

New device architectures for lead sulfide colloidal
quantum dot photovoltaics utilizing metal oxide
transport layers and electrodes

by

Alyssa M. Gonçalves

Submitted to the Department of Physics
in partial fulfillment of the requirements for the degree of

Bachelor of Arts

at

MOUNT HOLYOKE COLLEGE

May 2011

© Mount Holyoke College 2011. All rights reserved.

Author
Department of Physics
April 20, 2011

Certified by
Alexi C. Arango
Associate Professor of Physics
Thesis Supervisor

Accepted by
Janice Hudgings
Chair of Physics, Professor of Physics

I give permission for public access to my thesis and for any copying to be done at the discretion of the archives librarian and/or the college librarian.

Signed:

Date:

New device architectures for lead sulfide colloidal quantum dot photovoltaics utilizing metal oxide transport layers and electrodes

by

Alyssa M. Gonçalves

Submitted to the Department of Physics
on April 20, 2011, in partial fulfillment of the
requirements for the degree of
Bachelor of Arts

Abstract

Colloidal quantum dot photovoltaics are a class of third generation solar cell with the potential to harness greater amounts of solar energy than their silicon predecessors. These devices operate on the basis of electron transfer between two thin layers of semiconducting material. This project considers devices with semiconducting layers consisting of zinc oxide and lead sulfide quantum dots. Quantum dots are nanocrystalline semiconducting material, usually only a few hundred atoms in diameter. Their versatility lends them to wide ranging applications such as solar cells, light-emitting-diodes, and biological tagging. Their unique physical architecture motivates new inquiries into the physics of charge dynamics on the nanoscale.

This project uses two new device architectures for lead sulfide colloidal quantum dot photovoltaics. The goal is to examine the effect of oxygen exposure and layer thickness on device performance. We fabricate two sets of devices using sputter deposition and thin-film spin casting techniques. The power efficiency is determined by measurements of device current-voltage characteristics under illumination from a white light-emitting-diode. Quantum efficiency measurements are taken with a spectrometer, chopper and a Xenon light source. It is observed that exposing the device to oxygen after deposition of the lead sulfide quantum dot layer has a detrimental affect on device power and quantum efficiency, but results in increased open circuit voltage. Decreasing the thickness of the zinc oxide transport layer also produces a significant increase in device power efficiency. Finally, an annealing process is shown to have a restorative effect on electron transport through thicker layers of zinc oxide.

Thesis Supervisor: Alexi C. Arango
Title: Associate Professor of Physics

Acknowledgments

I would like to thank the following for their help in completing this work:

- My advisor, Professor Alexi Arango, for his guidance and for giving me the opportunity to pursue my first intensive experience not only with photovoltaic devices but also with undergraduate research.

- Professor Katherine Aidala for her support and her expertise in all things electronic and quantum-dot related.

- Kanchi Gashaw for being my lab partner over the summer and for spending many long hours with me tirelessly fabricating and testing all of the devices in this thesis.

- Nathan Monroe for his help in fabricating and characterizing the devices in this thesis and for introducing us to the *Tequila* waiting song.

- Professor Vladimir Bulović for giving me the opportunity to work in his lab over the summer and for being very friendly and hospitable.

- Patrick Brown, who patiently watched over Kanchi, Nathan, and I in the lab over the summer and gave us a lot of support.

- Darcy Wanger for happily talking to us for hours about quantum dots and giving invaluable instruction on the synthesis and crash-out process.

- Leonard (Len) McEachern, Thomas Liimatainen, and Kadhair Al-Hemyari for their invaluable help and support in the lab at Mount Holyoke College.

- Kanchi Gashaw, Maggie Stevens, Laalitya Uppalapati, and Sophia Weeks for kindly helping to proofread the final drafts. The document as a whole is a whole lot better thanks to their great questions.

- Professor Margaret Robinson for being part of my thesis committee and for not only teaching me linear algebra but teaching it with passion.

- Professor Janice Hudgings and the Mount Holyoke College Department of Physics.

Contents

1	Motivation and Background	16
1.1	Overview: Solar cells and the business of converting light into electricity . . .	16
1.2	The Sun as a viable energy source	18
1.2.1	Analyzing the Sun’s electromagnetic radiation	20
1.3	Modern developments in solar cell technology	22
1.3.1	Silicon <i>p-n</i> junction solar cells	23
1.3.2	Thin-film structures, organics, and other novel materials	24
1.4	Prior work concerning colloidal quantum dot solar cells	25
1.4.1	Initial progression towards high efficiency lead sulfide nanocrystalline photovoltaics	27
1.4.2	Schottky-barrier lead sulfide quantum dot photovoltaics	28
1.4.3	Excitonic, heterojunction, and donor/acceptor quantum dot photovoltaics	29
1.5	Developing new device architectures	32
2	Basic donor/acceptor photovoltaic theory: from $h\nu$ to electricity	35
2.1	A basic donor/acceptor solar cell	36
2.2	Solar cells and circuit analysis	37
2.2.1	But first, a bit of electronics	37
2.2.2	An electronic model of the solar cell	39
2.2.3	Solar cell power efficiency and current-voltage characterization . . .	43
2.2.4	Plotting the current-voltage characteristics of a solar cell	46
2.3	Donor/acceptor photovoltaics	52
2.3.1	The photovoltaic effect	53

2.3.2	Using bandgap offset to transport charge	56
2.3.3	Expressing light and dark current in terms of bandgaps	59
2.3.4	Quantum dots	61
2.3.5	Size and tuneability	62
2.3.6	Charge transport and quantum tunneling	63
2.3.7	Solar cell quantum efficiency characterization	64
3	Experimental techniques in device fabrication and characterization	67
3.1	Quantum dot solar cell device design and overview	67
3.1.1	Device band diagram	70
3.2	Substrate and cleaning	70
3.3	Zinc oxide transport layer	71
3.3.1	Design attributes of the ZnO layer	72
3.4	Lead sulfide quantum dots	74
3.4.1	Spinning thin films	75
3.5	Final indium-tin-oxide electrodes	75
3.6	Characterization and testing fixtures	76
4	Experimental results	79
4.1	Affects of the open laboratory atmosphere on device efficiency after deposition of lead sulfide quantum dot films	79
4.1.1	Background Information	80
4.1.2	Experiment procedure and methods	82
4.1.3	Results	83
4.1.4	Analysis	88
4.2	Variations in zinc oxide thickness and effects of oven annealing on device efficiency	92
4.2.1	Experiment procedure and methods	93
4.2.2	Results	93
4.2.3	Analysis	99
5	Overview and conclusions	101

A	Procedure for synthesizing lead sulfide quantum dots	104
A.1	Equipment	104
A.2	Supplies	107
A.3	Chemicals	108
A.4	Procedure	108
A.4.1	To set up the 3-neck flask where the synthesis will occur:	108
A.4.2	To set up the solvent trap:	109
A.4.3	Adding the first two chemicals and completing the setup of the 3-neck flask:	110
A.4.4	Heating the chemicals:	111
A.4.5	Degassing the octadecane (ODE):	111
A.4.6	Preparing the TMS-S solution:	112
A.4.7	Introducing the TMS-S solution to the 3-neck flask system:	113
A.4.8	Preparing the PbS quantum dot solution for crash-out and storage:	114
A.4.9	Clean up:	114
A.5	Safety hazards	115
A.6	Liquid nitrogen perils	116
A.7	Liquid oxygen perils	117
B	Procedure for spinning lead sulfide quantum dot films	119
B.1	Supplies	119
B.2	Chemicals	120
B.3	Safety notes for spinning quantum dot films	120
B.4	Procedure for chemical preparation	121
B.5	Procedure for spinning films of lead sulfide onto device	121
C	Full scale current-voltage and quantum efficiency curves	123

List of Figures

1-1	The International Space Station and its unfurled solar panels [1]. The ginormous silicon solar arrays generate 84 kilowatts of power to support the crew and their laboratories [2].	18
1-2	Images of the Sun taken from SOHO's Extreme ultraviolet Imaging Telescope (EIT) on March 30, 2011 [3]. EIT uses imaging techniques to observe the Sun emitting solar radiation across various wavelengths. Shown here are images taken of the sun at 60,000 to 80,000 degrees Kelvin (K), 1×10^6 K, 1.5×10^6 K, and 2×10^6 K [4].	19
1-3	The solar spectrum shown is Figure 18.3 from <i>Chemistry: The Central Science</i> , 10th Edition [5]. This plot depicts the sun's irradiance across different wavelengths and shows a peak around the 400-500 nm range.	21
1-4	Two graphs plotting the solar spectrum from Figure 3.2 from Professor Alexi Arango's doctoral thesis [6] showing solar energy with respect to wavelength (left) and photon energy (right).	22
1-5	Half-inch wide second generation solar cells of thin film silicon used as part of a novelty recharging station for two +AA batteries.	24
1-6	Size comparison between a standard quantum dot (shown: 3 nm in diameter) and the author's thumbnail (0.5 in wide). About 4.2 million of these quantum dots would cross this distance if laid out side by side.	33
2-1	A simple donor/acceptor model solar cell consisting of an electron-transporting layer (ETL), a hole-transporting layer (HTL), and two electrodes (-,+). The solar cell uses photons to generate a photocurrent (J_{light}) that is sent through a load (lightbulb) in a simple circuit.	36

2-2	A model depicting current flow from high voltage to low voltage as downhill slopes on a mountain river (left) and its analogous circuit diagram showing direction of current flow from 20 volts dropping across two resistors to 0 volts (right).	38
2-3	A section of a hypothetical circuit diagram, showing voltage driving current as a difference in measured voltages V_1 and V_2 at an electric load's input and output terminals. The "electronic component" can be any load which takes current, such as a lightbulb or a light-emitting diode (LED).	38
2-4	A few basic symbols used in circuit diagrams to represent electronic components: (a) a diode and (b) a resistor (c) a load and (d) a power source. . .	39
2-5	The circuit diagram equivalent of a solar cell showing both diode and photocurrent-generating components in parallel with the electrodes. The drawing is based off of Figure 1.7 from <i>The Physics of Solar Cells</i> [7].	41
2-6	Graph adapted from Figure N3.9 in <i>The Student Manual for the Art of Electronics</i> [8] displaying current-voltage characteristics for an ideal diode. . . .	42
2-7	A sketch of the light (solid line) and dark (dashed line) current-voltage characteristics observed by a hypothetical photovoltaic with open-circuit voltage (V_{oc}) and short-circuit current (I_{sc}) points labeled.	44
2-8	Light current plots showing equivalent circuit conditions for (a) open-circuit voltage (V_{oc}) and (b) short-circuit current (J_{sc}).	45
2-9	A typical current-voltage curve for a photovoltaic device with short-circuit current and open-circuit voltage labeled. Current and voltage are both scaled linearly. The data used in this and the following four plots is from the control device in set 20100628 from Section 4.1.	46
2-10	A typical current-voltage curve for a photovoltaic device. A device's fill factor is determined by taking the ratio between $P_{theoretical} = J_{sc}V_{oc}$ (the large rectangle shown in green) and $P_{max} = J_mV_m$ (the small rectangle shown in purple). Current and voltage are both scaled linearly.	48
2-11	An atypical current-voltage curve for a photovoltaic device using the absolute value of all points in both light and dark current curves. This plot is a transition step between showing current and voltage scaled linearly and scaled logarithmically.	49

2-12	A typical half-log current-voltage plot for a photovoltaic device. All values along the dark current curve can clearly be seen alongside the shape of the light current curve. Current is scaled logarithmically and voltage is scaled linearly.	50
2-13	A typical current-voltage curve for a photovoltaic device. Both current and voltage are scaled logarithmically.	51
2-14	Shown is a circuit diagram of a solar cell with shunt resistance (R_{sh}) and series resistance (R_s) from Figure 1.10 of <i>The Physics of Solar Cells</i> [7]. In an efficient cell, $R_s = 0$ and $R_{sh} = \infty$	52
2-15	Shown are how a solar cell's light current curve is affected by series resistance (a) and shunt resistance (b), from Figure 1.11 of <i>The Physics of Solar Cells</i> [7]. Note that the current axis has been adjusted so that the direction of the photocurrent is positive and the direction of the dark current (not shown) is negative.	53
2-16	Sketch of a photon transferring its energy to an electron in an atom's highest occupied molecular orbital (right), enabling the electron to pop out of its orbital. The resulting positively-charged ion (specifically, a cation) and free-moving negative charge carrier are shown on the left.	54
2-17	Illustration of (a) an electron gaining energy from an incident photon, leaving behind a hole in the lower energy state and (b) the bound electron-hole pair, called an exciton	55
2-18	A sketch depicting (a) exciton generation from an incident photon and diffusion towards the heterojunction (b) exciton separates as the hole crosses the heterojunction to a higher energy state in the hole transporting layer (HTL) and (c) electron and hole move as free charge carriers across their respective transport layers to transfer their charge to opposing electrode.	57
2-19	A physical approximation of exciton separation at the junction between a hole-transporting layer (HTL) and electron-transporting layer (ETL) in a model photovoltaic device. The exciton splits as the hole (white circle) crosses the barrier into a more favorable energy state and leaves behind its companion electron (black circle).	58

2-20	Diagrams illustrating how applying forward and reverse bias affect the bandgaps of a photovoltaic's ETL and HTL (left) and the current flow through equivalent circuit diagrams (right). Shown is (a) J_{dark} under forward bias (b) J_{dark} under reverse bias (c) J_{photo} under forward bias and (d) J_{photo} under reverse bias.	60
2-21	Sketch of a quantum dot made up of atoms of lead and sulfide (PbS).	62
2-22	Two vials of cadmium selenide (CdSe) quantum dots quantum dots under a UV lamp, synthesized under the supervision of Darcy Wanger in the Bawendi Lab.	63
2-23	Quantum dots suspended in solution showing long ligands (left) exchanged for shorter ligands (right) during the chemical "crash out" process.	64
2-24	An example graph from a hypothetical device displaying quantum efficiency measurements per photon energy (right).	65
3-1	Cross section and overhead view of a device showing individual layers of material used in device design including glass substrate, indium tin oxide electrodes, lead sulfide quantum dot electron donor layer, and zinc oxide electron accepting layer.	68
3-2	A completed device as seen resting in a circular fluoroware wafer container within a glovebox used for solar cell testing.	69
3-3	An energy level diagram of the solar cells fabricated in this thesis, showing the ZnO bandgap is $\sim 3.4\text{eV}$ [30], the PbS bandgap is $\sim 1.4\text{ eV}$ [28], and the work function for ITO is $\sim 4.8\text{ eV}$ [30].	70
3-4	Uncut strips of 1 mm (0.039 in) thick glass with a layer of indium-tin-oxide printed on one side. The transparent ITO layer is tinted purple can be seen in the the window reflection as a purple-tint.	71
3-5	Sketch of zinc oxide deposition using mask inside sputter chamber (left) and final film after deposition (right).	72
3-6	A sketch of inside of the sputter deposition chamber in the ONE Lab used to deposit the zinc-oxide on the devices fabricated in this thesis. The chamber consists of three deposition targets (bottom) and a z-stage used to hold the stencil-tray with glass substrates lying face down.	73

3-7	Completed layer of zinc oxide (right) seen with the mask which produced the design (left).	74
3-8	Sketches of solar cell shown right after spin coating films of PbS quantum dots (left) and after a border has been scratched off (right).	75
3-9	Metal tray used to load substrates into the metal oxide sputter deposition chamber, seen here with electrode stencil mask lying on top.	76
3-10	Diagrams of bottom (left) and top (right) transparent ITO electrodes of device sans the other layers.	77
3-11	Testing fixture with probes. The completed solar cell is placed with glass side up and top electrode side down in the center with each of the metal probes touching one of the ten pads.	78
4-1	A glovebox used for handling chemicals during the device fabrication process. Materials can be transferred inside the box using antechambers, such as the one with the red handle on the left, and users can access the inside of the box through the long, black rubber gloves.	80
4-2	Current-voltage curves showing how performance varies between ZnO and PbS solar cells that have spent 0 and 5 minutes (top) and 0 and 15 minutes (bottom) outside of an inert glovebox atmosphere.	84
4-3	Current-voltage curves comparing how performance varies between ZnO and PbS solar cells that have spent 0 and 30 minutes (top) and 0 minutes and 1 hour (bottom) outside of an inert glovebox atmosphere.	85
4-4	Current-voltage curves showing how performance varies between ZnO and PbS solar cells that have spent 0 minutes and two hours outside of an inert glovebox atmosphere (top) and collected current-voltage curves for all solar cells from Figure 4-2, Figure 4-3, and Figure 4-4 (bottom).	86
4-5	Collected quantum efficiency curves for devices 20100628 showing how photon energy absorption varies between devices that have spent varying amounts of time outside of an inert glovebox atmosphere.	87
4-6	Collected short-circuit current density for devices 20100628 taken at a bias of 0 volts.	89

4-7	Sketch of electron-hole separation and recombination after excitation from an incident photon. Hole mobility within the lead sulfide causes recombination at the zinc oxide and lead sulfide barrier.	90
4-8	Sketch of electron-hole separation after excitation from an incident photon where the electron is able to overcome the lead sulfate barrier but hole mobility is limited and it is unable to recombine with the electron in the zinc oxide layer.	91
4-9	Two colloidal quantum dot photovoltaics showing variations in zinc oxide thickness.	92
4-10	Collected current-voltage curves for solar cells 1, 3, 5, and 7 out of the set of devices 20100706. Each was fabricated with ZnO layers of different thicknesses ranging from 10 nm to 220 nm.	94
4-11	Collected current-voltage curves for solar cells 2, 4, 6, and 8 out of the set of devices 20100706. Each was fabricated with ZnO layers of different thicknesses ranging from 10 nm to 220 nm that were annealed in an oven before the PbS layer was spun on top.	96
4-12	Collected current-voltage curves for all solar cells in the set of devices 20100706. Each was fabricated with ZnO layers of different thicknesses ranging from 10 nm to 220 nm and devices 2, 4, 6, and 8 were annealed in an oven before the PbS layer was spun on top.	97
4-13	Collected short-circuit current density for devices 20100706 with un-annealed ZnO layers (teal) and annealed ZnO layers (purple).	98
5-1	Films of cadmium selenide quantum dots diluted with chloroform and spun on top of plain glass substrates (top row) and substrates deposited with a layer of zinc oxide (middle and bottom rows), shown here under a fluorescence microscope at varying levels of magnification.	103
A-1	Vials containing individual batches of lead sulfide nanocrystals. Each vial contains nanocrystals of different sizes: 2.3 nm (left), 3.3 nm (middle), and 5.4 nm (right) in diameter.	105
A-2	Rough sketch of finished quantum dot synthesis setup, including necessary glassware components, and complete lines for nitrogen, water, and vacuum.	118

C-1	Full scale current-voltage curves for devices 20100628 showing how current and voltage varies between devices which have spent varying amounts of time outside of an inert glovebox atmosphere.	124
C-2	Full scale quantum efficiency curves for devices 20100628 showing how photon energy absorption varies between devices which have spent varying amounts of time outside of an inert glovebox atmosphere.	125
C-3	Full scale current-voltage curves for solar cells 1, 3, 5, and 7 out of the set of devices 20100706. Each was fabricated with ZnO layers of different thicknesses ranging from 10 nm to 220 nm.	126
C-4	Full scale light current-voltage curves for solar cells 2, 4, 6, and 8 out of the set of devices 20100706. Each was fabricated with ZnO layers of different thicknesses ranging from 10 nm to 220 nm that were annealed in an oven before the PbS layer was spun on top.	127
C-5	full scale dark current-voltage curves overlaying the light curves from Figure C-4 for all devices 20100809. Each was fabricated with ZnO layers of different thicknesses ranging from 10 nm to 220 nm that were annealed in an oven before the PbS layer was spun on top.	128
C-6	full scale light current-voltage curves from all solar cells out of the set of devices 20100706 showing how devices with different thicknesses of ZnO performed with and without annealing the ZnO layer.	129

List of Tables

4.1	Devices 20100628 produced to test air annealing of lead sulfide quantum dot hole-transporting layer.	83
4.2	Chart of the short-circuit current (J_{sc}), open-circuit voltage (V_{oc}), and fill factor (FF) for each device in set 20100628.	83
4.3	Devices 20100706 produced to test optimal thickness of zinc oxide electron acceptor semiconducting layer.	93
4.4	Devices 20100706 produced to test optimal thickness of zinc oxide electron acceptor semiconducting layer.	95
4.5	Devices 20100706 produced to test optimal thickness of zinc oxide electron acceptor semiconducting layer. * = the device was annealed after ZnO layer was deposited.	95

Chapter 1

Motivation and Background

This chapter will introduce to the reader basic concepts behind solar cell use and fabrication. I will begin with the motivation behind undertaking the research presented in this thesis, discussing how the Sun's energy is a suitable alternative to current fossil fuels. Next, I will present a short summary of photovoltaic history and how devices have evolved over recent years to become more practical and efficient. The chapter will conclude with a review of recent literature concerning modern solar cell materials and design, including some of the predecessors to the quantum dot solar cells that will be discussed in the succeeding pages of this thesis. The chapter will conclude by introducing the solar cells that were fabricated in this thesis, a device that uses a layer of zinc oxide in combination with a photon-absorbing layer of lead sulfide semiconductor nanocrystals and indium-tin-oxide electrodes. We will only touch upon the most critical aspects of solar cell physics in this chapter and continue with a more detailed discussion in Chapter 2.

1.1 Overview: Solar cells and the business of converting light into electricity

A solar cell, or a photovoltaic device (PV), converts energy from the Sun into electric current. Photons have the ability to transfer their energy to the electrons that exist within the atoms of the solar cell's semiconducting material. Given enough energy, electrons confined in the outermost atomic orbitals are excited into higher energy states and become carriers

of negative charge. This charge is now free to traverse the semiconductor. These excited electrons leave behind identical but oppositely-charged spaces, called holes. A hole is the absence of an electron. A voltage develops across the photovoltaic when one side of the device becomes more negatively charged than the other. The difference in charge, or photovoltage, results from electrons drifting through the semiconductor in one direction and holes drifting in the opposite direction. When the illuminated device is properly hooked up to a circuit, photovoltage will drive a photocurrent that can then be used to power an electronic load, such as a light bulb. At its most basic, a solar cell is a battery that does not work in the dark and exhibits unique, photovoltaic current-voltage characteristics.

This is a mere sketch of how most solar cells work, for photovoltaic theory changes depending on what materials are used in the device's architecture. The science behind the solar cells discussed in this thesis is only just beginning to be understood. Next-generation solar cells has expanded research to include new photovoltaic materials such as thin film organics and colloidal quantum dot semiconductors. The goal of this new technology is to create improved solar cells that will offer long-term sustainability, greater power efficiency, and affordable costs. Research into solar cell photovoltaics also lends itself to applications in light-emitting diodes (LEDs). LEDs are the antithesis to solar cells: devices which emit photons when an electric current is applied.

The insight to how charge behaves on the atomic level is reason enough to continue expanding photovoltaic research, but there are practical concerns also driving the endeavor. Electricity is a crucial staple to living a comfortable and humane life in many parts of the world. Solar cells in themselves offer a clean, long-term solution to the now growing problem of supplying energy to an expanding global population. The cost that human society is paying for the fossil fuel market can be seen in the alarming damage fossil fuels do to the environment. In April 2011, the Tennessee Valley Authority announced that it was closing 18 of its coal plants that, altogether, were releasing 15 million tons of carbon dioxide into the atmosphere in 2008 [9]. Forms of alternative energy, solar cells included, have been a hot topic in political discussion over the past several years, often tied into conversations about climate change. The lack of quality in the scientific data on the Earth's climate being brandished by today's politicians and legislatures has concerned scientists such as physicist Richard A. Muller, who helped conceive the now nearly completed Berkeley Earth Surface Temperature (BEST) project that will present experimentally sound data on the

current and projected state of the Earth's climate [10]. If and when this data, and the data from future studies like it, is used to prompt a stronger call for renewable energy to be implemented in everyday life, solar cells will most certainly be an alternative worthy of consideration.



Figure 1-1: The International Space Station and its unfurled solar panels [1]. The ginormous silicon solar arrays generate 84 kilowatts of power to support the crew and their laboratories [2].

1.2 The Sun as a viable energy source

The Sun is the biggest known source of energy in our solar system. A vast amount of energy is generated within the Sun's core as the byproduct of nuclear reactions that turn atoms of hydrogen into nuclei of helium [11]. This energy makes its way to the surface and is emitted in the form of electromagnetic radiation that we can feel on Earth in the form of light and heat [11]. Life on Earth would not be able to exist if the planet did not orbit in the habitable region around the star, where the amount of electromagnetic radiation that it receives is just enough to sustain carbon-based life. The Sun is roughly 4.5 billion years

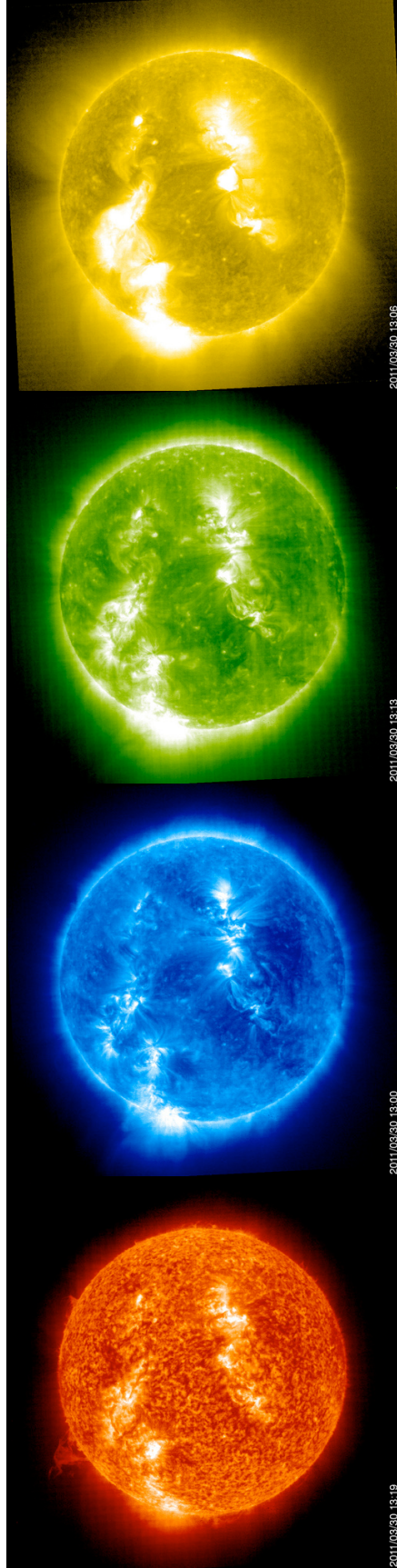


Figure 1-2: Images of the Sun taken from SOHO's Extreme ultraviolet Imaging Telescope (EIT) on March 30, 2011 [3]. EIT uses imaging techniques to observe the Sun emitting solar radiation across various wavelengths. Shown here are images taken of the sun at 60,000 to 80,000 degrees Kelvin (K), 1×10^6 K, 1.5×10^6 K, and 2×10^6 K [4].

old and estimated to have a total lifespan of 14 billion years. At present, the Sun's energy is abundant and in no danger of depleting.

Photosynthesis is one biological example of how life already utilizes the Sun's energy: certain plants absorb sunlight and through a series of internalized reactions are able to produce nutrients for themselves. This energy can also be transferred to organisms that consume all or part of the plant. Harnessing the Sun's energy requires ingenuity in utilizing the properties of different photon-absorbing materials.

Solar cells have already been successfully implemented by NASA as one of their chief energy sources for driving and sustaining space missions. The photovoltaic arrays seen in Figure 1-1 currently keep the International Space Station in orbit around the earth, housing scientists from all over the world and providing power for their experiments [2]. Photovoltaic devices have also been used by NASA to bring interstellar vehicles such as New Horizons and Cassini far into the solar system.

1.2.1 Analyzing the Sun's electromagnetic radiation

The Solar and Heliospheric Observatory (SOHO) was launched by the European Space Agency (ESA) and the National Aeronautics and Space Administration (NASA) in December 1995 [12] and the latest solar data obtained from SOHO is available for free on NASA's website (<http://sohowww.nascom.nasa.gov/data/realtime-images.html>). The four photographs of the Sun in Figure 1-2 were taken with SOHO's Extreme ultraviolet Imaging Telescope (EIT) and show the Sun's inner corona and transition region at four different temperatures in the extreme ultraviolet region of the electromagnetic spectrum [13]. Further data concerning the EIT can be found on the instrument's homepage (<http://umbra.nascom.nasa.gov/eit/>). The corona is the outermost region of the Sun. Each color in Figure 1-2 corresponds to a different temperature: red/orange is 60,000 to 80,000 degrees Kelvin (K), blue is 1×10^6 K, green is 1.5×10^6 K, and yellow is 2×10^6 K [4]. Kelvin is a standard unit of temperature which is scaled so the point 0 K is equal to absolute zero. For the sake of comparison, room temperature of 18 degrees Celsius (64 degrees Fahrenheit) is equal to 291.15 Kelvin. These ranges encompass only a fraction of the total solar radiation that the Sun emits.

Figure 1-3 shows a more complete picture of the electromagnetic radiation emitted by

the Sun in terms of irradiance (a measure of Watts per meter-squared) and wavelength (in meters). It should be noted that the Sun emits greater quantities of radiation at certain wavelengths than it does at others. According to Figure 1-3, there is less solar energy contained in wavelengths of 3000 nm than in wavelengths of 600 nm. However, irradiance is a poor way to measure power in the solar spectrum. Section 3.2.2 of Professor Alexi Arango’s doctoral thesis describes how plotting irradiance in terms of wavelength skews the data to make shorter wavelengths appear to contain more power than longer wavelengths [6]. Plots attempting to chart solar energy in terms of wavelength, such as the one in Figure 1-3, shows an inaccurate picture for how power is distributed across the solar spectrum.

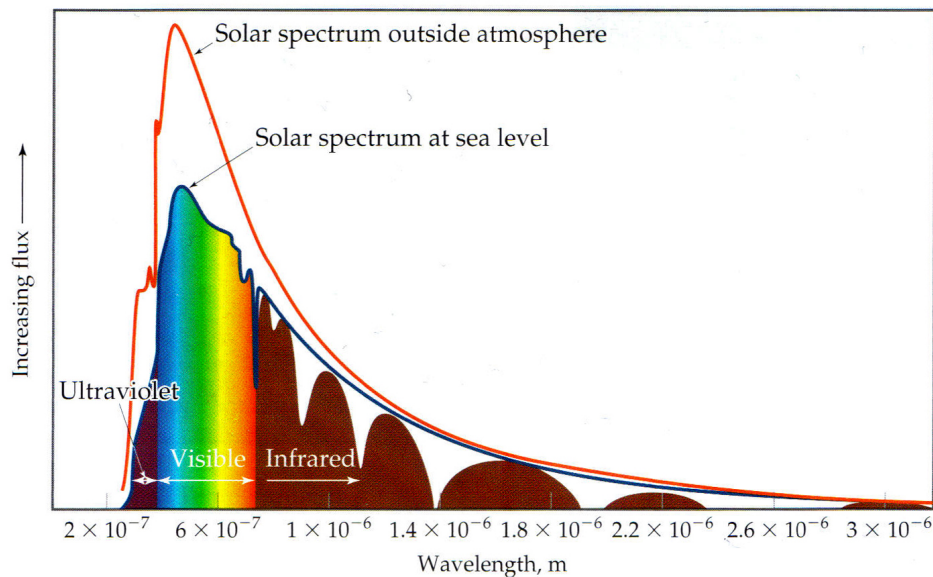


Figure 1-3: The solar spectrum shown is Figure 18.3 from *Chemistry: The Central Science*, 10th Edition [5]. This plot depicts the sun’s irradiance across different wavelengths and shows a peak around the 400-500 nm range.

Wavelengths can be converted into quantized packets of energy, called photons, with units of electron volts (eV). One electron volt is equal to 1.602×10^{-19} Joules and the conversion between photon energy (eV) and wavelength (λ) is as such:

$$E(eV) = \frac{1240}{\lambda(nm)}$$

Photon energy is plotted, not in terms of irradiance, but in terms of photon flux. Figure

1-4 shows the difference when the solar spectrum plotted as a function of wavelength (left) and as a function of photon energy (right). The graph on the left in Figure 1-4 is similar to the plot in Figure 1-3 in that it plots the solar spectrum in terms of irradiance versus wavelength and shows a peak in the spectrum around 400-500 nm. The graph on the right in Figure 1-4 plots the solar spectrum in terms of photon flux versus photon energy and shows a peak in the spectrum around 800nm, or the infrared.

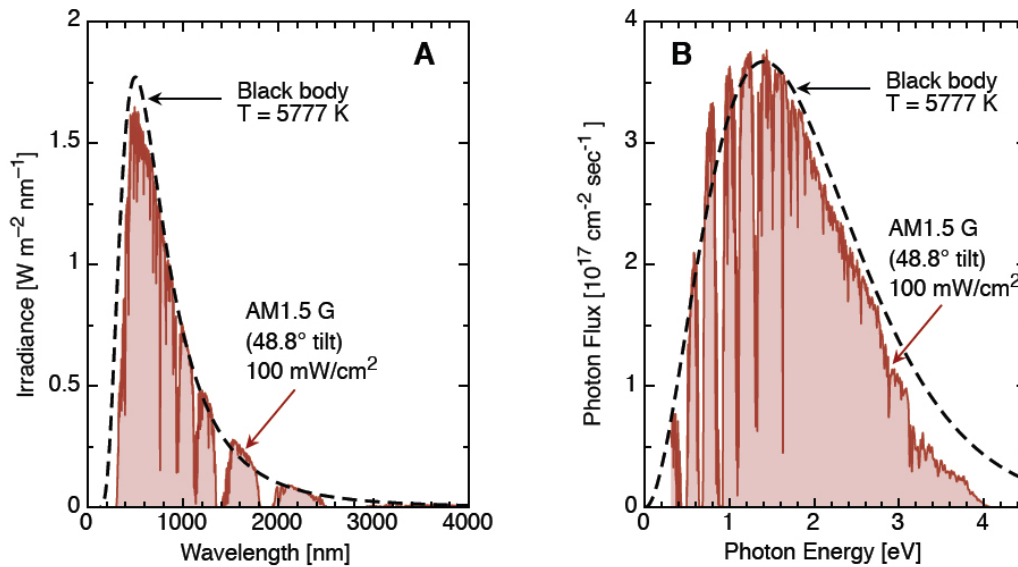


Figure 1-4: Two graphs plotting the solar spectrum from Figure 3.2 from Professor Alexi Arango’s doctoral thesis [6] showing solar energy with respect to wavelength (left) and photon energy (right).

The total solar power which is felt at the surface of the Earth, year-round and throughout the entire day, averages to about 100 Watts-per-meter-squared (Wm^{-2}) around the globe and $300 Wm^{-2}$ near the equator [14]. The standard solar spectrum at the Earth’s surface, as defined under specific atmospheric conditions, is referred to as Air Mass 1.5, or simply AM 1.5, and is used as a standard for developing photovoltaic devices [15].

1.3 Modern developments in solar cell technology

The physics that makes solar cells possible has been studied since the 19th century. Before the advent of the modern solar cell, scientists were studying a phenomena called the

photovoltaic effect, wherein electric current can be generated by exposing materials to photons. Study of the photovoltaic effect can be traced back as early as 1839, when researcher Edmund Becquerel observed electric current being produced by a platinum, silver-coated electrode that he had suspended in electrolyte and exposed to light [7]. The first known photovoltaic device, a selenium rod fitted with platinum contacts, was produced less than half a decade later, in 1877, by researchers W.G. Adams and R.E. Day [14] [16]. Experiments with photovoltaic materials continued into the mid-20th century, with researchers mostly interested in developing accurate photographic light meters [7].

The advent of silicon solar cells marked the beginning of producing photovoltaics as a source of clean electricity. The first silicon solar cells were expensive to produce and were used mostly by industries such as NASA for space exploration and satellites [7]. Development of solar cells for a wider commercial market, including the private sector, took off in the 1970s due to growing concerns over the cost of oil and the mortality of fossil fuels [7]. This growing societal concern for human civilization's over-reliance on limited resources for fuel still is one of the main driving factors behind photovoltaic research. Since the 1950s, there have been many different types of solar cells, each with their own sophisticated structure and materials. Three categories will be outlined here as context for the quantum dot solar cells that are the topic of this thesis.

1.3.1 Silicon p - n junction solar cells

The first type of solar cell is the silicon (Si) solar cell. Instantly recognizable as flat, bluish panels, they were the first to be produced commercially and have persisted to the point where they can now be found, not only in simple, novelty devices, but also covering entire rooftops of buildings. More than 85% of the global photovoltaic market consists of these expensive, first generation crystalline silicon (c-Si) solar cells [17], but even the best laboratory-fabricated silicon solar cells can only reach sun-to-electricity conversion efficiencies of 24% [18]. Efficiencies for silicon solar cells worsen when they are produced commercially, dropping to 15-20% [18]. The prevalence of crystalline silicon on the global market can be attributed to a few benefits that it has as a photovoltaic material. Silicon solar panels have long lifespans of over twenty-five years [19] and a strong history of use in solid-state devices, which makes it a familiar material to engineers [14]. However, silicon

does not absorb light well and as a result, most first generation cells are quite thick and expensive to produce [14]. For solar cells to find a niche on the market, device efficiency needs to improve and fabrication methods must be cheap and easy for mass production.

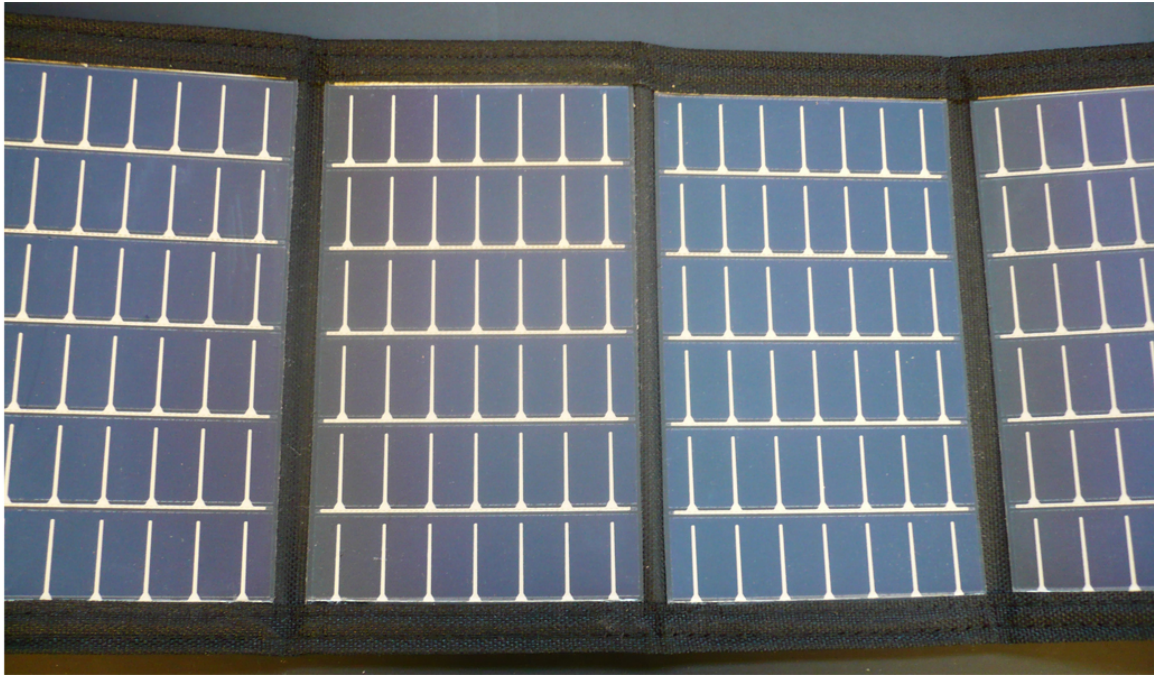


Figure 1-5: Half-inch wide second generation solar cells of thin film silicon used as part of a novelty recharging station for two +AA batteries.

1.3.2 Thin-film structures, organics, and other novel materials

A second generation of solar cells began to develop as scientists searched for ways to make smaller, cheaper, and more efficient solar cells. They attempted to use different materials and thinner films, including amorphous silicon (a-Si) and cadmium telluride (CdTe) [17]. Researchers have found that cheaper solar cell production most often came at a cost of lower device efficiency [17]. However, thin film silicon has been used to successfully market relatively inexpensive solar powered devices, such as the +AA battery recharger in Figure 1-5. Thin-films, by their nature, use much less material than crystalline silicon cells, but they haven't yet matched c-Si's prominence on the photovoltaic market [19]. At present,

the expense of solar energy remains high when compared to other energy alternatives, preventing solar energy from making substantial progress in the global market [20].

Recent innovations have pushed the science of solar cells even further in terms of both materials and fabrication methods. Laboratories are developing a new wave of photovoltaic devices, focusing on the physics of more unconventional semiconducting materials [17]. This generation includes solar cells that use organic materials and colloidal quantum dots, or nanocrystalline amounts of material. New fabrication techniques are also being sought as a way to further reduce manufacturing cost. For instance, the production of organic solar cells use small amounts of material that can be printed, roll-to-roll, onto cheap, flexible substrates [21]. Solar cell costs will most likely remain high until this kind of high-output manufacturing can be implemented for a mass market [17].

Solar energy has been making rapid advances in recent years towards becoming an indispensable part of everyday life. The industry has been sustaining a 40% growth rate, predicting that electricity from solar devices will begin to seriously compete against electricity from the grid in the following decade [18]. A study performed by Stanford University in 2009 placed solar energy near the top of a list of energy systems that are the least harmful to the environment [22]. *Scientific American* recently gave quantum dot photovoltaics a small nod in a list of the most potent, but unrealized sources of alternative energy currently under investigation by scientists and engineers, listing QD solar cells as more likely to break into the mainstream than other experimental alternatives such as fusion-triggered fission power plants and a type of sunlight-produced hydrogen and carbon monoxide-blend synthesis gas [23]. So long as solar energy continues to gain public interest and motivate research interests, there is no reason why photovoltaic devices cannot become become a practical energy alternative.

1.4 Prior work concerning colloidal quantum dot solar cells

The topic of this thesis concerns colloidal quantum dot solar cells and uses a donor/acceptor photovoltaic model to describe charge transport between the device's two semiconducting layers. This section contains a review of the recent literature pertaining to similar devices

and materials. Also discussed are noteworthy papers which broke through to record quantum dot photovoltaic device efficiencies, the predecessors to the specific zinc oxide, lead sulfide nanocrystal, and indium-tin-oxide architecture used in this thesis' photovoltaic devices. In brief, the treatment of the PbS quantum dots before deposition seems to have a significant affect on device efficiency, particularly the treatment of the ligands which surround the dots in solution. Ligands are chains of molecules which attach to the outside, spherical surface of a quantum dot during synthesis to control dot growth [24] and can cause resistance as charge carriers attempt to move between the semiconducting dots.

The quality of a photovoltaic device is determined by four key measurements: open-circuit voltage (V_{oc}), short-circuit current (I_{sc} , or short-circuit current density, J_{sc}), fill factor (FF), and efficiency (η). Open-circuit voltage and short-circuit current are a measure of the maximum current and voltage that a solar cell can produce while under illumination. A solar cell will drive maximum current when it is in a short-circuit and will have a measure of 0 volts across its electrodes. In a short-circuit, there is no resistance encountered by current which travels via wire from one solar cell electrode to the other. A solar cell will have maximum voltage across its electrodes in an open circuit and there is no current flowing from one electrode to the other. An open circuit is when the solar cell is not connected to a circuit, or is part of a broken circuit. Fill factor is the ratio between the solar cell's maximum power and $J_{sc} \times V_{oc}$. Efficiency is a measure of how well a solar cell can convert energy from incident photons into electrical energy and can be related to fill factor, open-circuit voltage, and short-circuit current by the following equation:

$$\eta = \frac{J_{sc}V_{oc}FF}{P_{solar}}$$

where P_{solar} is the amount of solar power incident on the solar cell at the time of the measurement. A solar cell is often more efficient at absorbing photons from certain regions of the solar spectrum than others. The papers discussed in the following section often reference AM1.5 testing conditions, which is using the Air Mass 1.5 Spectra (<http://rredc.nrel.gov/solar/spectra/am1.5/>) as the model light spectrum used when testing solar cell [15].

One final measurement to take note of is quantum efficiency. External quantum efficiency (EQE) is a ratio between the number of photons that are shining on a solar cell to

the number of electrons measured at the solar cell's electrodes. Internal quantum efficiency (IQE) is a ratio between the number of photons that are actually absorbed by the solar cell to the number of electrons measured at the solar cell's electrodes. Photon absorption is determined by a characteristic known as the material's bandgap (E_g). The bandgap is a concept that is too complicated to explain in full here and will be fleshed out more in the following chapter, but simply put, the bandgap determines how much energy is needed to generate free charge carriers within a material, and thus electric current.

This is a brief introduction to how solar cell performance is measured so that the results presented in the following literature may be better understood by readers who are unfamiliar with the terminology. A more detailed explanation of solar cell characterization is discussed in Chapter 2.

1.4.1 Initial progression towards high efficiency lead sulfide nanocrystalline photovoltaics

In the November of 2005, Maria et al. published a novel infrared nanocrystal photovoltaic device architecture which absorbs photons in the 1-3 μm (1000-3000 nm) range, has 1% external quantum efficiency (EQE), and over 10% internal quantum efficiency (IQE) [25]. The device architecture consists of an indium-tin-oxide (ITO) substrate as the bottom anode, a 40 nm-thick PEDOT:PSS layer, an 80 nm-thick P3OT layer, a lead sulfide (PbS) nanocrystal layer ranging in thickness from 80-160 nm, and an 80 nm-thick aluminum (Al) as the top cathode [25]. They are one of the first to use an active layer fabricated just using nanocrystals instead of a polymer/nanocrystalline blend in addition to using shorter ligands attached to the nanocrystal's surface and the group attributes both to the improved device efficiencies [25]. The PbS nanocrystals have long oleic acid ligands which are attached during synthesis and then exchanged with shorter, primary butylamine ligands [25]. The group makes reference to another infrared-absorbing photovoltaic architecture that is their predecessor, also using lead sulfide nanocrystals as the photon-absorbing layer, but achieving a much smaller efficiency of 0.0008% [25].

1.4.2 Schottky-barrier lead sulfide quantum dot photovoltaics

In the April of 2008, a group reported a solution-processed Schottky-PbS-quantum dot photovoltaic device with a power conversion efficiency of 4.2% in the infrared [26]. The device architecture consists of a spin-cast, 100-300 nm thick lead sulfide nanocrystal layer sandwiched between a glass substrate coated with indium-tin-oxide (ITO) and a thermally evaporated stack of 0.7 nm-thick lithium-fluorine (LiF), 140 nm-thick aluminum (Al), and 190 nm-thick silver (Ag) as a Schottky contact [26]. The group states that their high device efficiencies are attributed to a fabrication technique that includes replacing cumbersome and highly resistive ~ 2.3 nm long oleate ligands with ~ 0.6 nm long *n*-butylamine ligands to enable a closely-packed, uniform PbS layer that facilitates charge transfer [26]. The group also reports that they are able to increase device open-circuit voltage by a factor of 2 when they immediately submerge the nanocrystals in an ice bath after the growth stage of the synthesis process, thereby cooling the nanocrystals at a faster rate and supposedly lowering the density of quantum trap states for charge to interact with at the device's PbS/Al Schottky-barrier [26].

Previous work by Johnston on Schottky-quantum dot solar cells includes a March 2008 paper with Andras G. Pattantyus-Abraham et al., describing the mechanics of charge behavior at a PbS/Al junction, the companion piece to Johnston's April 2008 article on a ITO/PbS/Al Schottky photovoltaic device architecture [27]. The group attributes high device efficiency to extensive time for charge carriers to exist and a large depletion region extending from the PbS/Al Schottky barrier interface deep into the bulk PbS quantum dot layer [27].

In the August of 2008, Luther et al. published a paper reporting on a Schottky junction, ITO/PbS nanocrystal/metal solar cell with a 2.1% AM1.5 power conversion efficiency, 55-56% visible wavelength external quantum efficiencies, 25% infrared EQE, and short-circuit photocurrent greater than 21 mA/cm^2 [24]. The device architectures consists of an ITO-coated glass substrate, a 60-300 nm-thick PbS colloidal quantum dot layer, and a metal contact. Various metal contacts, including (listed from lowest work function to highest:) calcium (Ca), magnesium (Mg), silver (Ag), aluminum (Al), and gold (Au) are tried and devices with calcium and magnesium are shown to produce higher open-circuit voltages than devices with silver, aluminum, and gold contacts [24]. Also noteworthy is the group's

deposition of the PbS quantum dot films layer-by-layer on top of the ITO-coated substrate by using a hexane solution and either a 0.01 M 1,2-ethanedithiol (EDT) or methylamine wash to remove oleate ligands from the PbS quantum dots [24]. A similar hexane and EDT bath, with the addition acetonitrile, is also used in treating the spin-coated PbS quantum dot layer in this thesis' devices, as described in Section 3.4 and Appendix B.

1.4.3 Excitonic, heterojunction, and donor/acceptor quantum dot photovoltaics

In the October of 2008, a paper was published reporting on a study which investigated how photoexcited electrons transfer from PbS quantum dots (QDs) into titanium dioxide (TiO_2) for potential use in solar cell fabrication that uses quantum dots to sensitize metal oxide materials to light [28]. The group finds it takes electrons ~ 100 nanoseconds to travel from PbS into TiO_2 , much longer than electron transfer times between cadmium selenide (CdSe) QD/ TiO_2 interfaces that happen as quick as $\sim 0.02 \mu\text{s}$ for CdSe QDs 4.6 nm in diameter and $\sim 0.12 \mu\text{s}$ for CdSe QDs 7.5 nm in diameter [28]. The group finds that the energy levels of small PbS quantum dots, less than 4.3 nm in diameter, allow for improved transfer rates of electrons into the TiO_2 and fabricate a Gratzel solar cell with a device architecture that has a 2-8 μm -thick TiO_2 layer with nanocrystals 2-8 μm in diameter over a set of fluorinated tin oxide electrodes [28]. The group's prototype Gratzel cell achieves 0.49 V open-circuit voltage, 1 mA/cm^2 short-circuit current density, a 57% fill factor, and a 0.28% energy conversion efficiency [28].

In the August of 2009, a report was given by Choi et al. on a solar cell design which uses an excitonic model to separate charge via separate electron-transporting and hole-transporting semiconducting layers in an effort to exceed the performances of Schottky solar cells by minimizing the bandgap-bending which occurs at material heterojunctions [29]. Device architecture consists of a bottom glass substrate with patterned ITO electrodes, a blended PEDOT:PSS/PbSe nanocrystal/zinc oxide (ZnO) nanoparticle active layer ~ 100 nm-thick, and 70 nm-thick aluminum electrodes on top [29]. Under AM1.5 illumination, they achieve 0.44 V open-circuit voltage, 24 mA/cm^2 short-circuit current, a 32% fill factor, and 3.4% efficiency [29]. They attribute their high open-circuit voltage to the mechanics of charge transfer in excitonic solar cell structure [29]. The group finds that open-circuit

voltage exponentially decreases with the size of nanocrystal diameter and correlates this to a change in energy level offsets between the PbS nanocrystal/ZnO nanoparticle interface[29].

In the October of 2009, a paper was published by Leschkies et al. on a set of solar cells that contain a heterojunction between layers of PbSe quantum dots and thin zinc oxide films [30]. Device architecture consists of a glass substrate patterned with ITO, a 30-100 nm-thick ZnO layer, a PbS quantum dot layer, and a 15-30 nm-thick α -NPD [N,N'-bis(1-naphthaleenyl)-N,N'-bis(phenylbenzidine)] layer meant to protect the quantum dots as a 100 nm-thick gold contact is deposited on top [30]. Their best solar cells achieve 12-15 mA/cm² short-circuit current, 0.45 V open-circuit voltage, and 1.6% power conversion efficiency under a stimulated AM1.5 spectrum of 100 mW/cm² illumination [30]. The group states that although their heterojunction devices perform better than Schottky solar cells that also use PbSe quantum dots, the α -NPD electron-blocking barrier is not suitable for this device architecture due to the mis-matched location of the α -NPD HOMO level relative to the PbSe QDs' LUMO level [30].

In the January of 2009, a paper was published by Arango et al. on a novel organic/quantum dot bilayer device which is able to maintain decent current-voltage characteristics using different sizes of quantum dots in the QD layer [31]. The device architecture consists of a glass substrated printed with a 100 nm-thick layer of ITO, a 100 nm-thick PEDOT layer, a 100 nm-thick organic N,N'-diphenyl-N,N'-bis(3-methylphenyl)[1,1'-biphenyl]-4,4'-diamine (TPD) layer, a 20 nm-thick layer of CdSe quantum dots, and a 100 nm-thick, transparent ITO top electrode [31]. The open-circuit voltage obtained by this device structure is one of the highest mentioned in this section, 0.8 V, that the group attributes to a low dark current flow and a high diffusion rate of charge carriers after separation at the TPD/QD heterojunction [31]. Also notable is the deposition method used to form the CdSe quantum dot layer. The quantum dots are deposited via microcontact printing with a PDMS stamp that achieves a planar heterojunction between the quantum dots and the TPD layer, as opposed to a mesoporous heterojunction [31]. The authors state that this quantum dot printing method is more suited for commercial applications, such as printing quantum dot pixels in a photodetector, than the traditional spin casting method [31].

In his doctoral thesis, submitted in the February of 2010 to the Massachusetts Institute of Technology, Professor Alexi Arango has identified low open-circuit voltages as a problem area for third-generation photovoltaics consisting of organic and polymer-based semicon-

ducting layers, which are otherwise ideal for production on a mass market scale due to the inexpensive and simple process of their fabrication [6].

In the May of 2010, a report on a depleted-heterojunction photovoltaic was published, comparing its performance to those of both Schottky solar cells and excitonic colloidal quantum dot (CQD)-sensitized solar cells [32]. The device structure of the depleted-heterojunction solar cell consists of a heterojunction between titanium-dioxide (TiO_2) and PbS colloidal quantum dots of different sizes, ranging from ~ 3.7 nm to ~ 5.5 nm [32]. The best depleted-heterojunction solar cell, using PbS quantum dots with a 1.3 eV bandgap (E_g), achieves 0.53 V open-circuit voltage, 16.2 mA/cm², a 58% fill factor, and 5.1% efficiency. On average, the depleted-heterojunction design performs better than the cited Schottky and excitonic QD-sensitized solar cells and the group attributes this performance to the superior architecture of the depleted-heterojunction [32]. The group states that the Schottky solar cell does not allow for decent charge transport from the photon-absorbing layer into the metal contact, resulting in low FF and V_{oc} , and that the CQD-sensitized solar cell is a poor photon-absorber, resulting in low J_{sc} [32]. The group argues that the architecture of the depleted-heterojunction solar cell combines the best factors of both the Schottky and excitonic designs without translating their deficiencies [32].

In the June of 2010, Zhao et al. published a paper concerning a lead sulfide quantum dot and fullerene derivative solar cell [33]. The device architecture consists of a glass substrate with a 150 nm-thick layer of ITO, a 110 nm layer of PbS quantum dots, a 70 nm layer of a fullerene derivative, [6,6]-phenyl-C61-butyric acid methyl ester (PCBM), and a 120 nm layer of magnesium-silver (Mg/Ag). After deposition of the PbS quantum dot layer, some devices are either nitrogen annealed, air annealed, or exposed to ozone (O_3) to affect the structure of the quantum dots, based on previous studies the group cites as having an improvement on V_{oc} by changing the composition of some PbS dots to include lead oxide (PbO) and lead hydroxide (PbO_3) [33]. Under AM1.5 testing conditions, devices that were air annealed and had PbS QDs with a bandgap less than 1.0 eV achieved a 62% fill factor, a V_{oc} of 0.47 V, and $\sim 1.3\%$ power conversion efficiency [33]. Exposure to ozone improves the power conversion efficiency of the devices, but lowers device fill factor and V_{oc} [33]. A similar air annealing process is undertaken to treat the PbS quantum dot layer of some devices in this thesis and the experiment is described in Chapter {results}.

In the July of 2010, a group reports on an ITO/TiO₂ nanocrystal/PbS nanocrystal/Au photovoltaic device architecture which is able to achieve greater than 3% efficiency, 20.7 mA/cm² short-circuit current density, 0.456 V open-circuit voltage, and 33% fill factor under AM1.5 testing conditions [34]. Device performance is further improved by cooling the device to 170 K (-103.15 °C) in a cryostat, achieving 28.6 mA/cm² short-circuit current density, 0.66 V open-circuit voltage, and 42.4% fill factor [34]. Device architecture consists of a glass, ITO-coated substrate as the bottom electrode, a 100 nm-thick planar, titanium dioxide (TiO₂) solgel, an n-type, mesoporous, nanocrystalline TiO₂ layer, a p-type PbS nanocrystal layer, and a 100 nm-thick gold top electrode [34]. Since individual PbS and TiO₂ nanocrystals intermingle at the mesoporous/mesoporous interface, the group thought that this would attribute to increased absorption and charge extraction within the materials, but concludes this actually hinders device performance and a planar/mesoporous interface is more favorable for charge transfer than a mesoporous/mesoporous interface [34]. Also interesting is the group's finding that they are able to improve the performance of their devices by cooling the device, attributing the improvement to organic ligands in the quantum dot layers constricting under lower temperatures and enabling better charge transport through the device [34].

1.5 Developing new device architectures

The solar cells fabricated in this thesis are unique in that their specific architecture has never been fabricated or tested before. The devices are built upon a glass substrate with electrodes of indium-tin-oxide and contain two semiconducting layers: one electron accepting zinc oxide layer and the other an electron donating lead sulfide layer. The lead sulfide layer is unique in that it consists of a lead sulfide colloidal quantum dot film. Quantum dots are tiny crystals of semiconducting material only a few nanometers in diameter. To give a sense of scale, a typical diameter for a quantum dot is around 3 nanometers (nm) and it would take about 4.2 million of them to span the width of an average sized thumbnail as shown in Figure 1-6. Conventional

device physics begins to break down in these nanostructures due to the unique nature of quantum confinement between dot barriers. More about third generation photovoltaic device physics and quantum dot architecture will be discussed in Chapter 2.

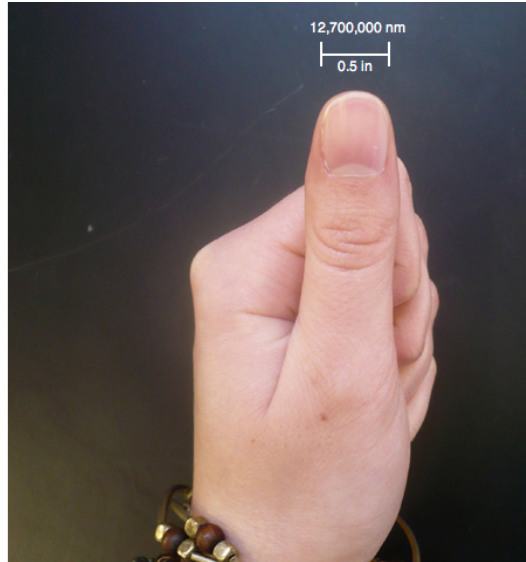
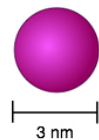


Figure 1-6: Size comparison between a standard quantum dot (shown: 3 nm in diameter) and the author's thumbnail (0.5 in wide). About 4.2 million of these quantum dots would cross this distance if laid out side by side.

The solar cells were fabricated at the Massachusetts Institute of Technology during the summer of 2010 by the author, Kanchi Gashaw, and Nathan Monroe using equipment from Professor Vladimir Bulović's lab under the guidance of Professor Alexi Arango and Patrick Brown. Fabrication of the solar cells is undertaken in a clean room environment with minimal exposure to dust or other foreign particulates. The devices are also kept in a chemically inert atmosphere of pure nitrogen or under vacuum to prevent corrosion during fabrication and for the remainder of their shelf life thereafter. A glass substrate pre-patterned with indium-tin-oxide (ITO) electrodes is cleaned in ultrasonic baths of micro-90, de-ionized water, acetone, and isopropanol for five minutes each, followed by a one-minute exposure to plasma. A layer of zinc oxide is deposited on top of the first set of electrodes using radio frequency sputter

deposition inside a magnetron sputter deposition chamber [6]. A thin film of lead sulfide quantum dots is laid across the zinc oxide layer through a spin coating process. Fabrication is complete when the device is capped off by depositing a final, top layer of ITO electrodes using radio frequency sputter deposition [6]. Testing takes place inside a glovebox under nitrogen atmosphere. The fabrication and characterization processes will be discussed extensively in Chapter 3.

This thesis is undertaken to investigate the physics behind a new device architecture for colloidal quantum dot solar cells. Two separate experiments are performed, each testing different aspects of device design with the intention of optimizing device power and quantum efficiency in addition to learning more about the material properties of zinc oxide and lead sulfide nanocrystals. The first experiment tests to see how oxygen exposure will affect device performance, particularly in the lead sulfide quantum dot layer. The second experiment attempts to find an optimal thickness for the zinc oxide electron transport layer that will maximize device performance. The second experiment also tests to see how using an oven to anneal zinc oxide layers with different thickness will affect device performance. The results from these experiments and detailed analysis is presented in Chapter 4.

Chapter 2

Basic donor/acceptor photovoltaic theory: from $h\nu$ to electricity

The aim of this chapter is to present readers with the necessary background to fully understand and appreciate the mechanics of solar cell device physics. A few different solar cell models were discussed in Chapter 1, including the p - n junction [14], the Schottky-quantum dot solar cell [26] [27] [24], quantum-dot sensitized solar cells (CQD-SSC) [28] [32], and depleted-heterojunction device structures [32]. The devices fabricated in this thesis use a more recent model, the donor/acceptor photovoltaic model.

Description of device physics falls into two categories, one internal and one external. The first section will examine photovoltaic devices from an electrical standpoint, or in terms of the produced current and voltage. This will lead to a thorough description of solar cell current-voltage characterization as a reference for the reader to aid in interpreting the plots in Chapter 4.

The second section will look at the internal workings of how photons enable charge transfer within a photovoltaic device. An overview of topics in modern physics is covered with emphasis on applications in charge transport within organic and inorganic semiconducting structures. We analyze a basic model of donor/acceptor photovoltaics and examine one of the most intriguing aspects of the type of solar cells which will be the subject of the rest of this thesis: the quantum dot. The chapter will conclude

with a discussion of external and internal quantum efficiency characterization.

2.1 A basic donor/acceptor solar cell

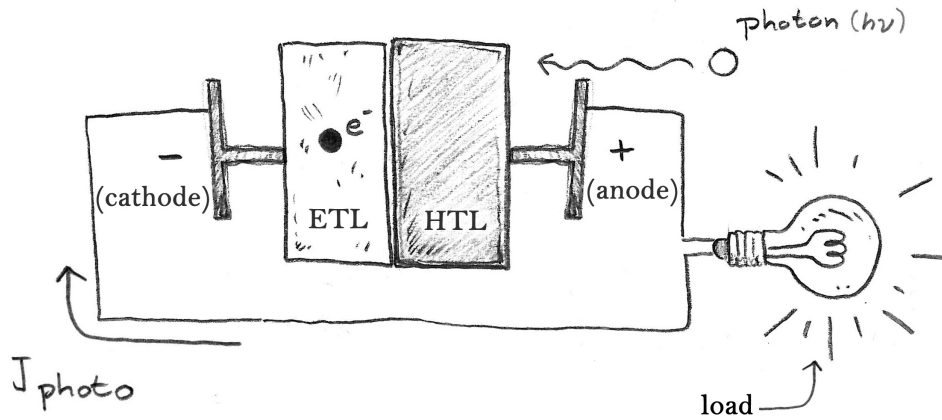


Figure 2-1: A simple donor/acceptor model solar cell consisting of an electron-transporting layer (ETL), a hole-transporting layer (HTL), and two electrodes (-,+). The solar cell uses photons to generate a photocurrent (J_{light}) that is sent through a load (lightbulb) in a simple circuit.

A simple diagram of a solar cell is drawn in Figure 2-1. It consists of one photon absorbing/hole-transporting semiconductor layer (HTL), one electron-transporting semiconductor layer (ETA), and a pair of charge-collecting metal electrodes. An electrode with a positive voltage (+) is called an anode and an electrode with a negative voltage (-) is called a cathode. A solar cell is similar to a battery in that it is able to drive current. However, a solar cell cannot operate without photons. Once the light source is removed, the solar cell is no longer able to generate current. A solar cell cannot store photons to use in the absence of light. This is the basic framework to keep in mind as we derive a more complex model of solar cell mechanics.

2.2 Solar cells and circuit analysis

In this first section, we will look at solar cells from an electrical point of view in order to set up a fundamental picture of how solar cells operate and define several important terms. We will initially treat the solar cell itself as an electrical black box, where the inner workings of the device are unknown and, for now, we simply accept that the behavior of the device in response to applied sunlight and voltage occurs as described.

2.2.1 But first, a bit of electronics

There are a few fundamental electronic concepts that must be understood in order to thoroughly appreciate how solar cell performance is characterized. Current and voltage are the first two. In a circuit, current always runs from regions of high voltage to regions of low voltage, or, more accurately, to regions of “lower” voltage. If we think of electric current as a stream of water, points of high voltage would be analogous to high ground and points of low voltage analogous to low ground. You can picture the stream naturally flowing downhill and it would go against your intuition to picture the water flowing against gravity to travel uphill. Voltage is always relative, meaning that the top of a hill is only considered to be “high” ground if the hill is not directly underneath the peak of a taller mountain, as in Figure 2-2. For example, +10 volts is “positive” relative to +5 volts, 0 volts, or -10 volts, but +10 volts is “negative” relative to +20 volts, +50 volts, or +1000 volts.

The word *voltage* is most often used in reference to a *difference* in voltage between two points in a circuit rather than the measure of a *single* voltage at one point. This is critical in that a voltage drop is what drives electric current. The following equation describes the relationship between voltage (V), current (I , or J for current density), and resistance (R):

$$V = IR$$

This equation is the foundation that the rest of electrical engineering and circuit

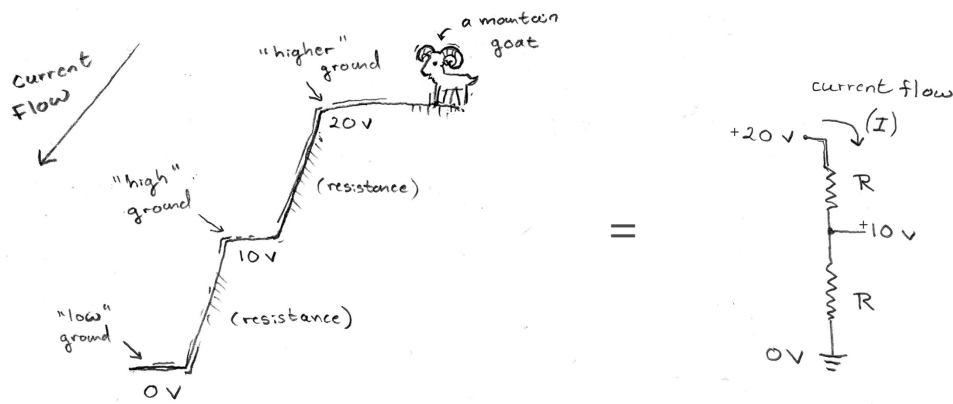


Figure 2-2: A model depicting current flow from high voltage to low voltage as down-hill slopes on a mountain river (left) and its analogous circuit diagram showing direction of current flow from 20 volts dropping across two resistors to 0 volts (right).

analysis is built upon. Without a difference in voltage, current cannot flow. When current encounters resistance in a circuit, such as when it runs through a resistor or a diode, this causes voltage to drop from one terminal of the resistant component, as is illustrated in Figure 2-3 with a black-box electronic component meant to symbolize any device which uses current to operate, such as a lightbulb or a light-emitting diode. A solar cell is able to build a voltage across itself while under illumination.

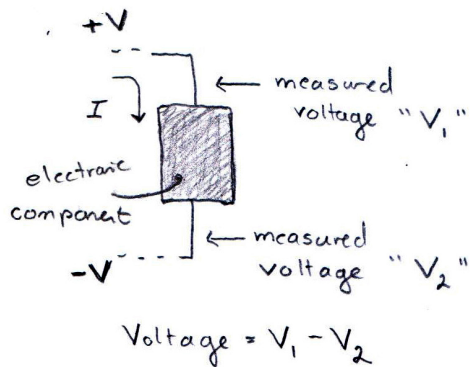


Figure 2-3: A section of a hypothetical circuit diagram, showing voltage driving current as a difference in measured voltages V_1 and V_2 at an electric load's input and output terminals. The "electronic component" can be any load which takes current, such as a lightbulb or a light-emitting diode (LED).

As a final note on circuit diagrams, Figure 2-4 shows the symbolic equivalents to a few elementary circuit components, a diode, a resistor, a load, and a power source. For further reading and a more thorough guide to circuit analysis, *The Art of Electronics* by Horowitz and Hill [35] is considered to be the so-called Bible of electronic references and is often used as a supplement to introductory electronics classes.

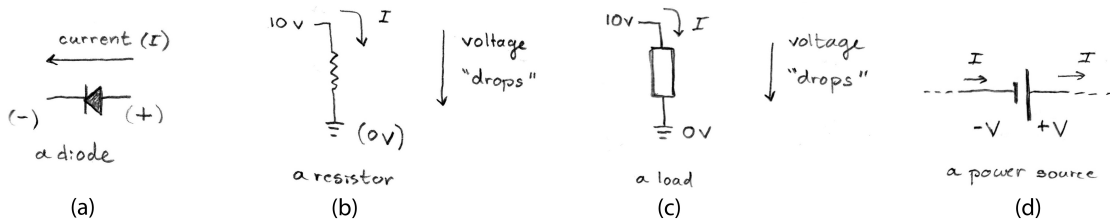


Figure 2-4: A few basic symbols used in circuit diagrams to represent electronic components: (a) a diode and (b) a resistor (c) a load and (d) a power source.

2.2.2 An electronic model of the solar cell

When a reference is made to the “current” and “voltage” of a device or electronic component, such as a solar cell, battery, or diode, this is referring to the current running through the component and the difference in measured voltage at each of the component’s terminals or electrodes. This is where solar cells become a bit complicated, because while a device’s photovoltage is relatively simple to measure, there are actually two currents, a photocurrent and dark current, which contribute to the net current said to be running through the device. An solar cell sitting on its own and isolated from a circuit produces no current when no light is shining on it, but current may flow when a voltage from an external power source is applied to a solar cell’s terminals while it is sitting in the dark. This external voltage is called a bias voltage, or simply a bias. Forward bias is when a voltage range is swept from 0 volts to a positive voltage. Reverse bias is when a voltage range is swept from 0 volts to a negative voltage.

Rudimentary definitions of the two types of photovoltaic currents are as follows:

Dark current is produced when a device is sitting in the dark by applying a bias to the device's electrodes. Dark current cannot flow without a bias. Even when light is shining, dark current is still present, as the solar cell is able to self-bias itself.

Light current is the current produced by the photovoltaic device while it is under incident illumination and is a combination of dark current and the **photocurrent** produced due to photon interaction with the photovoltaic's semiconducting materials. Photocurrent is dependent on the intensity of the incident light and independent of external applied bias at the solar cell's electrodes.

When a bias is applied to an illuminated solar cell, dark current may flow opposite or parallel to photocurrent depending on the value of the bias and the characteristics of the solar cell's semiconducting materials. The photocurrent and the dark current can run in the same direction and add to the device's net current, or they can run opposite to each other and subtract from the net current. The mechanics which enable light and dark current to flow are dependent on the physics which occurs as particles of charge move through the device and are affected by incident photons, as is discussed in Section 2.3. In this section, however, we will only focus on describing the electronic equivalent, which is only concerned with what a solar cell looks like from the outside, or what can be measured at its electrodes.

A photovoltaic is a combination of two components in parallel: a diode and a component which can produce current by absorbing photons, both illustrated in Figure 2-5. Dark current is primarily associated with the diode component of the solar cell. Photocurrent, and thus the light current, typically flows opposite to the direction of the dark current. Only when the solar cell is at certain voltages do the light and dark currents flow in the same direction.

Dark current characteristics

A diode is a semiconductor device that restrains current similar to how a valve may restrict the flow of water through a pipe [8]. Current will flow in one direction through

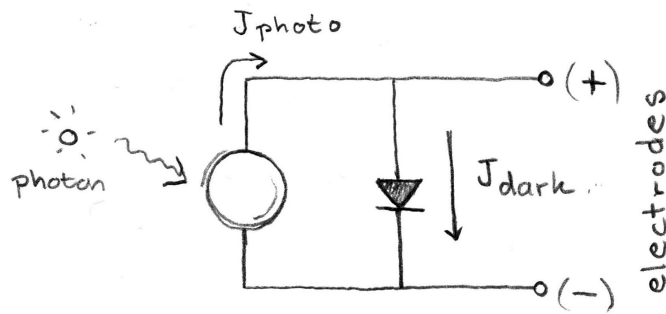


Figure 2-5: The circuit diagram equivalent of a solar cell showing both diode and photocurrent-generating components in parallel with the electrodes. The drawing is based off of Figure 1.7 from *The Physics of Solar Cells* [7].

a diode, from one set of electrodes to another, but the same diode will block current from flowing in the opposite direction. The non-linear relationship between a diode’s current and voltage are expressed in the following equation:

$$I(V) = I_s(e^{qV/kT} - 1)$$

where $I(V)$ and V are current and voltage respectively, q is electronic charge, k_B is Boltzmann’s constant, T is temperature in degrees Kelvin, and I_s is a constant value known as the saturation current which depends on the properties of the semiconducting material in the diode. The equation is visualized, likewise, as a non-linear current-voltage (IV) curve on a plot as shown in Figure 2-6. There is an exponential increase in current as forward bias increases until a “turn-on” voltage is reached, at which point a great deal of current begins to flow. This is attributed to the nature of the diode’s semiconductor device structure, and indirectly related to the $p-n$ junction in silicon solar cells and charge diffusion in donor/acceptor photovoltaics. The physics of diodes is described in Chapter 13 of Oldham and Schwartz’s *Electrical Engineering: An Introduction* [36], but will not be illustrated here as donor/acceptor photovoltaics do not follow the $p-n$ junction model. Little to no current flows through a diode in reverse bias until a relatively high negative voltage is applied, at which point the diode begins to break and allow current to flow in the opposite direction.

This renders the the physical component useless.

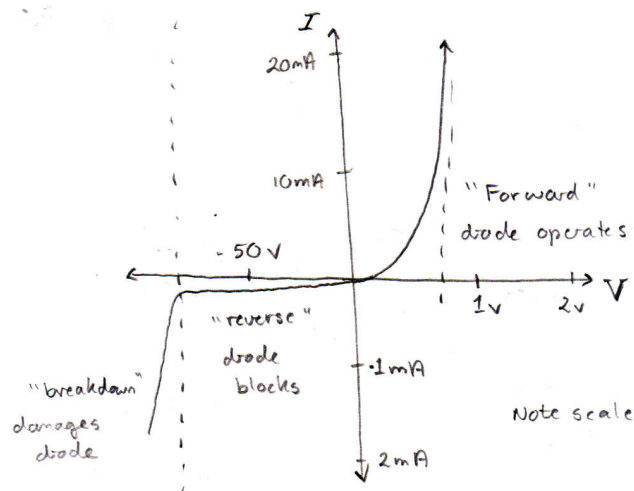


Figure 2-6: Graph adapted from Figure N3.9 in *The Student Manual for the Art of Electronics* [8] displaying current-voltage characteristics for an ideal diode.

The subsequent equation for dark current (J_{dark}) is similar to the above equation for current through a diode and is as follows:

$$J_{dark}(V) = J_o(e^{qV/k_B T} - 1)$$

where V is voltage, q is electronic charge, k_B is Boltzmann's constant, T is temperature in degrees Kelvin, and J_o is a constant value equivalent to the diode's saturation current I_s . The saturation current scales the equation according to how the properties of the asymmetrical junction between the semiconducting materials of the solar cell [7].

Light current characteristics

Light current also exhibits non-linear current-voltage characteristics. The photocurrent produced by a photovoltaic device is entirely independent of applied voltage and instead depends on how incident photons affect the semiconducting material within the device. Since a bias can also be applied to a solar cell in the light, light current

($J_{light}(V)$) is a combination of dark current and photocurrent, as is expressed in the following equation:

$$J_{light}(V) = J_{dark}(V) - J_{sc}$$

where $J_{dark}(V)$ is the dark current and J_{sc} is short-circuit current density under illumination. Dark current and light current typically run opposite to each other unless certain conditions are met. Current is comprised of positive charge moving in one direction and negative charge moving in the other. Traditionally, the orientation of current flow is relative to the direction positive charge is moving in. Positive current ($+I$) flows from positive to negative voltage (anode to cathode on the solar cell). This makes the photocurrent, and thus the light current, negative by comparison ($-I$) and flowing from the negative to positive voltage (cathode to anode on the solar cell). Sign convention for light and dark current changes depending on the source one is reading. For instance, Nelson writes that it is standard to designate light current as positive and dark current as negative (i.e. $J_{light}(V) = J_{sc} - J_{dark}(V)$) [7], but other texts use the opposite notation for light and dark current [6] [14].

2.2.3 Solar cell power efficiency and current-voltage characterization

Current and voltage are both needed to produce power, as is expressed in the classic electronics equation:

$$P = IV$$

A solar cell cannot produce power unless it exhibits both current and voltage. Therefore, a solar cell's performance can be analyzed by compiling data on resultant output current and voltage as is measured at the device's electrodes. The resultant plot is an IV curve. A typical current-voltage curve for a photovoltaic device is sketched in Figure 2-7. The orientation of the light current is negative and runs opposite to the

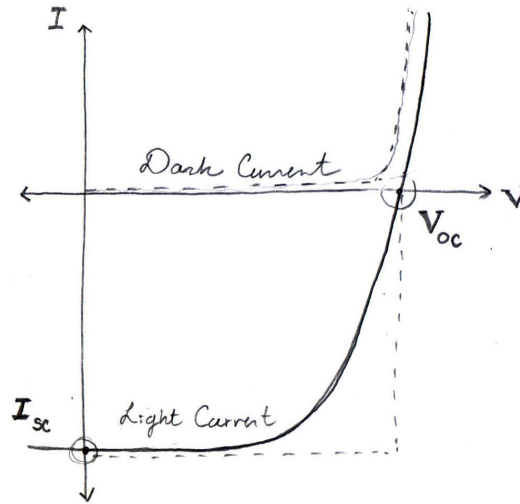


Figure 2-7: A sketch of the light (solid line) and dark (dashed line) current-voltage characteristics observed by a hypothetical photovoltaic with open-circuit voltage (V_{oc}) and short-circuit current (I_{sc}) points labeled.

dark current until the light current curve reaches the x-axis, at which point photocurrent stops flowing and then reverses so that the light current then runs in the same direction as the dark current.

There are two specific instances when an illuminated solar cell is producing no power:

Short-circuit current The first instance is when the solar cell is generating current but no voltage. This occurs when the solar cell's anode and cathode terminals are directly connected in a short circuit, with zero resistance between them, and the resulting current is appropriately termed the short-circuit current (I_{sc} or J_{sc} , where J_{sc} is typically reserved for short-circuit current density).

Open-circuit voltage The second instance is when the solar cell is producing voltage but no current. This occurs when the solar cell's electrodes are isolated from each other and the resulting voltage is termed the open-circuit voltage (V_{oc}). A solar cell that is sitting in the light, not connected to any external circuit, will exhibit an

open-circuit voltage.

Together, I_{sc} and V_{oc} give the theoretical maximum power that the device should be able to produce. An ideal device will generate light current at I_{sc} until the applied bias approaches V_{oc} , at which point the amount of current decreases exponentially until there is not current at all and maximum voltage V_{oc} is achieved. For applied biases greater than V_{oc} , the flow of photocurrent will switch and light current will run in the same direction as the dark current. The total light current should follow the shape of a ninety-degree angle with a rounded corner where the exponential decay occurs, as can be seen in Figure 2-7. However, when current leakage occurs, usually due to device defects, the angle becomes less pronounced, as can be seen in Figure 2-9. The better an experimental device is, the squarer its light current curve will be. Section discusses how internal resistance will distort IV curves.

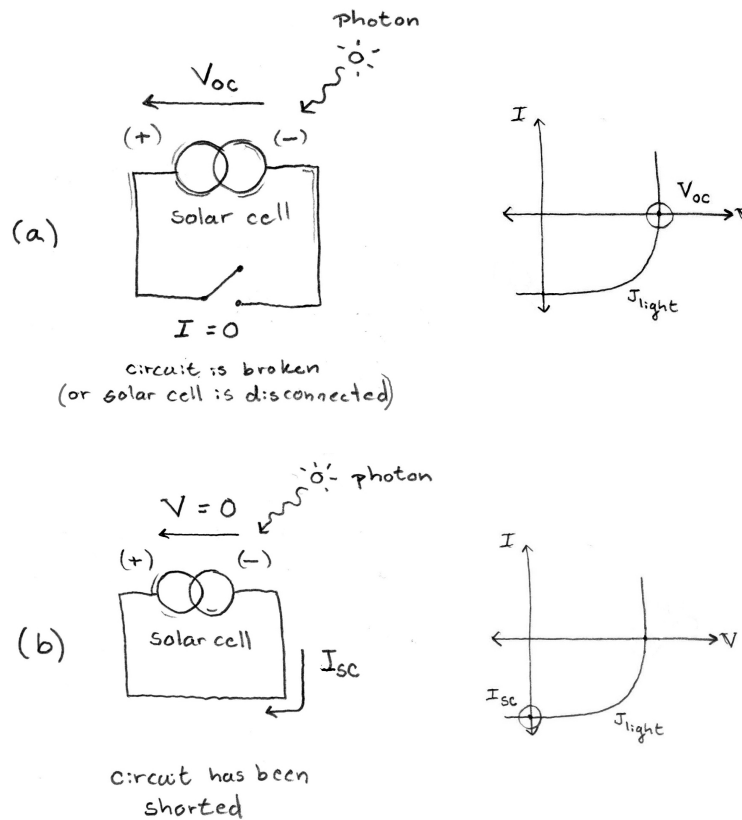


Figure 2-8: Light current plots showing equivalent circuit conditions for (a) open-circuit voltage (V_{oc}) and (b) short-circuit current (J_{sc}).

2.2.4 Plotting the current-voltage characteristics of a solar cell

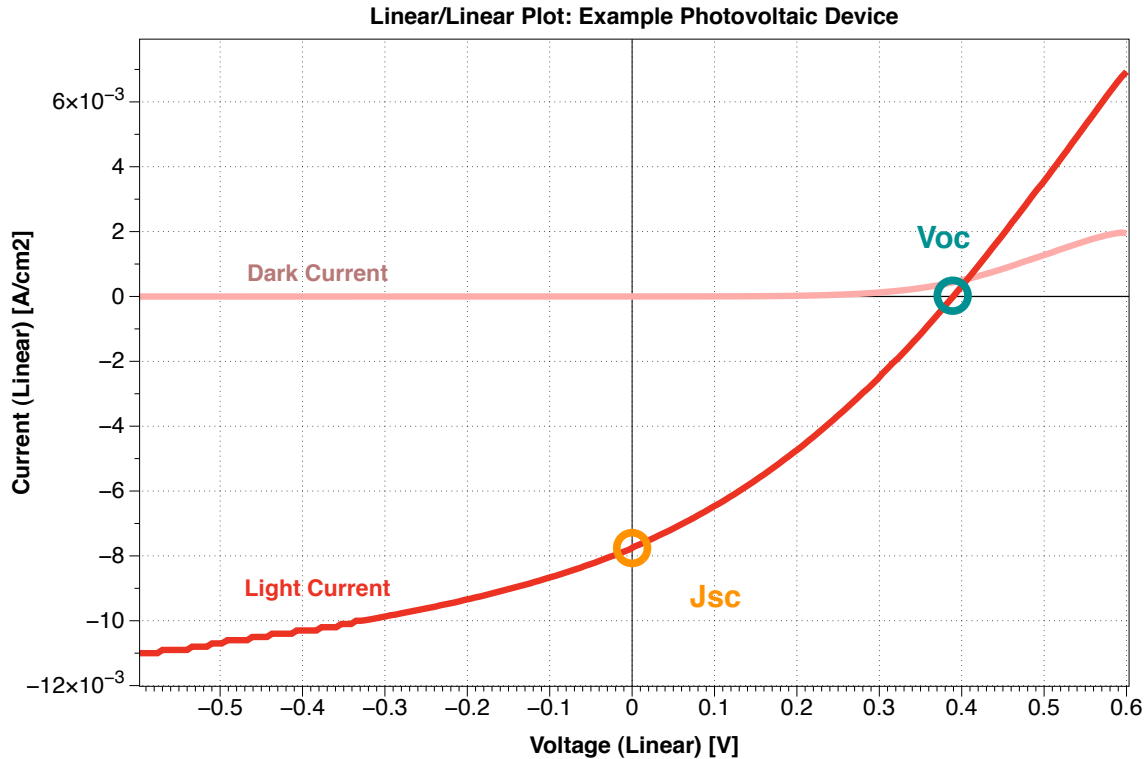


Figure 2-9: A typical current-voltage curve for a photovoltaic device with short-circuit current and open-circuit voltage labeled. Current and voltage are both scaled linearly. The data used in this and the following four plots is from the control device in set 20100628 from Section 4.1.

When a solar cell is tested, current density output is typically measured in milliamperes per centimeter squared (mA/cm^2) for each point of voltage in a bias sweep applied to the solar cell's electrodes. There are a few different ways that data from a photovoltaic's current-voltage curve can be presented depending on how the data points are scaled. Shown below are different ways of plotting the light and dark current of the control device from the set of experimental devices 2010628 in Section 4.1. The following section will familiarize the reader with the most important IV curve components in order to better understand the figures presented in Chapter 4.

The simplest, and most familiar, way of plotting the current-voltage curve from a

photovoltaic device is shown in Figure 2-9 with the current and voltage axes scaled linearly. Photocurrent runs opposite to dark current until the device reaches open-circuit voltage (V_{oc}), at which point the direction of the photocurrent switches and begins to flow in the same direction as the dark current. Light current is a combination of the photocurrent which is produced while a solar cell is illuminated and the underlying dark current which runs when the solar cell has a bias applied to its electrodes. Short-circuit current (J_{sc}) is then a single measurement of photocurrent only, with no bias, or 0 V, applied and thus takes no measure of dark current into account. The total current in the cell, with respect to the cell's voltage, or $J(V)$, is defined in terms of short-circuit current density and dark current in the following equation:

$$J(V) = J_{dark}(V) - J_{sc}$$

where $J_{dark}(V)$ is the dark current, shown in light pink in Figure 2-9, and $-J_{sc}$ is the photocurrent produced by the intensity of the light hitting the solar cell, a point circled in orange in Figure 2-9. V_{oc} is the point where photocurrent and dark current are equal and opposite to each other so that

$$J_{dark}(V) - J_{sc} = 0$$

Fill factor (FF) is a value which relates the total amount of power that a solar cell can theoretically produce ($P_{theoretical} = J_{sc}V_{oc}$) to the maximum power that the device can actually produce upon testing ($P_{max} = J_mV_m$). The fill factor (FF) for a linear/linear solar cell plot can be easily determined by picking the point on the light current curve that maximizes the value of JV , or coordinates of the light current curve's absolute maximum. The maximum power point for the curve in Figure 2-9 is approximated by the purple point shown in Figure 2-10 along with the corresponding values for current and voltage, J_m and V_m . Fill factor is defined as:

$$FF = \frac{J_m V_m}{J_{sc} V_{oc}}$$

Fill factor can be visualized as the ratio between the two rectangles in Figure 2-10. The purple rectangle shows the solar cell's power in terms of J_m and V_m and the green rectangle represents the solar cell's theoretical maximum power, represented by J_{sc} and V_{oc} .

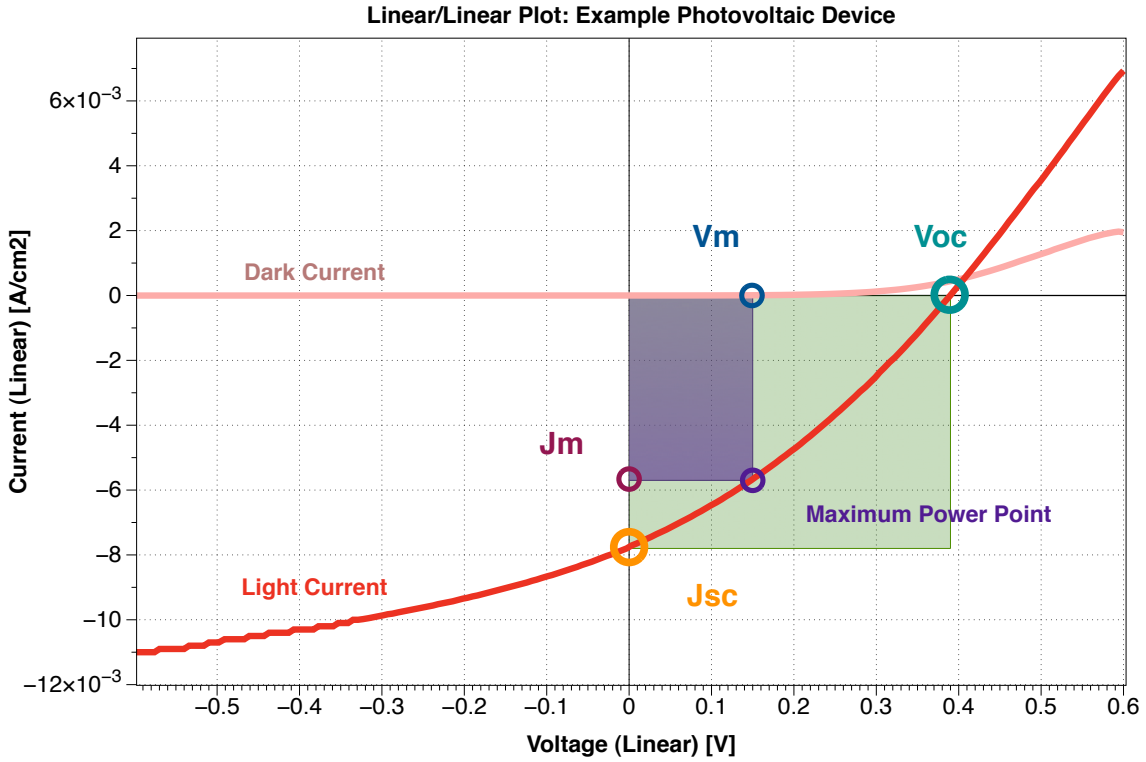


Figure 2-10: A typical current-voltage curve for a photovoltaic device. A device's fill factor is determined by taking the ratio between $P_{theoretical} = J_{sc}V_{oc}$ (the large rectangle shown in green) and $P_{max} = J_mV_m$ (the small rectangle shown in purple). Current and voltage are both scaled linearly.

Solar cell efficiency η is determined by the following equation:

$$\eta = \frac{Power_{in}}{Power_{out}} = \frac{J_m V_m}{P_{solar}} = \frac{J_{sc} V_{oc} FF}{P_{solar}}$$

where P_{solar} , or $Power_{out}$, is the power contained in the incident photons. The value of P_{solar} is usually equal to 100 mW cm^{-2} [32].

Efficient solar cells have a fill factor close to 1, or a square-ish light current curve that follows the outer boundary of the rectangle formed by J_{sc} and V_{oc} as shown

in Figure 2-7. The device which produced the light current curve in Figure 2-9 is obviously not very efficient. The dark current curve resembles that of a diode.

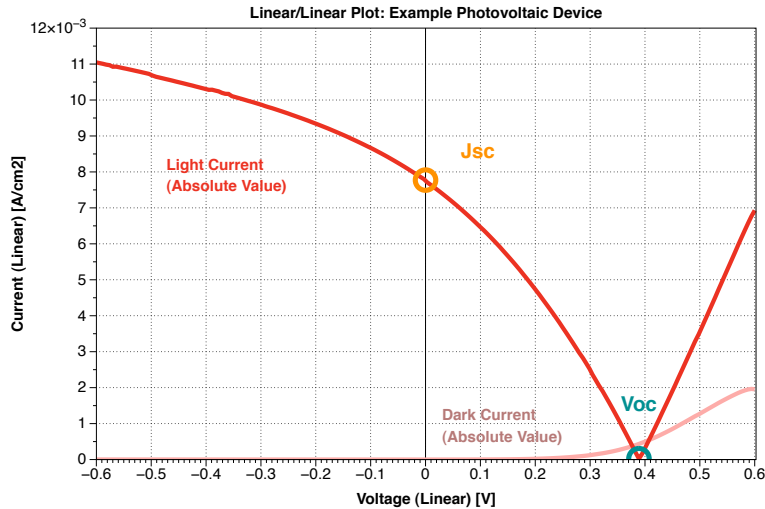


Figure 2-11: An atypical current-voltage curve for a photovoltaic device using the absolute value of all points in both light and dark current curves. This plot is a transition step between showing current and voltage scaled linearly and scaled logarithmically.

Current-voltage characteristics for photovoltaics can be shown in logarithmic plots to emphasize the nonlinear attributes of the curve. Since the logarithm of a negative number is a non-real value, negative values cannot be plotted logarithmically alongside positive values. Before either axis can be scaled, the absolute value is taken for all of the data points in light current curve, the result shown in Figure 2-11. The plot seen in Figure 2-11 is quite irregular and never seen in publications as it contains the same data seen in Figure 2-9 without acknowledging the switching orientation of the light current, but in the event of plotting data from a photovoltaic device, it is useful to be able to recognize this plot for what it is.

When the current in Figure 2-11 is scaled logarithmically, the dark and light current curves are illustrated as shown in Figure 2-12. The dark current curve, which could barely be detected in the previous plots, is now fully unfolded so that subtler values of current can be seen. There is a sharp dip in the dark current curve. Also important in Figure 2-12 is that the device's open-circuit voltage and short-circuit

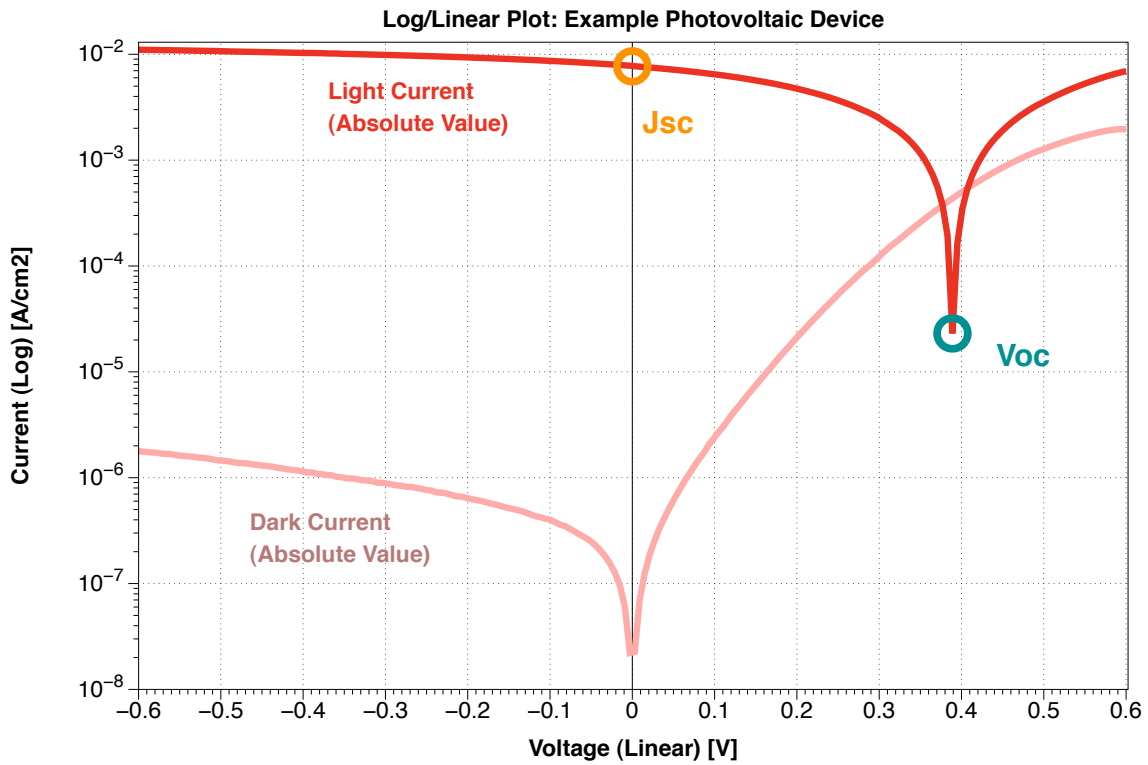


Figure 2-12: A typical half-log current-voltage plot for a photovoltaic device. All values along the dark current curve can clearly be seen alongside the shape of the light current curve. Current is scaled logarithmically and voltage is scaled linearly.

current are still prominent characteristics and can be used as the cornerstones for comparing the performances of different devices. The one downside is that there appears to be some photocurrent generated at V_{oc} , clouding the point's significance. This can cause confusion if the reader is unfamiliar with the original presentation of the data in Figure 2-9, where there is no question that the light current curve passes through the x-axis and photocurrent stops when the device is at this certain voltage, V_{oc} . The log/log plot shown in Figure 2-12 will be used in the experimental section of this thesis, Chapter 4, to show the device's current-voltage behavior in the light and dark.

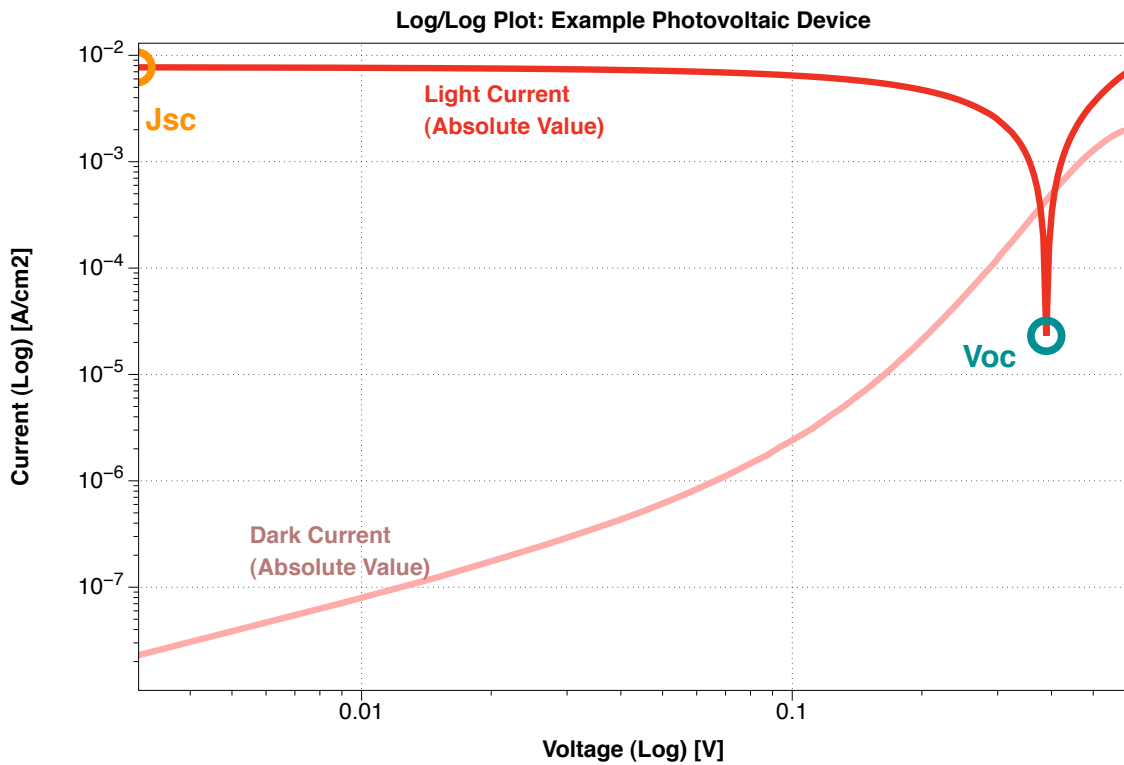


Figure 2-13: A typical current-voltage curve for a photovoltaic device. Both current and voltage are scaled logarithmically.

A third way to display current-voltage data is shown in Figure 2-13 where both current and voltage are on a logarithm scale. This returns the dark current curve to its diode-like shape, similar to Figure 2-9, but the dark current remains a prominent

feature of the plot.

Internal resistance

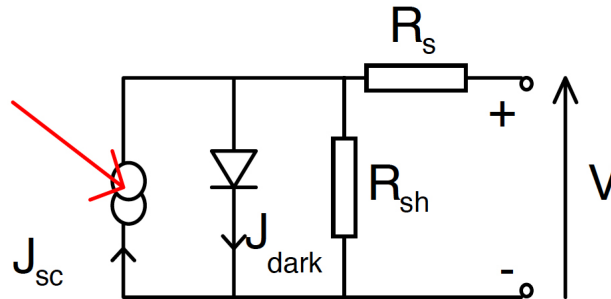


Figure 2-14: Shown is a circuit diagram of a solar cell with shunt resistance (R_{sh}) and series resistance (R_s) from Figure 1.10 of *The Physics of Solar Cells* [7]. In an efficient cell, $R_s = 0$ and $R_{sh} = \infty$.

There are two kinds of internal resistance within a solar cell that affect its performance. Figure 2-14 shows a circuit diagram of a solar cell with series resistance (R_s) in series with the device and shunt resistance (R_{sh}) parallel to the device. Shunt resistance is considered to be good for a device to have because it prevents an unwanted short circuit from forming across the device. Series resistance is bad for photovoltaics because it stops light and dark current from properly flowing across the cell. An efficient solar cell will have low series resistance and high shunt resistance.

Note how the light current curve in Figure 2-9, if inverted, more closely resembles a combination of plots (a) and (b) in Figure 2-15 than Figure 2-7. Clearly the experimental device which produced the plot in Figure 2-9 is experiencing some current leakage through internal resistance.

2.3 Donor/acceptor photovoltaics

Now that the basic principles of solar cell operation have been laid down, we can remove the black box and properly discuss the internal physical and chemical mecha-

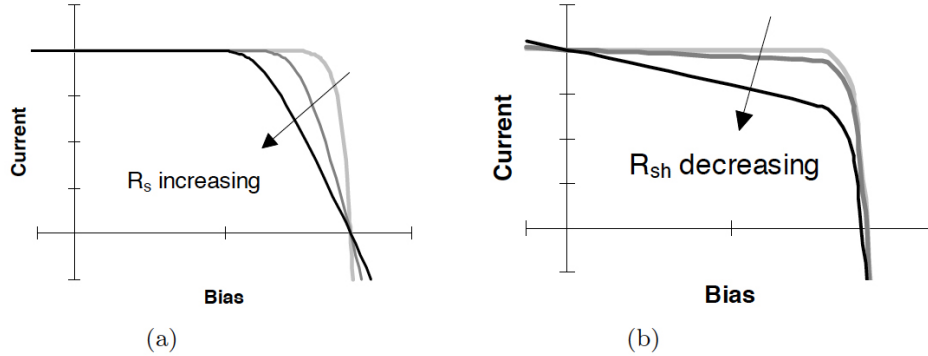


Figure 2-15: Shown are how a solar cell's light current curve is affected by series resistance (a) and shunt resistance (b), from Figure 1.11 of *The Physics of Solar Cells* [7]. Note that the current axis has been adjusted so that the direction of the photocurrent is positive and the direction of the dark current (not shown) is negative.

nisms which allow solar cells to turn photon energy into electrical power. Dissecting the innards of a photovoltaic device involves looking at the bandgap theory of semiconductors and how charge particles are atomically inclined to act. A simple model of a donor/acceptor solar cell will be outlined here, following the steps from excitation generation to current output. We will start with one of the most fundamental concepts of modern physics.

2.3.1 The photovoltaic effect

The photovoltaic effect is a phenomena which was first observed by the French physicist Alexandre-Edmund Becquerel through experiments with electrolyte cells [37]. Becquerel found that when he shone light on a sample of silver-coated platinum suspended in an electrolyte, he could measure electric current coming from the device [14]. The photovoltaic effect is the act of a voltage accumulating across a piece of material when exposed to a light source. It is the fundamental principle that allows a photovoltaic device, such as a solar cell, to generate free charge carriers and drive them through a circuit at as electric current.

In order to better appreciate the photovoltaic effect, it would be useful to look at

a model of a particle of charge. A particle such as an electron is naturally inclined to exist in states that give the electron the least amount of energy. The energy of an electron is measured in units of electron volts (eV), where 1 eV is approximately 1.60×10^{-19} joules (J). The electron may have only certain, specified quantities of energy and not contain amounts that fall in-between. This is known as quantization.

Each state that the electron can exist in is defined as an energy level. Each energy level can be thought of as rungs of a ladder or steps on a staircase. The lowest energy state is known as the ground state. If enough energy is added to the electron, it will be able to jump to the next energy level as shown in Figure 2-16, leaving behind a positively-charged space called a hole. When the electron loses this energy, releasing it in the form of radiation, it will fall back to its lower, more natural state.

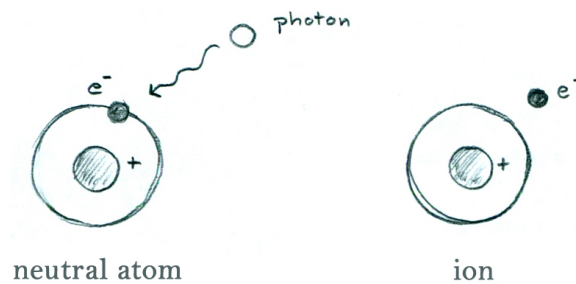


Figure 2-16: Sketch of a photon transferring its energy to an electron in an atom's highest occupied molecular orbital (right), enabling the electron to pop out of its orbital. The resulting positively-charged ion (specifically, a cation) and free-moving negative charge carrier are shown on the left.

Electrons may gain energy when they come in contact with other particles. Particles of light, called photons (γ), contain energy which is transferred to the particles of the material it strikes. Light can also be characterized as a wave. The energy contained by the wave of light is a property of wavelength. The two are related by the following equation:

$$E(\text{eV}) = hv = \frac{hc}{\lambda(\text{nm})}$$

where E is energy in electron volts (eV), v is angular frequency, λ is wavelength in

nanometers (nm), h is Planck's constant, and c is the speed of light. Electrons are found in the atoms of all materials. When a photon of light strikes a material, it transfers its energy to the electrons in the material. This may give the electron the energy it needs to jump to the next energy level, or to completely escape from confinement to the surface of the material. When an electron escapes from the highest occupied molecular orbital (HOMO) of an atom, it enters the atom's lowest unoccupied molecular orbital (LUMO). When many atoms are arranged together to form a material, the individual HOMO and LUMO levels, often minutely offset from each other, may be approximated as bands. The empty region between a material's HOMO and LUMO level, where no electron or hole can exist, is called a bandgap.

Exciton generation

A special case of electron excitation occurs when an electron is excited to a higher energy state, but remains physically attached to the hole it is trying to escape from. A Coulombic attraction keeps the negatively charged electron and positively charged hole bound together. Figure 2-17 shows the bandgap diagram of this scenario, wherein the electron is inhabiting a different energy level than its hole counterpart, but still feels a connection through the energy gap since the two remain bound in the same physical space.

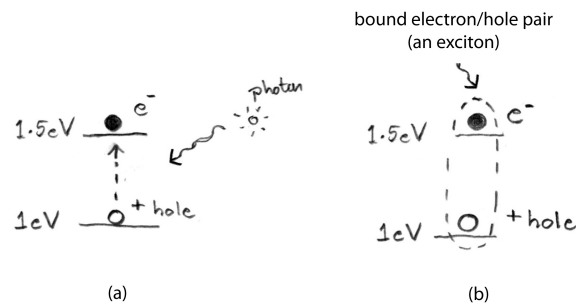


Figure 2-17: Illustration of (a) an electron gaining energy from an incident photon, leaving behind a hole in the lower energy state and (b) the bound electron-hole pair, called an exciton

A bound electron-hole pair is called an exciton. Once generated, an exciton's

existence is fragile. The electron will see the hole as a more appealing energy state and it is only a matter of time before the electron relaxes, releasing the extra energy and falling back down. The exciton then annihilates as the negative and positive charges recombine. This is the fate of most excitons and is a common occurrence even in the most efficient solar cell. However, under a certain set of circumstances, the exciton can be convinced to separate and lend the electron and hole to current generation.

2.3.2 Using bandgap offset to transport charge

Although many different types of photovoltaic devices were described in Chapter 1, each one operates in a similar fashion. Light is absorbed by a photon-absorbing material inside the device and the incident photons generate either free charge carriers within the solar cell's semiconducting materials or a bound electron-hole pair called an exciton. The donor/acceptor model is used to describe solar cells that have exciton formation upon contact with incident photons. Once an exciton is generated within the photon-absorbing material, the next step is to use a combination of photovoltaic materials to coax the exciton into separating before it annihilates.

A donor/acceptor solar cell is typically built out of two materials, the electron-transporting layer (ETL) and the hole-transporting layer (HTL). In a photovoltaic device, materials are chosen based on the offset between their HOMO and LUMO levels, so that when the two materials are placed together, their bandgaps form a sort of staircase in energy space, as seen in Figure 2-18. Energy space diagrams are drawn with regions of lower energy at the bottom and regions of higher energy at the top. Electrons are more inclined to go down in energy whereas holes are more inclined to go up. When two different materials are placed together, the plane of contact is called a heterojunction. If a particle of charge in one material happens to come close to the heterojunction, it will cross the barrier and enter the joining material if it finds that doing so will enable it to transfer to a more favorable energy state. Holes will cross the heterojunction if they find they will go up in energy by doing so and electrons will cross the heterojunction if they find they will go down in energy.

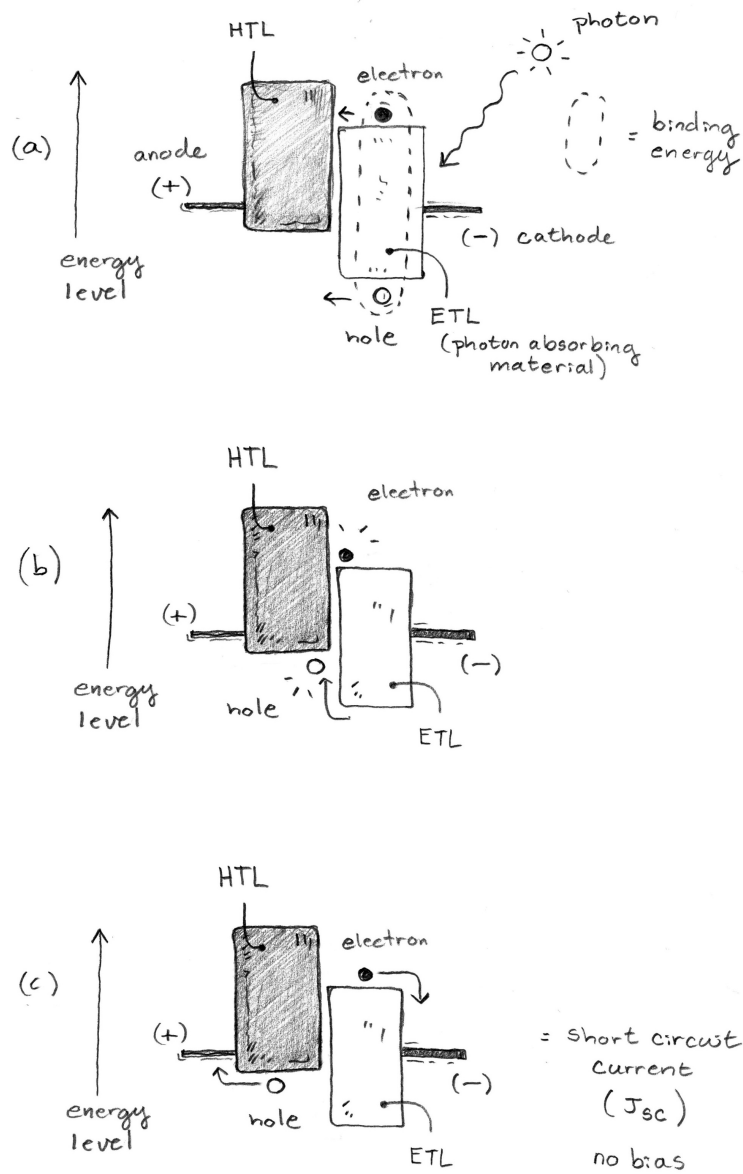


Figure 2-18: A sketch depicting (a) exciton generation from an incident photon and diffusion towards the heterojunction (b) exciton separates as the hole crosses the heterojunction to a higher energy state in the hole transporting layer (HTL) and (c) electron and hole move as free charge carriers across their respective transport layers to transfer their charge to opposing electrode.

This is also illustrated in the three parts of Figure 2-18, showing the lifecycle of an exciton. The exciton is generated in the photon-absorbing, electron-transporting material on the left in Figure 2-18 (a). The exciton then diffuses within the material, carrying both bound positive and negative charge with it, until it reaches the heterojunction. Figure 2-18 (b) shows that the exciton's hole sees a way to jump to a higher energy state and so it does, crossing the heterojunction into the hole-transporting layer (HTL). The electron will attempt to follow the hole, but entering the HTL requires going up in energy. The electron finds that the Coulombic attraction keeping it bound to the hole is not strong enough to get it over the barrier. The exciton splits apart, rendering the electron and hole as separate, free-moving entities within their respective materials. In Figure 2-18 (b), the hole has been donated by the ETL and accepted by the HTL.

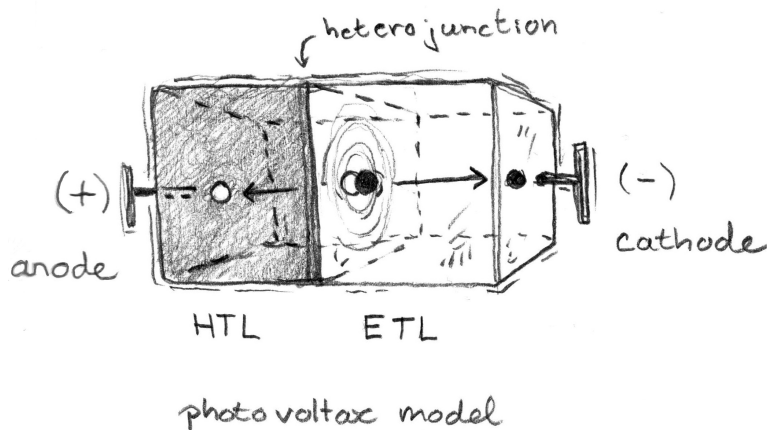


Figure 2-19: A physical approximation of exciton separation at the junction between a hole-transporting layer (HTL) and electron-transporting layer (ETL) in a model photovoltaic device. The exciton splits as the hole (white circle) crosses the barrier into a more favorable energy state and leaves behind its companion electron (black circle).

Figure 2-18 (c) shows the final step in current generation within a donor/acceptor solar cell where the electron and hole diffuse towards opposite ends of the device. A cathode is attached to the opposite end of the ETL to collect negative charge and an anode is attached to the opposite end of the HTL to collect positive charge. As

charge collects, a difference in voltage develops across the device. This voltage will then drive electric current when the device is put into a circuit.

A simple, physical model of exciton separation at the heterojunction of a donor/acceptor solar cell is shown in Figure 2-19, with an exciton separating at the center of the device.

Solar cell efficiency is determined by how effective a device is at translating photon-generated excitons into electric current. The more excitons that annihilate before they can separate at the heterojunction, the less efficient the device. Bandgap architecture and material thickness are both key to solar cell design.

2.3.3 Expressing light and dark current in terms of bandgaps

The first half of the chapter defined light and dark current as the two types of current found in a solar cell under illumination and under bias. When the electrodes of a solar cell become biased, either from an external power supply or self-biasing, the change in voltage affects the composition of the bandgaps. This section presents only a brief description of how dark current and light current are able to flow, using Figure 2-20 to illustrate how a donor/acceptor solar cell's bandgaps are affected by forward and reverse bias across the solar cell. One note to keep in mind about the bandgap diagrams in Figure 2-20 is the orientation of positive and negative in energy space. The more positive an electrode is, the closer it is to the bottom of the diagram and the more negative an electrode is, the closer it is to the top.

Figure 2-20 (a) shows the bandgap diagram of forward bias dark current while the solar cell is not under incident illumination. In the dark, a solar cell will not produce current until a voltage is applied from an external source. When a forward bias is applied, the electron-collecting cathode becomes more negative than the hole-collecting anode. The negative status of the cathode bends the ETL and HTL bands to signify that it is easier for electrons to overcome the high energy barrier of the HTL than it is to overcome its Coulombic repulsion from the negative charge collected on the cathode. The reverse is true for holes, as they are similarly repulsed by the positive charge on the anode and that enables them to overcome the low energy barrier of the

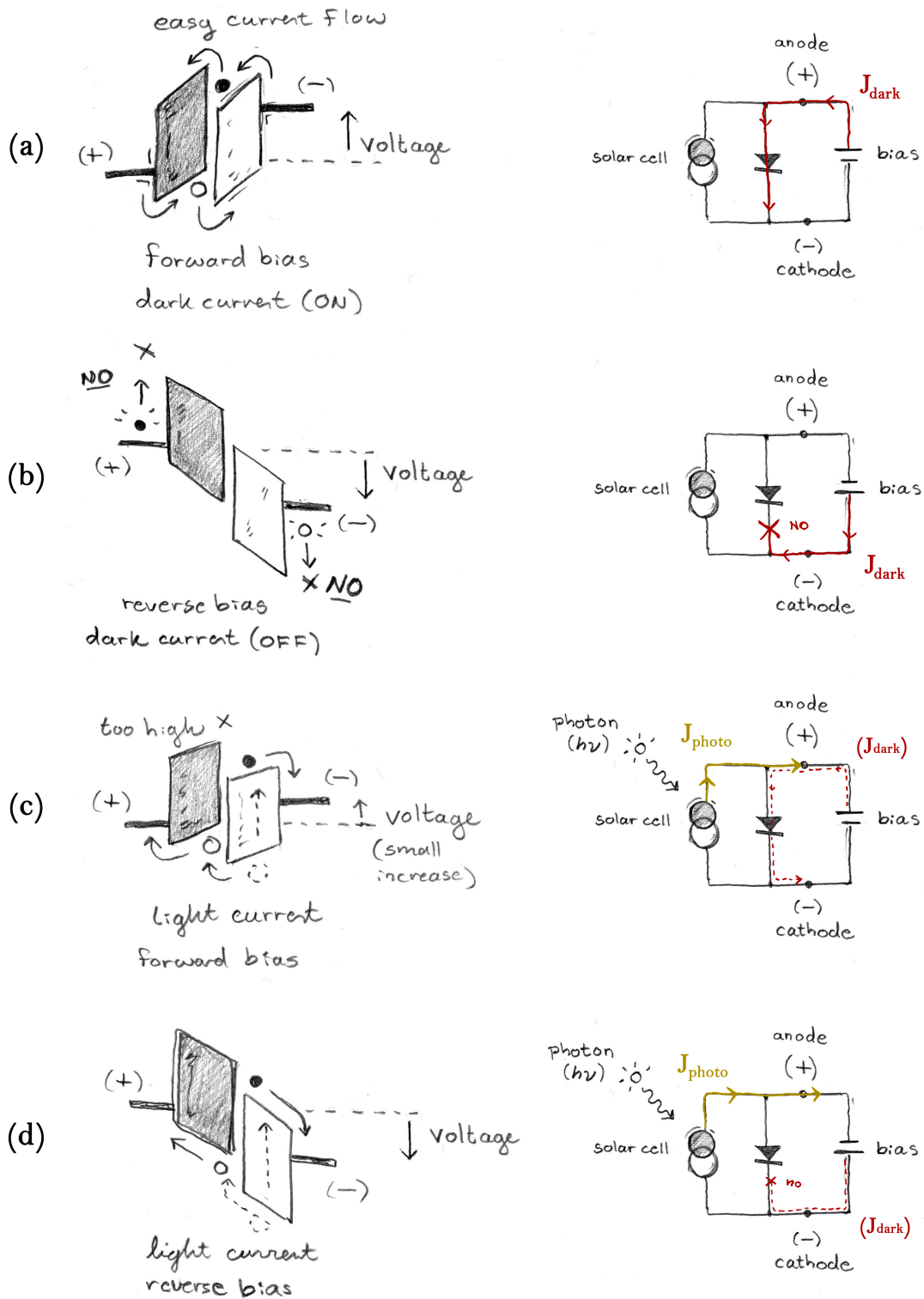


Figure 2-20: Diagrams illustrating how applying forward and reverse bias affect the bandgaps of a photovoltaic's ETL and HTL (left) and the current flow through equivalent circuit diagrams (right). Shown is (a) J_{dark} under forward bias (b) J_{dark} under reverse bias (c) J_{photo} under forward bias and (d) J_{photo} under reverse bias.

ETL. Dark current flows from anode to cathode.

Figure 2-20 (b) shows the bandgap diagram of reverse bias dark current while the solar cell is not under incident illumination. A reverse bias on a solar cell in the dark will cause the cathode to become more positively charged than the anode. The resultant band-bending shows that this goes against the intended structure of the photovoltaic device. The electrons and holes will become stuck at the electrodes, attracted to electrodes with opposite charge, and unable to overcome the energy barrier that would complete the current's circuit. Dark current attempts to flow from solar cell cathode to anode, but it is blocked.

Figure 2-20 (c) shows the bandgap diagram of forward bias photocurrent while the solar cell is under incident illumination. When photons strike a photovoltaic device in forward bias, the cathode is lower in voltage than the anode, but unlike Figure 2-20 (a), the cathode is not so negative as to be unfavorable when compared to the barrier the electron encounters at the heterojunction. In light current forward bias, the energy it would take to overcome the barrier is greater than the energy it takes to overcome the negative charge on the cathode. Holes find themselves in a similar situation where they are more inclined to travel in the direction of the positively-charged anode than to cross the heterojunction into a region of lower energy. Therefore, photocurrent flows from cathode to anode.

Figure 2-20 (d) shows the bandgap diagram of reverse bias photocurrent while the solar cell is under incident illumination. Unlike the dark current in Figure 2-20 (b), where charges get stuck, new charge carriers are constantly being generated in the photon-accepting layer. A reverse bias favors current flow from photogenerated charges and photocurrent flows from cathode to anode.

2.3.4 Quantum dots

A quantum dot is a tiny amount of semiconducting material. A quantum dot of lead sulfide is modeled in Figure 2-21 showing a typical diameter and spherical arrangement of molecules. Quantum dots are small enough to confine individual electrons or holes which leads to strange quantized effects in descriptions of the semiconductor.

The quantum dot is the zero dimensional equivalent of the notorious “particle in a well” problem from quantum mechanics. The particle, an electron in our case, is confined in all spacial dimensions.

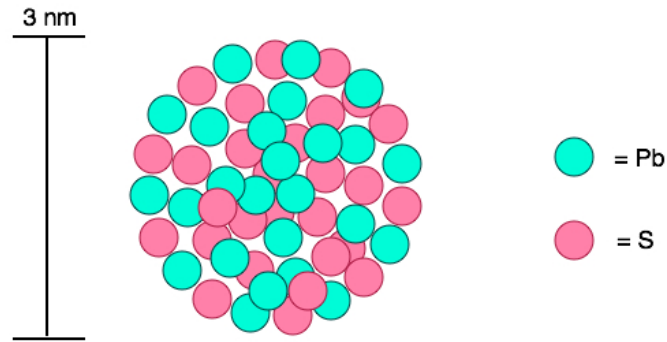


Figure 2-21: Sketch of a quantum dot made up of atoms of lead and sulfide (PbS).

2.3.5 Size and tuneability

Dots with greater radii absorb photons of lower energy. Lower energy corresponds to longer wavelengths of light. As the diameter of the quantum dot is compressed, the wavelength of photons that the dot may absorb and emit decreases. The smaller the wavelength, the greater the energy transmitted by the wave and its particle equivalent. This correlation occurs because the size of the dot controls the bandgap of the material it is made of. For instance, a decrease in diameter for cadmium selenide quantum dots will cause them to emit and absorb smaller wavelengths of light, which translates to “bluer” colors. Figure 2-22 shows two vials that contain cadmium selenide quantum dots of different diameters. The vial on the left contains quantum dots that are fluorescing in yellow and thus are smaller in diameter than the vial of quantum dots on the right that are fluorescing in red.

The size of the dot is determined during the formation process. Quantum dots can be grown in two ways: epitaxially, dot by dot like building blocks, or synthesized. A number of controllable factors during the synthesis process determine the diameter

of the dot. A detailed explanation of lead sulfide quantum dot synthesis is included in Appendix A.

Wavelengths or packets of energy absorbed and emitted also depend on the materials that the dot itself is made of. For example, a lead sulfide quantum dot about 2.3 nm in diameter may emit wavelengths around 850 nm, but a cadmium selenide quantum dot of the same size will emit different wavelengths.

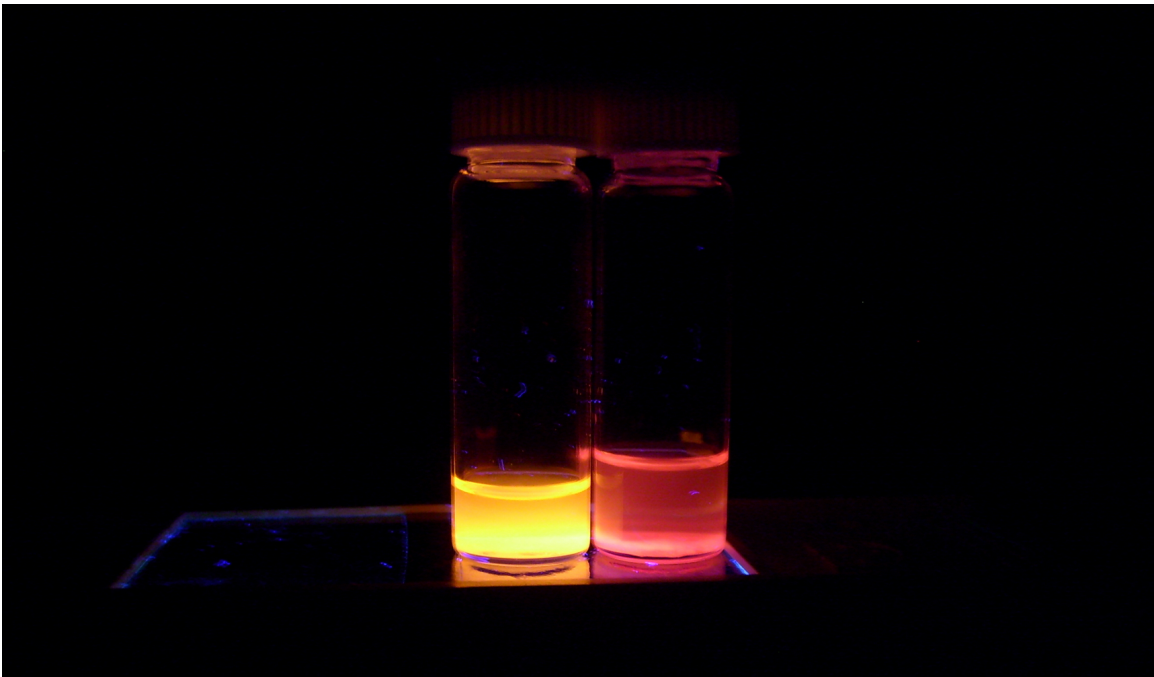


Figure 2-22: Two vials of cadmium selenide (CdSe) quantum dots under a UV lamp, synthesized under the supervision of Darcy Wanger in the Bawendi Lab.

2.3.6 Charge transport and quantum tunneling

Each dot specifies the region where a particle of charge, such as an electron, can exist. Within this sphere is a certain probability that the particle will exist. Since the particle wavefunction cannot come to an abrupt, crisp end, there is exponential decay outside of the dot. If the particle pops out of the boundary of the dot, through an effect known as quantum tunneling, it stands a chance of popping back into existence within the boundary of a neighboring dot. The charge can continue to travel in this

way, from dot to dot, and this forms the basic idea of electric current through a semiconducting material.

Ligands are chains of molecules which bond to other molecules. Every ligand has a pair of unshared valence electrons in the outermost orbital ready to bond with other molecules. In solution, these ligands will bind to the outermost atoms of the quantum dot, restricting the quantum dot's growth and its ability to share electrons of charge with neighboring dots. While this is not ideal for use in a solar cell, these long ligands keep the quantum dots preserved until they are ready to be used in a device. These long ligands are exchanged with smaller ligands during the spin coating process in device fabrication, explained more in Section 3.4.

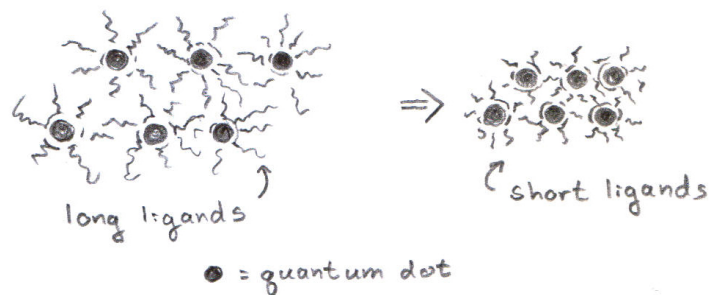


Figure 2-23: Quantum dots suspended in solution showing long ligands (left) exchanged for shorter ligands (right) during the chemical “crash out” process.

2.3.7 Solar cell quantum efficiency characterization

When light strikes a photovoltaic device, current is generated because, ideally, each photon that hits the material should be absorbed and the energy that was contained in the photon should be used to create free-moving carriers of electric charge. Experimentally, not every photon that strikes a solar cell is absorbed and not all absorbed photons are able to generate free charge carriers. Quantum efficiency measures how well a photovoltaic device is able to convert incident photons into electric current, as seen in Figure 2-24.

There are two types of quantum efficiency, external and internal. External quantum efficiency (EQE) is a ratio between the number of negative charge carriers, or electrons, generated in the device to the number of photons shining on the device. External quantum efficiency is described by the following equation:

$$EQE(E_v) = \frac{\text{Electrons generated}}{\text{Incident photons } (E_v)}$$

where E_v is the energy of a single incident photon and electrons generated is a number.

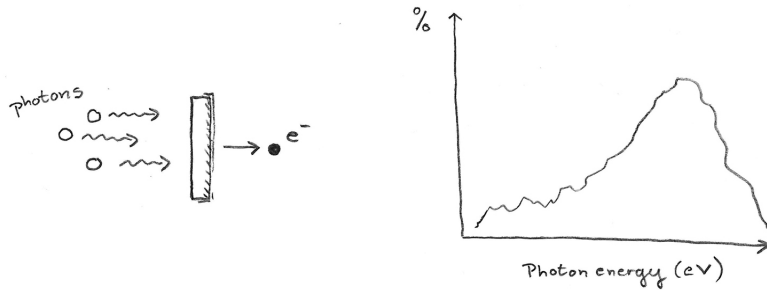


Figure 2-24: An example graph from a hypothetical device displaying quantum efficiency measurements per photon energy (right).

The companion to external quantum efficiency is internal quantum efficiency (IQE), which is a ratio between the number of electrons that are generated within the device to the number of photons that are absorbed by the device’s semiconducting materials. Internal quantum efficiency is defined as follows:

$$IQE(E_v) = \frac{\text{Electrons generated}}{\text{Photons absorbed } (E_v)}$$

Internal and external quantum efficiencies can be related by solving IQE for “electrons generated” and substituting into the equation for EQE as follows:

$$EQE(E_v) = IQE \times \frac{\text{Photons absorbed } (E_v)}{\text{Incident photons } (E_v)}$$

Quantum efficiency presents a picture of how well a device is absorbing different wavelengths of the electromagnetic spectrum which can then also be used to determine

how much solar energy a device will be able to utilize. A perfect device will theoretically be able to generate one electron free charge carrier per incident photon and for some materials, quantum efficiency can theoretically be as high as 100%. Experimental devices generate significantly less and 80% quantum efficiency is considered to be a more realistic bar for decent photovoltaic devices [6]. A spectrometer, chopper, and Xenon light source are used to take device quantum efficiency measurements. No external bias voltage is applied to the device while quantum efficiency measurements are taken to ensure that only electrons and holes generated by photocurrent are taken into account.

Chapter 3

Experimental techniques in device fabrication and characterization

This section aims to describe the particulars behind the design of the devices which will be discussed in the rest of this thesis including the mechanics behind device fabrication. We will begin an overview of the solar cell as a whole and continue with an analysis of each separate component starting with the two semiconducting layers of zinc oxide and lead sulfide and ending with the metal indium-tin-oxide electrodes. Sufficient explanation of the equipment responsible for device fabrication will be supplemented over the following pages with additional material provided in Appendix A for synthesizing lead sulfide quantum dots and Appendix B for spinning lead sulfide quantum dot films. We conclude the chapter with an overview of how to test devices for power and quantum efficiency as background material to better understand the experimental results in Chapter 4.

3.1 Quantum dot solar cell device design and overview

The following devices were based on a design by Professor Alexi Arango first explored in fabrication of solar cells with layers of small molecule N,N'-bis(3-methylphenyl)-N,N'-bis-(phenyl)-9,9-spiro-bifluorene (spiro-TPD) and colloidal cadmium selenide quantum dots [6]. The devices in this thesis have a novel design using lead sulfide

quantum dots as a photon absorbing layer and zinc oxide as a transparent electron transport layer mounted between a pair of metal indium-tin-oxide electrodes on a glass substrate. A diagram of the device in full showing all layers together in an overhead and cross-sectional view can be seen in Figure 3-1. The distinct characteristics of each layer, including design and function, will be a topic of discussion in the following sections. The devices in this thesis were fabricated by the author, Kanchi Gashaw, and Nathan Monroe using equipment from Professor Vladimir Bulović’s lab at the Massachusetts institute of Technology.

Each device consists of five separate layers, as seen in Figure 3-1. The active layer of the device consists of two semiconducting layers of lead sulfide and zinc oxide. Photons are absorbed by the layer of lead sulfide quantum dots which release negative free charge carriers into the semiconductor. The electrons travel into the zinc oxide layer and leave behind holes of positive charge in the lead sulfide quantum dots.

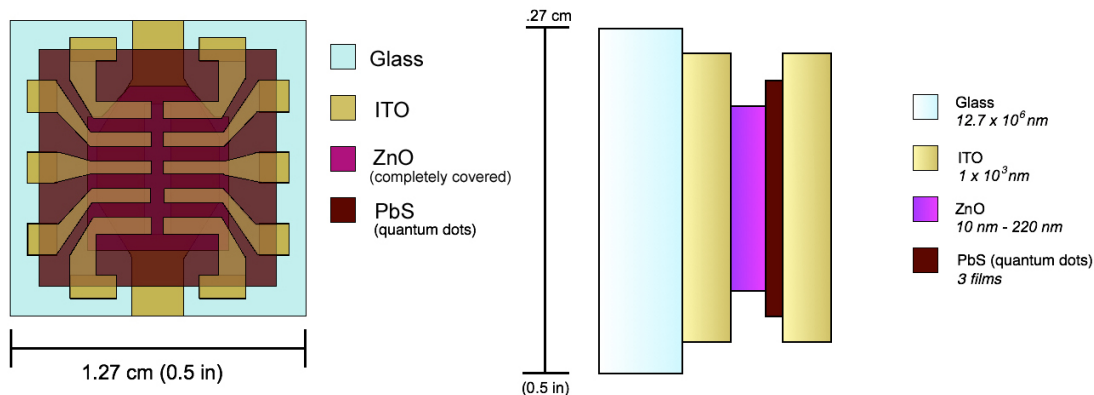


Figure 3-1: Cross section and overhead view of a device showing individual layers of material used in device design including glass substrate, indium tin oxide electrodes, lead sulfide quantum dot electron donor layer, and zinc oxide electron accepting layer.

The devices discussed in this thesis have a surface area of half-inch-by-half-inch and thickness ranging from about 2010 nm to 2220 nm, not including the 1 mm thick glass substrate as shown in Figure 3-1. In comparison, 1 millimeter is equal to 1 million nanometers. The total thickness of the ZnO layer varies from device to

device, as will be described further in Chapter 4.

The devices are fabricated, stored, and tested inside gloveboxes such as the one seen in Figure 4-1, where they are kept in controlled atmospheres of pure nitrogen. Nitrogen is an inert gas and unlike oxygen, which makes up approximately twenty percent of Earth's atmosphere, atoms of nitrogen will be nonreactive when they come into contact with atoms of other materials. Keeping the solar cells under nitrogen preserves the materials from corrosion. The effects of oxygen on device performance is the topic of one experiment on solar cell architecture discussed in this thesis and will be discussed in Chapter 4. In addition, the gloveboxes themselves are extensions of the clean room environment but with stricter standards of cleanliness than those employed on the clean room floor to prevent dust, dirt, and other foreign particulates from contaminating the device and harming photovoltaic performance.

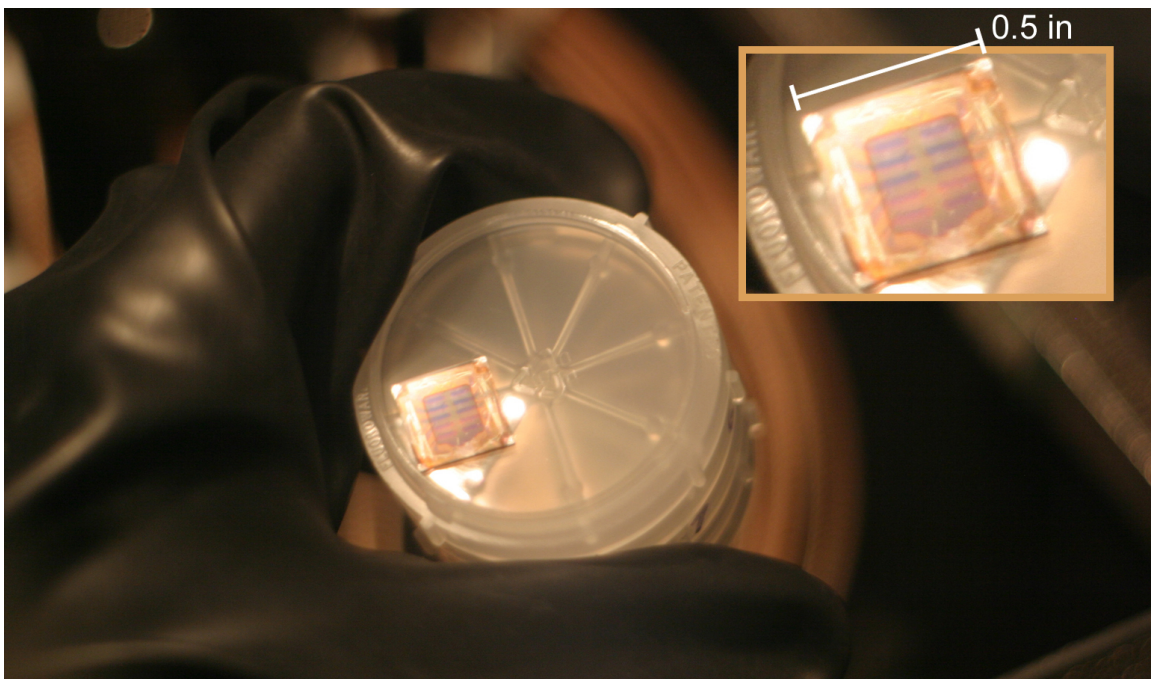


Figure 3-2: A completed device as seen resting in a circular fluoroware wafer container within a glovebox used for solar cell testing.

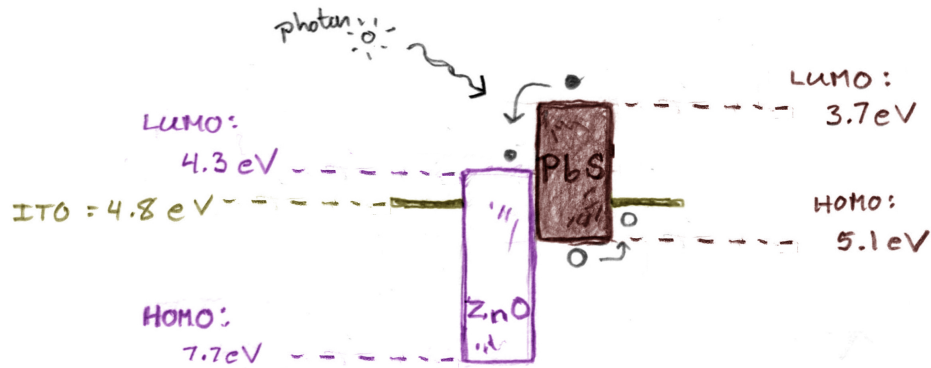


Figure 3-3: An energy level diagram of the solar cells fabricated in this thesis, showing the ZnO bandgap is $\sim 3.4\text{eV}$ [30], the PbS bandgap is $\sim 1.4\text{ eV}$ [28], and the work function for ITO is $\sim 4.8\text{ eV}$ [30].

3.1.1 Device band diagram

Figure 3-3 shows a bandgap diagram comparing the HOMO and LUMO levels of zinc oxide and lead sulfide. Exciton generation occurs in the photon-accepting lead sulfide quantum dot layer. Excitons are separated at the heterojunction between PbS and ZnO as electrons find the LUMO level of the ZnO more favorable than that of the PbS layer. Holes are unable to overcome the barrier set by the ZnO's HOMO level and are more inclined to stay within the PbS layer and collect on the attached ITO electrode. Electrons will tend toward the ITO electrode that is attached to the ZnO layer. The ITO metal-oxide electrodes have a work function of $\sim 4.8\text{ eV}$ [30].

3.2 Substrate and cleaning

We begin with a 1 mm (0.039 in) thick, 1.27 cm (0.5 in) wide, square glass substrate with a pre-printed set of indium-tin-oxide electrodes. The pattern of these electrodes can be seen on the left in Figure 3-10. The substrates are much like the glass seen in Figure 3-4 where the electrodes are transparent to allow light to pass through to the semiconducting layers which will be deposited on top. The substrates are cleaned in a sonicator using separate, five minute baths of micro-90, de-ionized water, acetone, and

isopropanol. Excess isopropanol is dried off using a nitrogen blower and substrates are then exposed to plasma for one minute. Substrates are then stored in isolated Fluoroware compartments and transferred into a nitrogen glovebox. The first layer is deposited either later the same day as cleaning or the following day to minimize the amount of particle buildup between the surface of the substrate and the first layer.

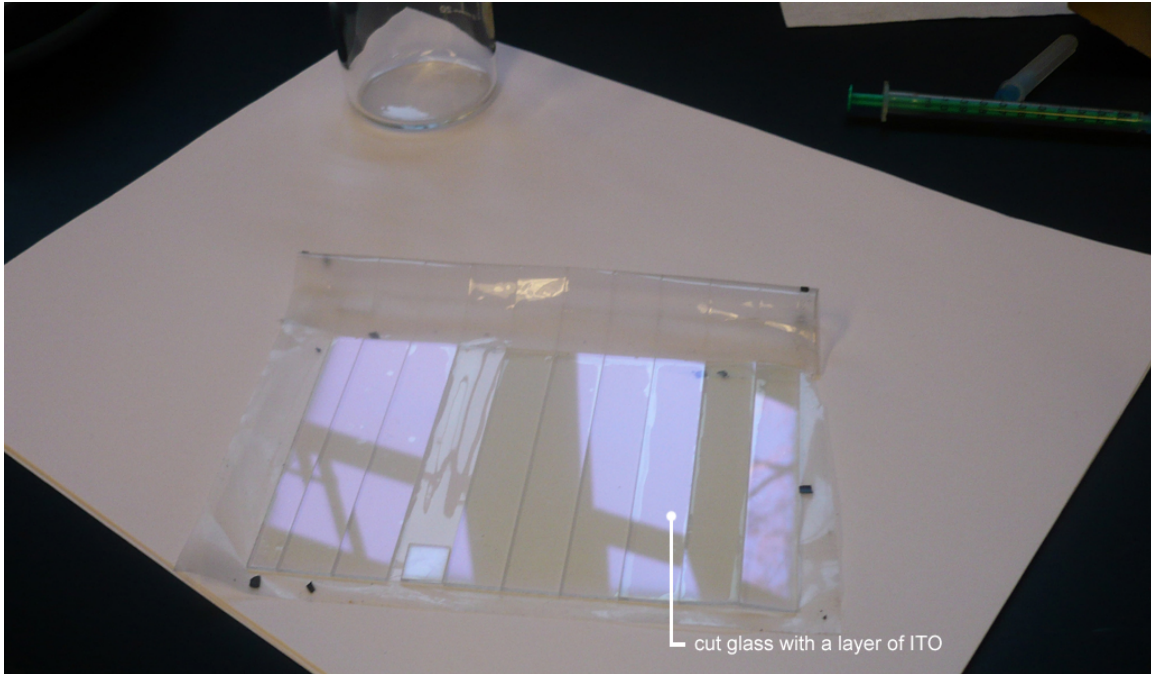


Figure 3-4: Uncut strips of 1 mm (0.039 in) thick glass with a layer of indium-tin-oxide printed on one side. The transparent ITO layer is tinted purple can be seen in the the window reflection as a purple-tint.

3.3 Zinc oxide transport layer

A layer of zinc oxide (ZnO) is used as the device's electron transport layer. This is also the first layer deposited onto the clean substrate with pre-printed ITO electrodes. We use a layer of zinc oxide (ZnO) in our devices. The ZnO is applied in a chamber using sputter deposition. A mask is used as a stencil, limiting the surface area of ZnO that covers the substrate, as seen in Figure 3-5.

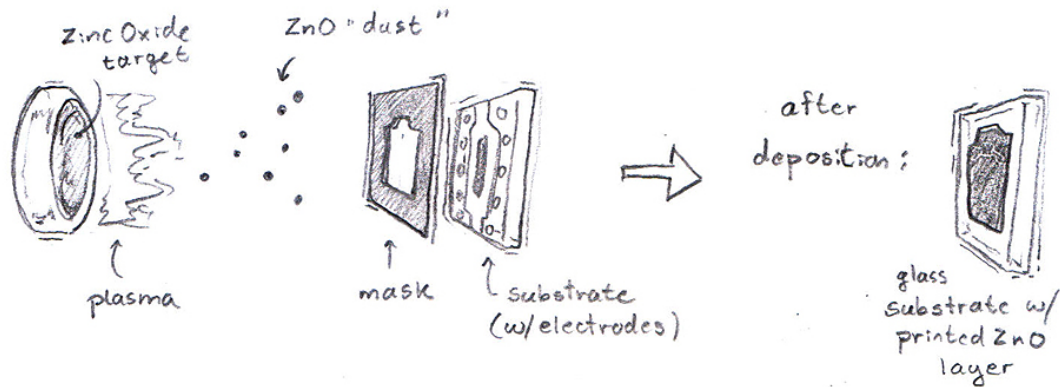


Figure 3-5: Sketch of zinc oxide deposition using mask inside sputter chamber (left) and final film after deposition (right).

A plasma is struck in a vacuum-sealed chamber filled with argon gas and loaded with a solid zinc oxide target. The plasma drives small particles of zinc oxide from the target so that the entire chamber becomes coated. If a substrate is placed inside with the back glass protected and the electrode-printed side facing the chamber, one side of the substrate will become coated as well. Use of a mask will control the pattern of zinc oxide deposited onto the substrate. The deposition process can last as long as needed to deposit zinc oxide layers of different thicknesses. An experiment addressing the optimal thickness of the zinc oxide layer is discussed in Chapter 4. Figure 3-6 shows a rough diagram of the inside of the sputter deposition chamber used to deposit the zinc oxide on the devices fabricated in this thesis. The z-stage rotates during the deposition to ensure an even deposition of material over all devices in the substrate holder. A hole in the side of the chamber, not shown in Figure 3-6, is connected to a vacuum transfer line which connects the sputter chamber, and other deposition chambers in the lab, to a nitrogen glovebox.

3.3.1 Design attributes of the ZnO layer

If the device is seen as a square from a bird's-eye view with top, right, bottom, and left sides, going counterclockwise, the design of the bottom electrodes make the left

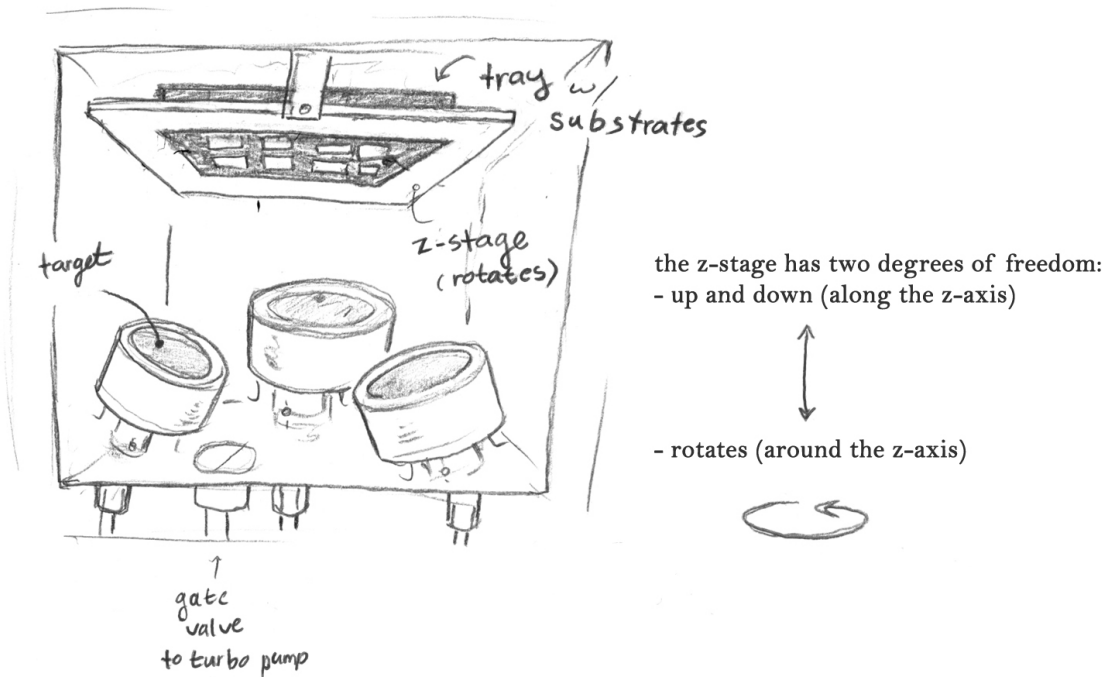


Figure 3-6: A sketch of inside of the sputter deposition chamber in the ONE Lab used to deposit the zinc-oxide on the devices fabricated in this thesis. The chamber consists of three deposition targets (bottom) and a z-stage used to hold the stencil-tray with glass substrates lying face down.

and right sides distinguishable from the top and bottom as can be seen on the left in figure 3-10. The tab at one end of the otherwise symmetrical zinc oxide square, as seen in Figure 3-7, is to distinguish the top side of the device from the bottom. The zinc oxide covers only the central strip of the bottom electrodes, as seen in Figure 3-7. In the completed device, this designate the only active region where charge is generated.

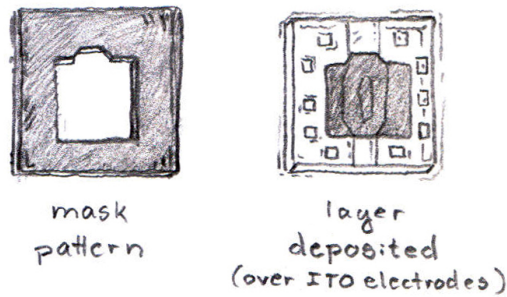


Figure 3-7: Completed layer of zinc oxide (right) seen with the mask which produced the design (left).

3.4 Lead sulfide quantum dots

The lead sulfide (PbS) quantum dots form the electron donor half of the solar cell and are also responsible for absorbing incident photons which strike the device. Lead sulfide absorbs primarily in the infrared portion of the electromagnetic spectrum which makes it an ideal material to explore in solar cell fabrication as the Sun emits energy mostly in the infrared as is discussed in Section 1.2. Lead sulfide quantum dots were synthesized for for these devices in Professor Mounji Bawendi's lab under the guidance of Darcy Wanger. A detailed description of PbS quantum dot synthesis is included in Appendix A.

3.4.1 Spinning thin films

After deposition of the zinc oxide layer, the device is coated with three films. A detailed description of the lead sulfide spin coating process is included in Appendix B. After a film of quantum dots is spun to cover the entire device, a border is scratched away as seen in Figure 3-8. The lead sulfide layer is delicate and the process can be done using metal or plastic tweezers. This will ensure that enough of the lead sulfide film is coating each pad to transfer charge, but also enable contact between the top electrodes and the ten, isolated ITO pads on the bottom electrodes as can be seen on the left and right side of the device also in Figure 3-8.

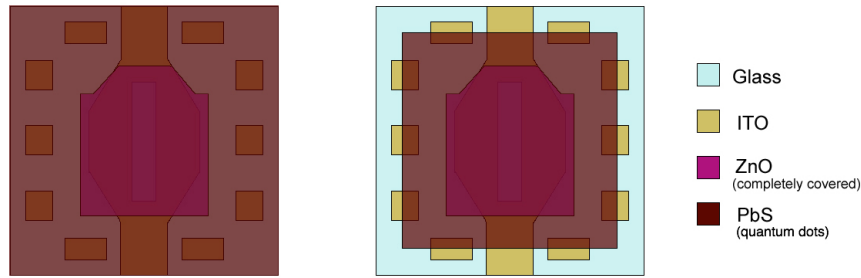


Figure 3-8: Sketches of solar cell shown right after spin coating films of PbS quantum dots (left) and after a border has been scratched off (right).

3.5 Final indium-tin-oxide electrodes

A final layer of indium-tin-oxide electrodes on top of the second transport layer completes the device as a solar cell ready for testing. The top ITO electrode layer is deposited using the same method as depositing the layer of zinc oxide. After the lead sulfide layer has been added to the device, the substrates are placed in a tray. A mask with a cut out in a shape to pattern the set of final electrodes is screwed in on top of the tray as seen in Figure 3-9. A similar tray with a different mask is also used to hold the substrates in the sputter deposition chamber when the zinc oxide layer is deposited. The mask patterns the top electrodes into a pattern shown on the right in Figure 3-10.



Figure 3-9: Metal tray used to load substrates into the metal oxide sputter deposition chamber, seen here with electrode stencil mask lying on top.

The top electrodes are 1000 nm thick. The delicacy of the lead sulfide layer requires a slightly different sputtering process. Deposition takes place in three stages where the first 200 nm are deposited under high gas pressure and low voltage to slow growth and minimize damage to the soft lead sulfide quantum dot film underneath. Growth speed is then increased for the next 200 nm and increased once again for the final 600 nm. The zinc oxide layer is deposited using the same growth rate from beginning to end.

3.6 Characterization and testing fixtures

After a device is fabricated it is stored face-down in its own separate fluoroware container with a concave floor to minimize contact between the container and the semiconducting layers on top. The container is kept under vacuum or inside a nitrogen atmosphere glovebox. Time spent between completion of the fabrication process and

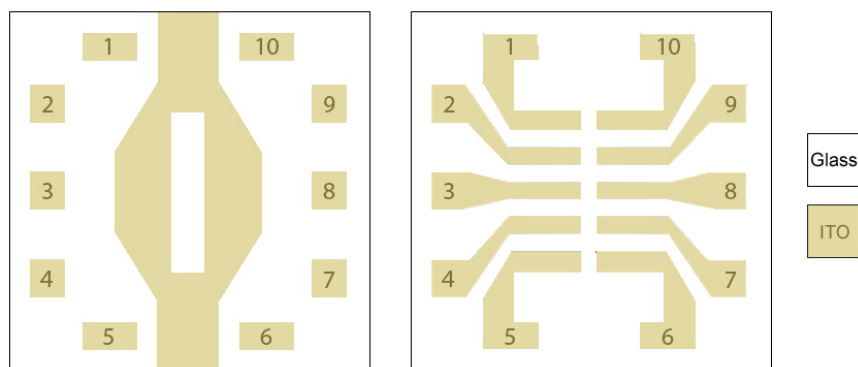


Figure 3-10: Diagrams of bottom (left) and top (right) transparent ITO electrodes of device sans the other layers.

testing is minimized to prevent decomposition of materials affecting experimental results. More about depletion of device efficiency over time is described in Section 4.1.1.

The electrical setup used to test the solar cells in this thesis, including the design of the probe fixture, was designed by Professor Alexi Arango and the following is described extensively in section 4.3 of his doctoral thesis [6]. The testing setup was developed to measure each electrode pad separately inside a glovebox. Each of the ten pads labeled in Figure 3-10 is thought of as a single solar cell. The active region in the center is where charge is generated in the zinc oxide and lead sulfide layers of the device. The top electrodes then distribute the charge to each of the ten electrode pads from a Keithley 6487 source-meter.

When a device is tested, it is placed face-down into the testing fixture shown in Figure 3-11. Each of the ten pads touches one of the probes in the testing fixture. Each probe is connected to a wire which can apply a forced voltage and relay current-voltage characteristics to a custom LabVIEW program which accumulates and processes the data.

The devices discussed in Chapter 4 were tested by sweeping four biases in the following order:

1. from 0 V to +6 V

2. from +6 V to 0 V
3. from 0 V to -6 V
4. from -6 V to 0 V

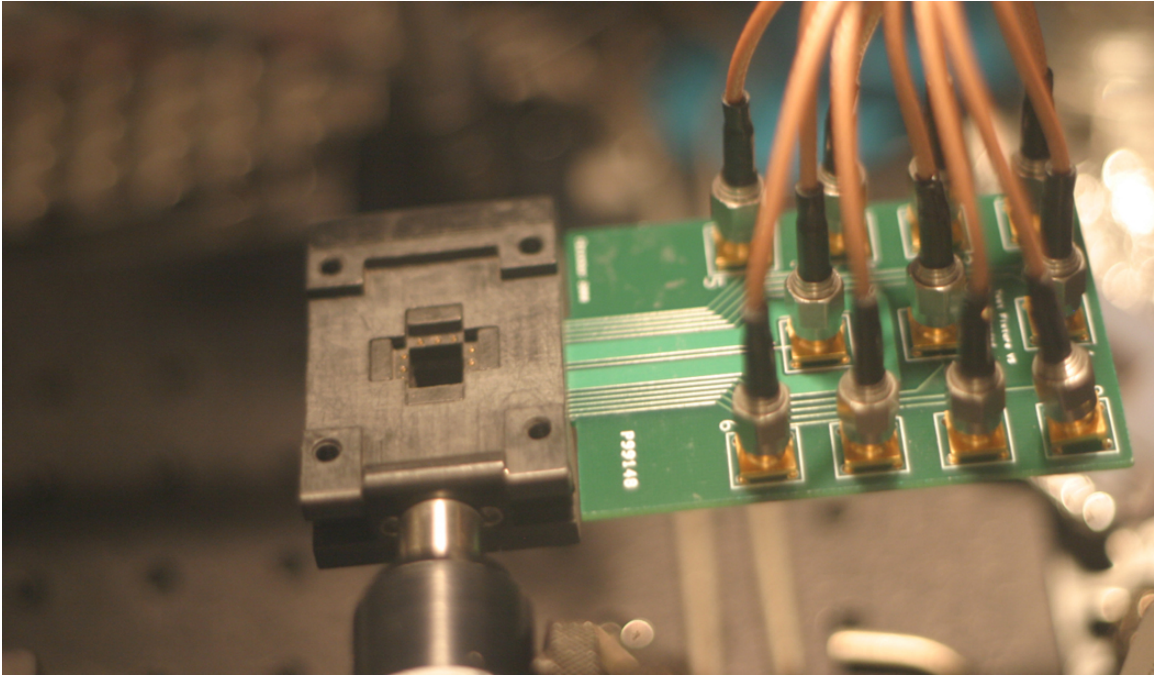


Figure 3-11: Testing fixture with probes. The completed solar cell is placed with glass side up and top electrode side down in the center with each of the metal probes touching one of the ten pads.

Chapter 4

Experimental results

This thesis aims to address solar cell device design issues and to inquire about the semiconductor properties of quantum dot and metal oxide materials. In this section, we will discuss the experiments performed to test colloidal quantum dot solar cells fabricated as described in Chapter 3. We obtained current-voltage curves for all devices and characterized the quantum efficiency of one promising set of devices. The basics behind solar cell testing is covered in Section 2.2.3 as a reference for the reader. Full scale figures of the current-voltage curves presented in this chapter are included in Appendix C.

As a note on record-taking, the author would like to inform the reader that the device names were generated based on the date of fabrication and number within the set fabricated on that day. For example, solar cell 1 from the set of device 20110214 would have been the first of the devices fabricated on February 14, 2011.

4.1 Affects of the open laboratory atmosphere on device efficiency after deposition of lead sulfide quantum dot films

A set of devices were fabricated to answer the question: Is exposure to air truly hazardous to the efficiency of zinc oxide and lead sulfide solar cell devices, espe-

cially during the fabrication process, or will some exposure to oxygen improve their efficiency?

4.1.1 Background Information

Earth's atmosphere is roughly 78% nitrogen, 20.9% oxygen, and 0.93% argon, with small quantities of other miscellaneous gases making up the rest. Nitrogen is an inert gas, chemically nonreactive. Oxygen, on the other hand, is highly reactive. As the second most abundant gas in our atmosphere, oxygen has an almost certain chance of coming into contact with commercial photovoltaics during the devices' lifespan.



Figure 4-1: A glovebox used for handling chemicals during the device fabrication process. Materials can be transferred inside the box using antechambers, such as the one with the red handle on the left, and users can access the inside of the box through the long, black rubber gloves.

The solar cells discussed in this thesis are fabricated, tested, and stored either in the lab's nitrogen atmosphere gloveboxes or under vacuum. Gloveboxes such as the one seen in Figure 4-1 contain an environment that is free of oxygen and moisture,

both of which may alter the properties of the materials that go into the devices. The glovebox is an ideal but imperfect environment with a small chance of oxygen molecules entering the chamber. Glovebox standards require an equipped O_2 monitor in addition to the ability to purge and recycle the atmosphere inside to restore it to an inert state. When items are transferred into a glovebox it is typical to evacuate and refill the antechamber three to five times with nitrogen while the items are inside. The process flushes foreign particulates, including O_2 molecules, from the surface of the items and minimizes contamination of the glovebox atmosphere from the outside environment. Although preferable to the open-lab environment, gloveboxes are imperfect and some degradation in device efficiency is observed after a long period of storage. Section 5.9, Figure 5-13, of Professor Alexi Arango's doctoral thesis shows how a device's current-voltage characteristics compare 4 days after the date of fabrication and 285 days after fabrication while stored in a nitrogen glovebox [6]. Devices are tested as soon as possible after fabrication to prevent degradation from affecting experimental results.

The device's lead sulfide (PbS) quantum dots are most at risk of being altered by exposure to oxygen. Lead sulfide can easily react with oxygen to form lead sulfates ($Pb_XS_XO_X$, where X represents the number of atoms of each element in the molecule). Lead sulfide is a semiconductor and has properties that are beneficial to producing voltage and current in a solar cell, but lead sulfates are insulators and their presence has the potential to truncate charge mobility in a device. Degradation in the lead sulfide layer will also affect the device's ability to absorb photons.

Precautionary measures are taken in the lab environment to preserve device quality. Researchers operate under the assumption that severe degradation can be detected after a device spends more than five minutes outside of the glovebox. Solar cells left outside of the nitrogen environment for one to two hours are assumed to not work at all. Device containers are wrapped in aluminum foil during transfers that take them outside the glovebox antechamber.

Device mobility outside of the glovebox also limits characterization to testing apparatuses that are contained in a glovebox close to or inside the same lab where

devices are fabricated. Glovebox size and expense limits the range of equipment that can be brought in for device characterization. An atomic force microscope (AFM) uses a laser and photodiode to detect the motion of a small cantilever as it probes the surface of a sample and can be used to collect information about the topography of a solar cell, but operation of an AFM while inside of a glovebox would be difficult. The AFM's precision makes it sensitive to even minor vibrations and perturbations in its immediate environment and the user would be required to operate the microscope's delicate equipment while wearing a pair of bulky gloves. The user's observations are also limited by the pane of glass on the front of the glovebox that distances the user from the materials inside.

The known nature of device sensitivity to oxygen raised the question of how long a device has to be exposed to the Earth's atmosphere before a significant change is seen in device performance.

4.1.2 Experiment procedure and methods

A series of six devices were fabricated on substrates that were cleaned on June 28th, 2010 and each labeled as part of a set of Devices 20100628. The initial layer of zinc oxide for all devices was deposited on the same day. On June 29th, three films of lead sulfide quantum dots were spun on top of each device. On June 30th, all devices except for one control were taken out of the glovebox environment for varying amounts of time documented in Table 4.2. Devices were taken out of their individual fluroware containers and placed on top of a Texwipe cloth with the lead sulfide layer face up for the duration of their exposure.

The lead sulfide border, described in Section 3.4.1, was scratched away on devices 1, 2, and 3 while the devices were inside of a glovebox and the border on devices 4, 5, and 6 was scratched while the devices were spending greater lengths of time outside of the glovebox. The discrepancy was not done intentionally, but it should have no affect on the experimental results.

The fabrication was completed on June 30th, 2010. Devices 20100628 were tested the day after on July 1st.

Table 4.1: Devices 20100628 produced to test air annealing of lead sulfide quantum dot hole-transporting layer.

Device #	Materials	Time Outside
1	ITO/ZnO/PbS	none (control)
2	ITO/ZnO/PbS	5 min
3	ITO/ZnO/PbS	15 min
4	ITO/ZnO/PbS	30 min
5	ITO/ZnO/PbS	60 min
6	ITO/ZnO/PbS	120 min

4.1.3 Results

Current-Voltage Curves

Figure 4-2, Figure 4-3, and Figure 4-4 compare the performances of each device to the control device's red current-voltage curve and the last plot in Figure 4-4 shows the collected current-voltage curves for all devices in the experiment. There is a significant decrease in short-circuit current and an increase in open-circuit voltage as time spent exposed to the lab atmosphere increases. Overall, devices are shown to produce both less dark current and less light current as more time is spent outside of the glovebox. Fill factor increases over time from 31.5% for the control device to 38.5% for the device that spent two hours outside of the glovebox.

Table 4.2: Chart of the short-circuit current (J_{sc}), open-circuit voltage (V_{oc}), and fill factor (FF) for each device in set 20100628.

Device #	Time Outside	J_{sc} (mA/cm ²)	V_{oc} (V)	FF
1	none (control)	6.7599	0.389	31.54%
2	5 min	6.0396	0.409	35.59%
3	15 min	6.1843	0.411	35.59%
4	30 min	5.5951	0.420	37.41%
5	60 min	4.8770	0.436	34.94%
6	120 min	5.1034	0.442	38.49%

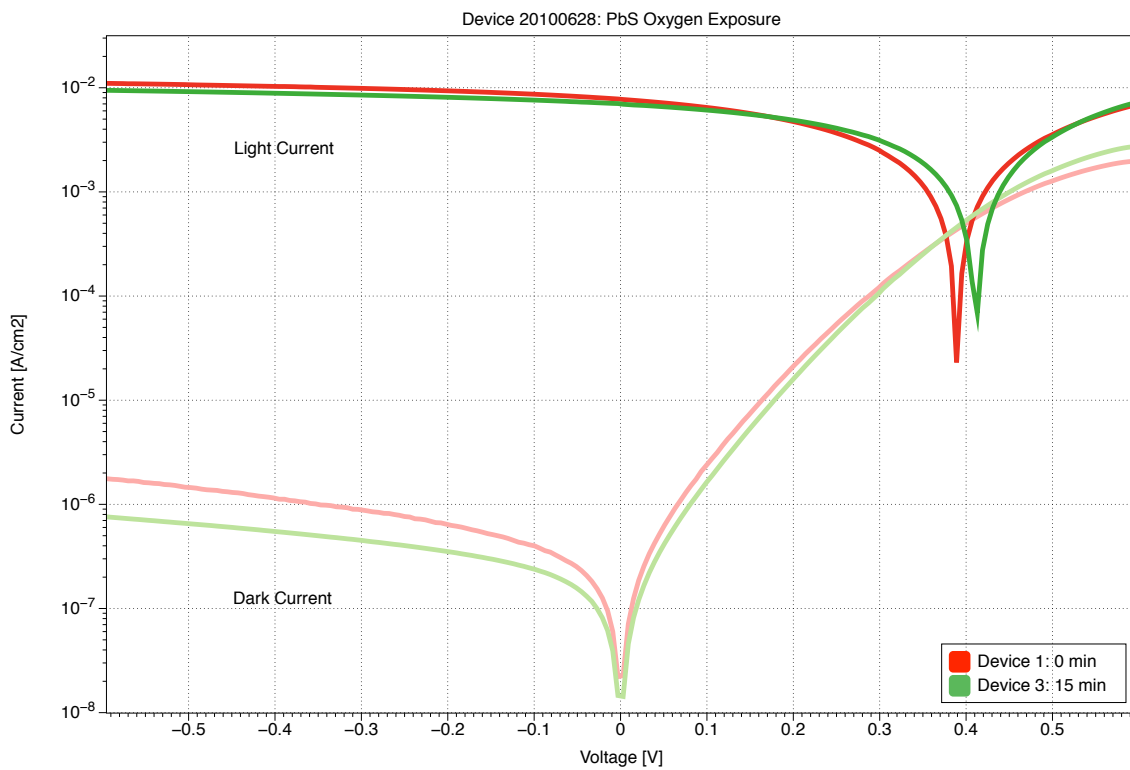
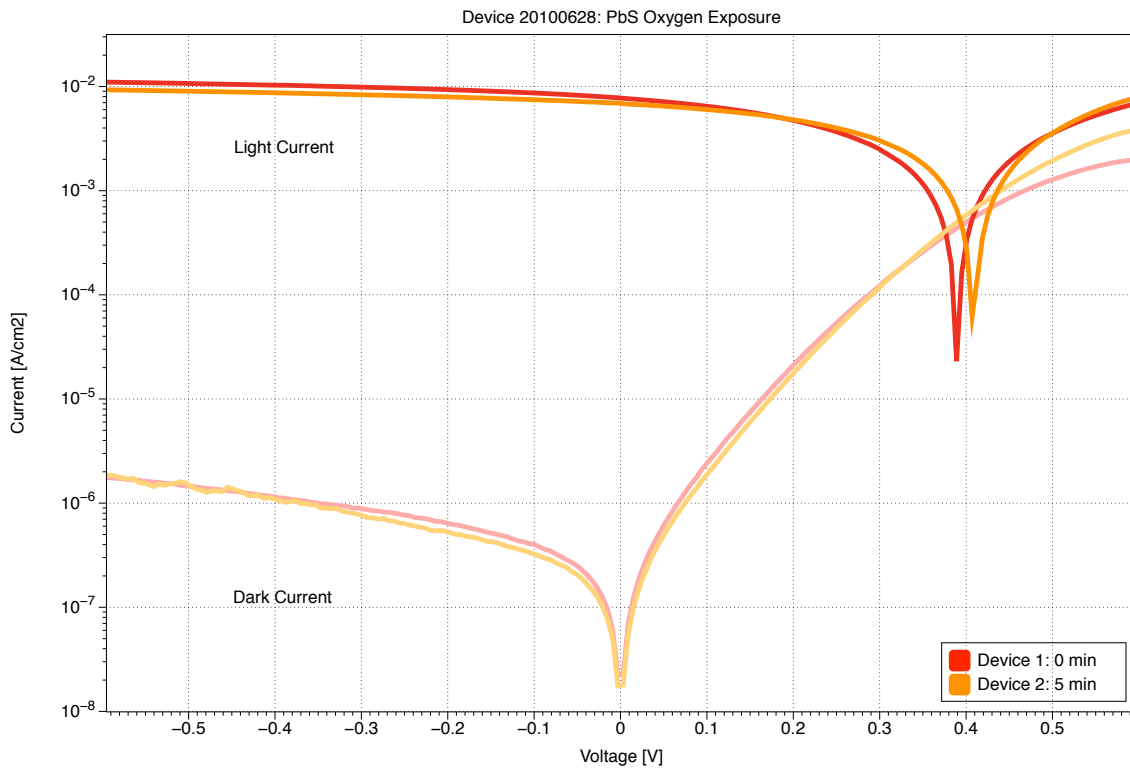


Figure 4-2: Current-voltage curves showing how performance varies between ZnO and PbS solar cells that have spent 0 and 5 minutes (top) and 0 and 15 minutes (bottom) outside of an inert glovebox atmosphere.

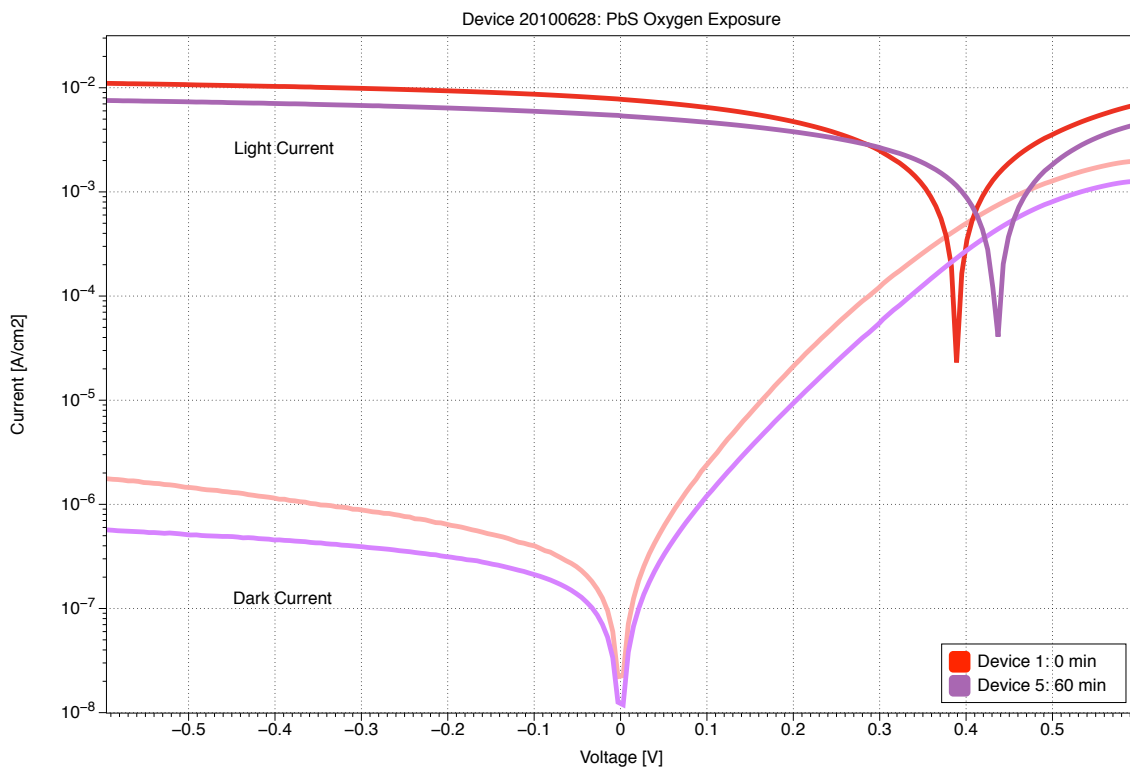
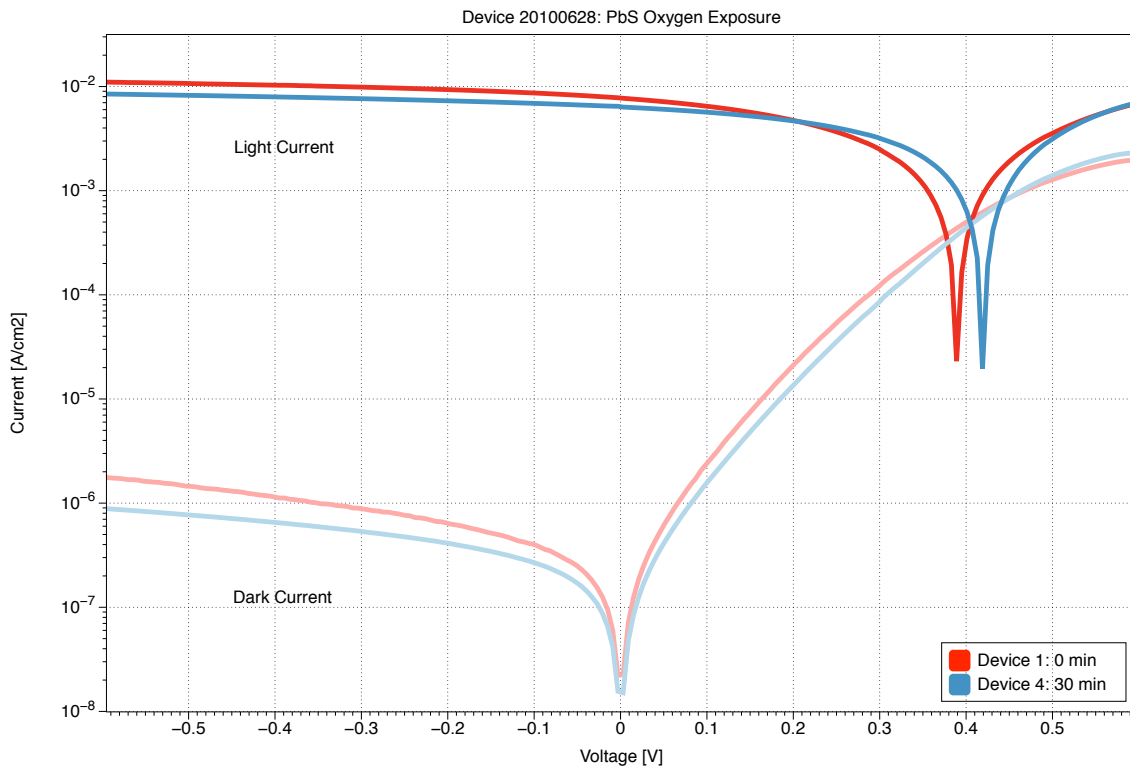


Figure 4-3: Current-voltage curves comparing how performance varies between ZnO and PbS solar cells that have spent 0 and 30 minutes (top) and 0 minutes and 1 hour (bottom) outside of an inert glovebox atmosphere.

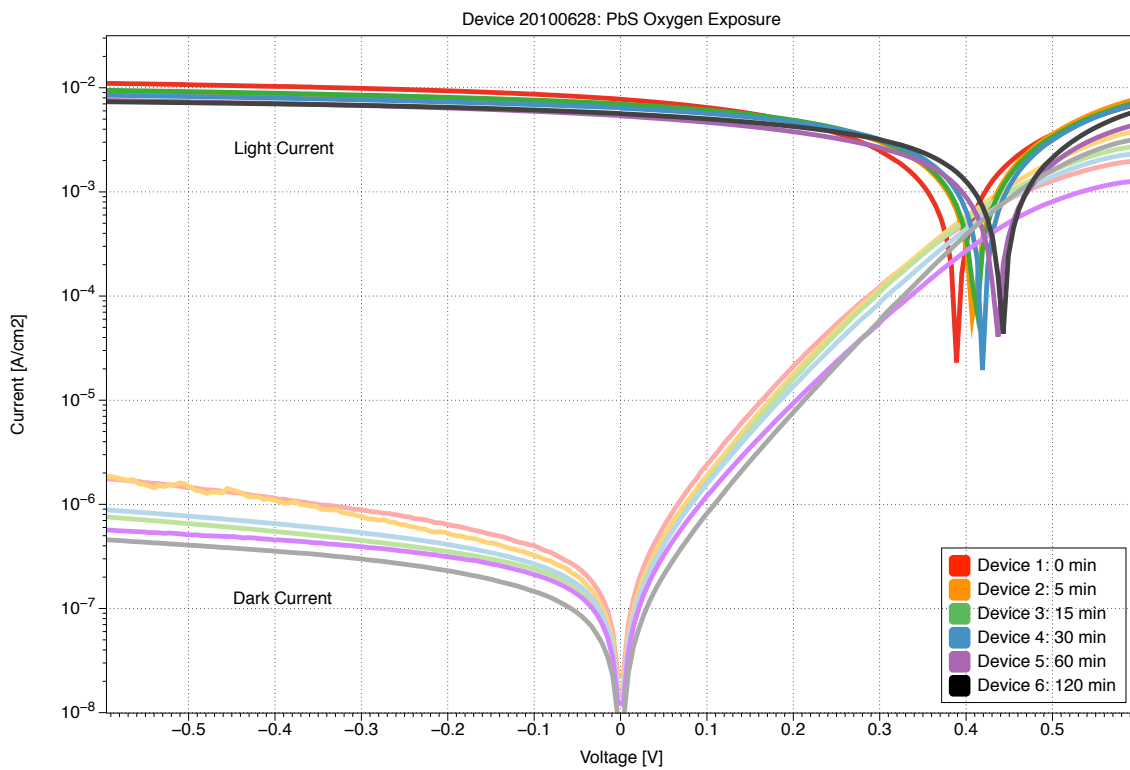
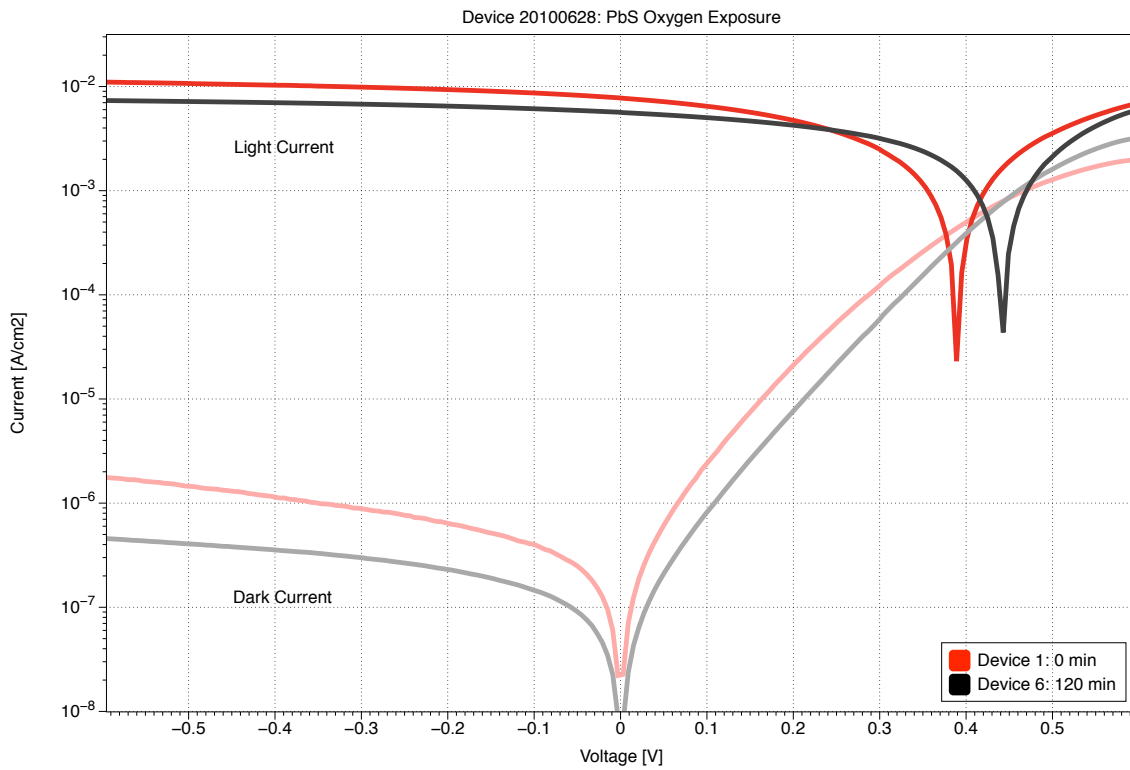


Figure 4-4: Current-voltage curves showing how performance varies between ZnO and PbS solar cells that have spent 0 minutes and two hours outside of an inert glovebox atmosphere (top) and collected current-voltage curves for all solar cells from Figure 4-2, Figure 4-3, and Figure 4-4 (bottom).⁸⁶

Quantum Efficiency Curves

Quantum efficiency measurements were taken to determine how the lead sulfide layer was affected. Figure 4-5 shows the quantum efficiency measurements produced by the devices as time spent outside the glovebox increases. The solar cell absorbs photons of energy between 1.1 eV and 4.2 eV. There is a significant decrease in quantum efficiency as time spent outside of the glovebox atmosphere increases. The highest quantum efficiency measured was Device 2, reaching about 73% quantum efficiency at 3.1 eV, which is equivalent to 400 nm or violet light.

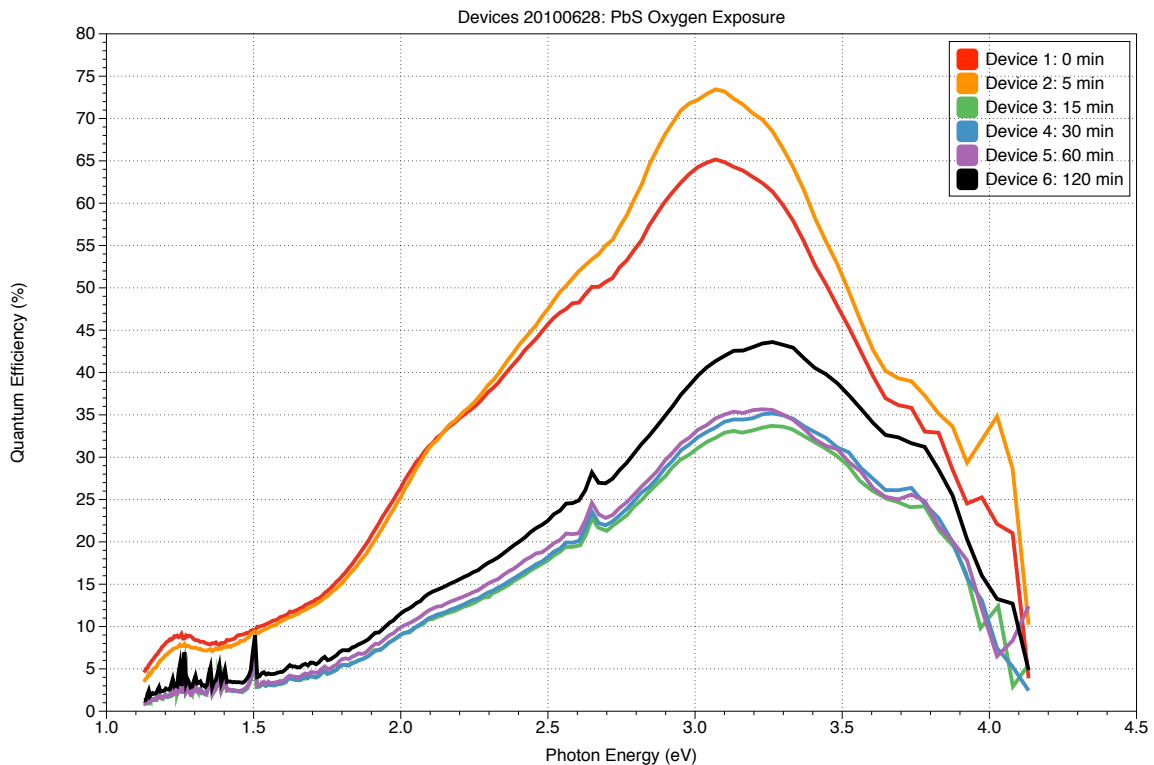


Figure 4-5: Collected quantum efficiency curves for devices 20100628 showing how photon energy absorption varies between devices that have spent varying amounts of time outside of an inert glovebox atmosphere.

The device that spent fifteen minutes outside of the glovebox has the lowest quantum efficiency curve with a drop to 26% quantum efficiency at 3.1 eV. After fifteen minutes, the quantum efficiency curves increase with each successive length of time

showing significantly improved quantum efficiency after two hours of exposure. Devices that spent thirty minutes to one hour outside of the glovebox have on average 35% quantum efficiency at 3.1 eV whereas the device that spent two hours outside of the glovebox reached 43% quantum efficiency at 3.1 eV.

The orange quantum efficiency curve for device 2 and the black quantum efficiency curve for device 6 stand apart from the general trend, implying that there are two devices that showed improvement in quantum efficiency with more exposure to the lab atmosphere. It should be taken into account that quantum efficiency measurements are more difficult to collect than current-voltage curves and some experience is required to collect good data. The quantum efficiency curves in Figure 4-5 resulted from the first QE measurements taken collectively by the author, Kanchi Gashaw, and Nathan Monroe after being trained to use the spectrometer, so device 2 and device 6 are most likely a discrepancy caused by user error.

Short-Circuit Current Density Plot

Figure 4-6 shows the averaging of light current for each device biased at 0 V. This is a concise summary of how the devices in the set performed overall and shows variation of current collected in testing. Devices that performed the best spent the least amount of time outside the glovebox environment.

A significant decrease in current happened when devices spent thirty minutes to one hour outside the glovebox. The decrease in short-circuit current was not as dramatic as first predicted. The device that spent two hours out of the glovebox performed almost as well as the device that only spent five minutes outside of the glovebox.

4.1.4 Analysis

The current-voltage curves in 4-2, Figure 4-3, and Figure 4-4 and the short-circuit current density plot in Figure 4-6 show degradation in solar cell performance as time spent outside of the glovebox's protective environment increases. However, overall

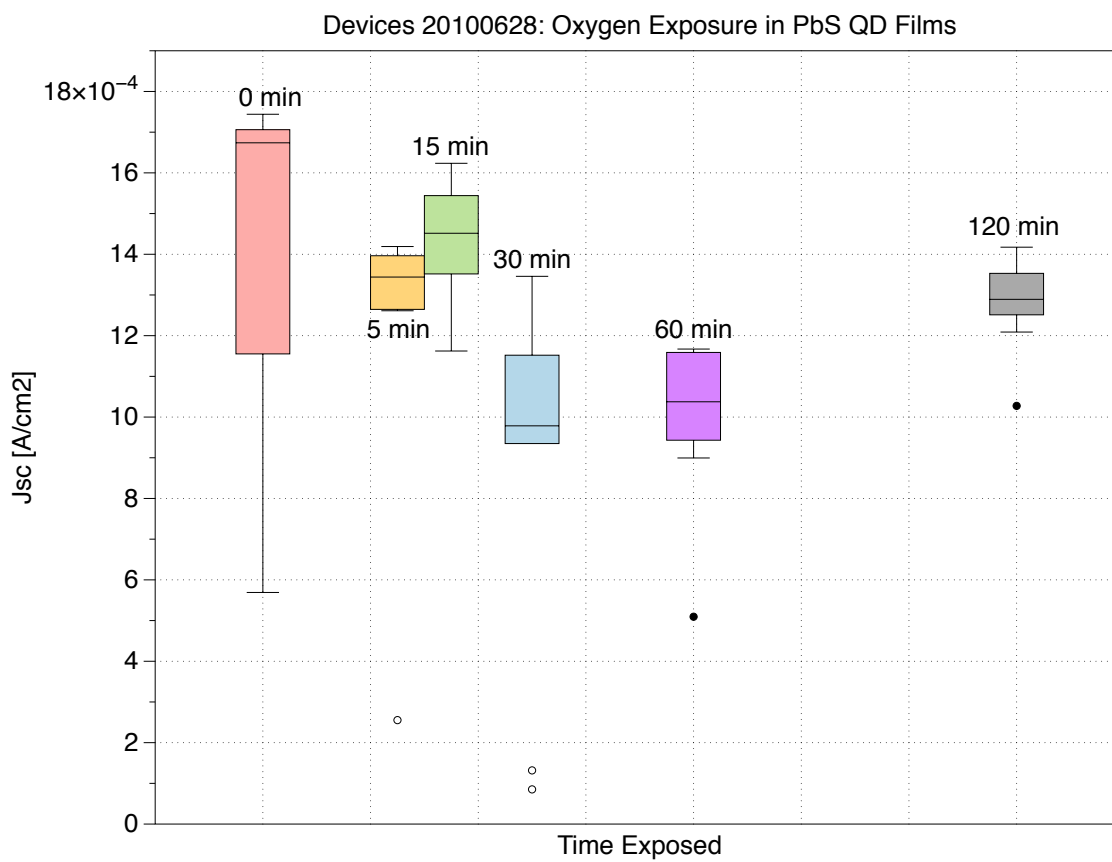


Figure 4-6: Collected short-circuit current density for devices 20100628 taken at a bias of 0 volts.

device performance far exceeds what was initially expected. It is surprising that a device which spent two hours outside of the glovebox is able to generate any short-circuit current at all. The current-voltage curves in the second plot of Figure 4-4 are impressive as they show oxygen exposure has limited effects on device power efficiency. Having consistent forward bias dark current from device to device, as seen in the second plot of Figure 4-4, is also promising as it shows consistency during device fabrication.

Most interesting is how open-circuit voltage (V_{OC}) increases over time. The inverse relationship between current decrease and voltage increase is initially perplexing. The significant change in quantum efficiency, as seen in Figure 4-5 over time, shows that oxygen most affects the lead sulfide quantum dot layer in the device. This layer absorbs energy from incident photons and releases free charge carriers within the solar cell that are transported to the device's zinc oxide layer. However, recombination may occur if negative charge within the zinc oxide layer comes close enough to feel a coulombic attraction to a hole in the lead sulfide layer as shown in Figure 4-7. This leads to a decrease in open-circuit voltage across the solar cell.

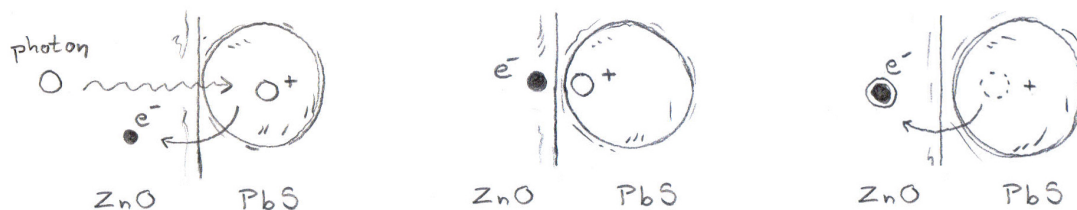


Figure 4-7: Sketch of electron-hole separation and recombination after excitation from an incident photon. Hole mobility within the lead sulfide causes recombination at the zinc oxide and lead sulfide barrier.

This thesis proposes the following mechanism to explain the observed device behavior. When oxygen comes into contact with a quantum dot of lead sulfide it will combine with the lead and sulfide atoms on the perimeter to form a less conductive lead sulfate shell around the dot. Electrons have more energy after photo-excitation than holes. The added energy transferred from the incident photon gives electrons

more energy for charge transfer across an interface such as the device's zinc oxide and lead sulfide interface. Holes are not imparted with excess energy and would be more sensitive to a barrier of less conductive material. Holes would be less likely to overcome a barrier of lead sulfate than an electron as seen in Figure 4-8. Open-circuit voltage is increasing over time as more oxidized lead sulfide quantum dots are able to build up more charge and produce a greater voltage. Lower conductivity in the solar cell translates to less current as it becomes harder for charge to tunnel through the shell of one dot and into the shell of another.

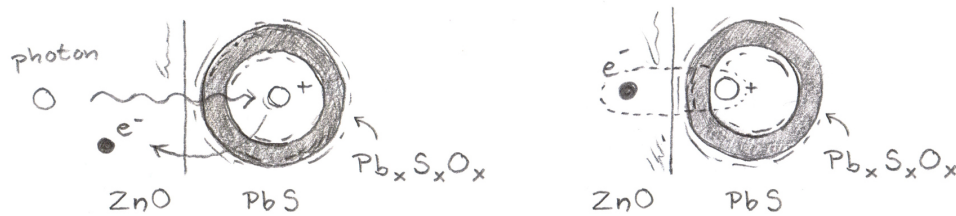


Figure 4-8: Sketch of electron-hole separation after excitation from an incident photon where the electron is able to overcome the lead sulfate barrier but hole mobility is limited and it is unable to recombine with the electron in the zinc oxide layer.

4.2 Variations in zinc oxide thickness and effects of oven annealing on device efficiency

The zinc oxide layer is the focus of the next experiment. Once we had determined that solar cells utilizing zinc oxide, lead sulfide, and ITO could work together as a potential photovoltaic device, we sought to optimize the characteristics of each layer for maximum power efficiency. The zinc oxide electron-transporting layer is the device's electron transport layer, as was discussed in Section 3.3. The zinc oxide layer must be thick enough to prevent the passage of holes from the lead sulfide layer to the electrode, but the layer must also be thin enough so that negative charge can in fact travel across the entire length of the semiconductor and reach the adjacent electrode. Figure 4-9 shows two different devices each with zinc oxide of different thicknesses.

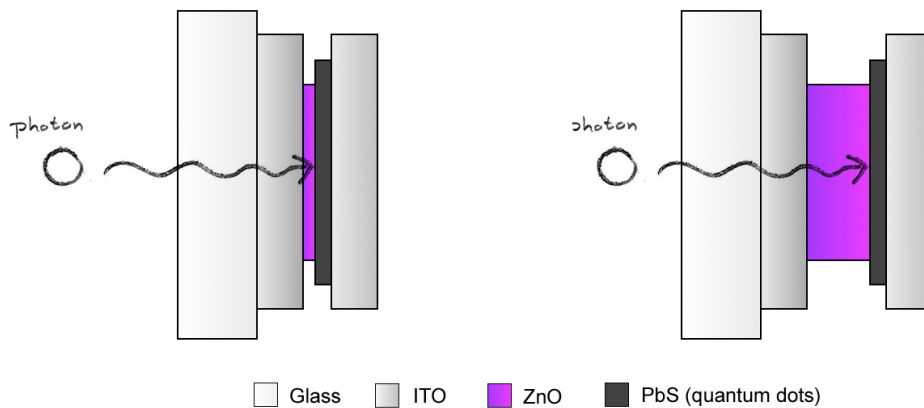


Figure 4-9: Two colloidal quantum dot photovoltaics showing variations in zinc oxide thickness.

An additional experiment was planned subsequently to test the affects of annealing on the zinc oxide layer. An incomplete device is baked in an oven before the addition of lead sulfide quantum dots and the heat removes oxygen atoms from the zinc oxide layer. This process is a type of doping. Doping adjusts the properties of a semiconductor to change the percentage of electrons that are in either the material's valence band or conduction band. Removing oxygen from zinc oxide adds more electrons to the material's conduction band, freeing more negative charge carriers. This

should theoretically increase the amount of current produced by the device.

4.2.1 Experiment procedure and methods

Eight substrates were cleaned on July 6th, 2010 and labeled each as part of the set of devices 20100706. Sputtering ZnO took place on July 7th and July 8th. The devices were then annealed on July 8th before the PbS layer was deposited. The annealing process took place at 450 degrees Celsius at RAM of 10 degrees per minute. The devices were removed from the oven when the chamber had cooled down to 200 degrees and devices were transferred to glovebox antechamber in less than one minute. Three layers of PbS quantum dots were spun onto each device and the final layer of ITO electrodes were deposited on the same day as the annealing after the annealing process took place. Devices were then transferred to the testing glovebox and tested on July 9th, 2010.

Table 4.3: Devices 20100706 produced to test optimal thickness of zinc oxide electron acceptor semiconducting layer.

Device #	Materials	ZnO Layer Thickness
1	ITO/ZnO/PbS/ITO	10 nm
3	ITO/ZnO/PbS/ITO	80 nm
5	ITO/ZnO/PbS/ITO	150 nm
7	ITO/ZnO/PbS/ITO	220 nm
2	ITO/ZnO/Annealing/PbS/ITO	10 nm
4	ITO/ZnO/Annealing/PbS/ITO	80 nm
6	ITO/ZnO/Annealing/PbS/ITO	150 nm
8	ITO/ZnO/Annealing/PbS/ITO	220 nm

4.2.2 Results

Current-Voltage Curves

Current-voltage curves were compiled in Figure 4-10 for solar cells 1, 3, 5, and 7 out of the set of devices 20100706 to examine the effects of varying zinc oxide thickness on device performance. The curves show that open-circuit voltage increases as device

thickness increases from 10 nm to 80 nm. However, open-circuit voltage for the two devices with ZnO thicknesses of 150 nm and 220 nm are significantly worse. Almost no open-circuit voltage can be detected for the device with the second thickest layer of ZnO, solar cell 5 with ZnO thickness of 150 nm, as can be seen in Figure 4-10 by the purple light current curve with symmetry around 0 V. Open-circuit voltage for the device with the thickest layer of zinc oxide, solar cell 7 with ZnO thickness of 220 nm, also 0 V. Solar cell 7 performs so poorly that its behavior while biased both under illumination and while in the dark is the same. The black light current curve for solar cell 7 in Figure 4-10 looks similar to solar cell 7's light gray dark current curve. Virtually no additional photocurrent can be detected in the thickest device. The dark current curves for solar cells 5 and 7 show less asymmetry than the dark current curves for solar cells 1 and 3.

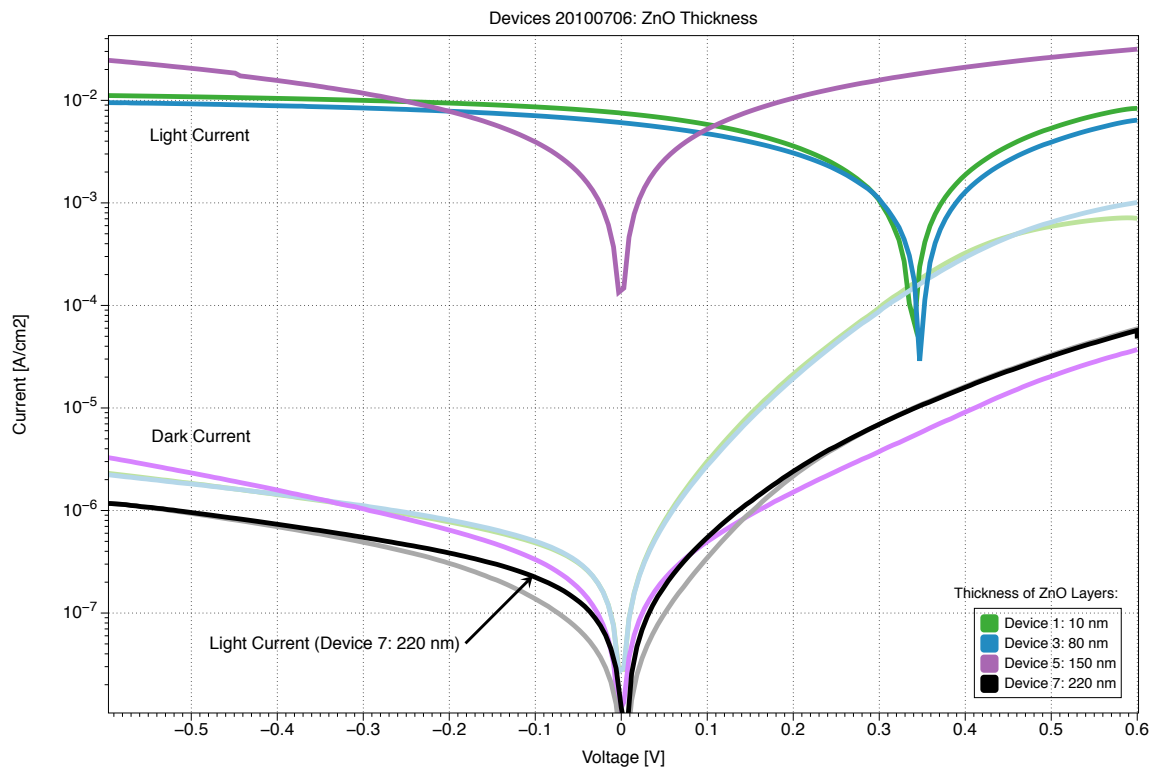


Figure 4-10: Collected current-voltage curves for solar cells 1, 3, 5, and 7 out of the set of devices 20100706. Each was fabricated with ZnO layers of different thicknesses ranging from 10 nm to 220 nm.

Table 4.4: Devices 20100706 produced to test optimal thickness of zinc oxide electron acceptor semiconducting layer.

Device #	ZnO Thickness	Jsc (mA/cm ²)	Voc (V)	FF
1	10 nm	6.2440	0.338	28.80%
3	80 nm	5.0803	0.348	29.26%
5	150 nm	7.2262×10^{-3}	-0.140×10^{-3}	-41.77%
7	220 nm	-1.4919×10^{-5}	-4.040×10^{-3}	0.00%

Additional current-voltage curves shown in Figure 4-11 were compiled for solar cells 2, 4, 6, and 8 to examine how annealing the zinc oxide layer would affect the performances of devices with varying ZnO thicknesses identical to those tested with solar cells 1, 3, 5, and 7. The device with the thinnest layer of annealed zinc oxide, solar cell 2 with a ZnO layer 10 nm thick, performed the worst with an open-circuit voltage of almost 0 V, as can be seen by the red light current curve symmetrical at an axis of 0 V. The device with the thickest layer of annealed zinc oxide, solar cell 8 with a ZnO layer 220 nm thick, shows an improved V_{OC} of about 0.242 V. Strange artifacts are seen around where the V_{OC} point is. The jagged 220 nm curve can also be seen in the 150 nm light current curve.

Current produced while solar cells 2, 4, 6 and 8 are biased in the dark is overall quite high. Many of the reddish dark current curves in Figure 4-11 overlap with the purple light current curves. The dark current curves also lack the usual asymmetry typical of a dark current curve produced by a good device.

Table 4.5: Devices 20100706 produced to test optimal thickness of zinc oxide electron acceptor semiconducting layer. * = the device was annealed after ZnO layer was deposited.

Device #	ZnO Thickness	Jsc (mA/cm ²)	Voc (V)	FF
2*	10 nm	-2.463×10^{-2}	-5.817×10^{-4}	-888.97%
4*	80 nm	5.1876	0.327	26.71%
6*	150 nm	1.1118	0.067	24.736%
8*	220 nm	4.1472	0.242	25.24%

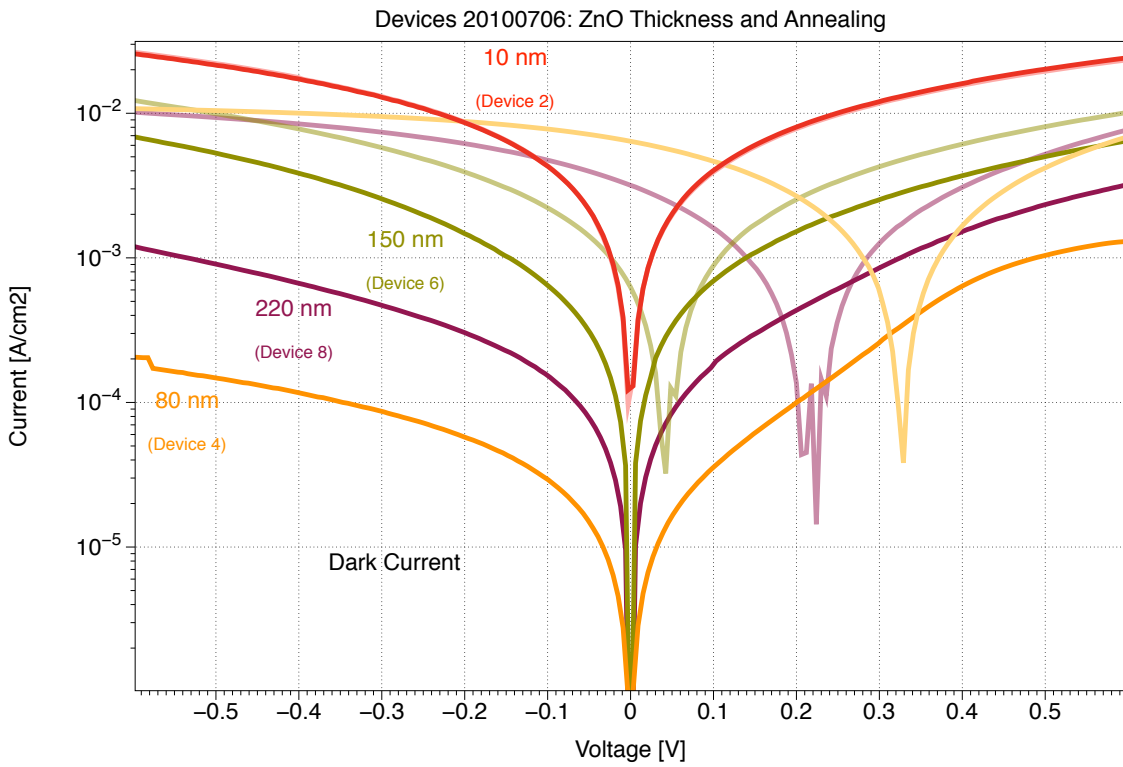
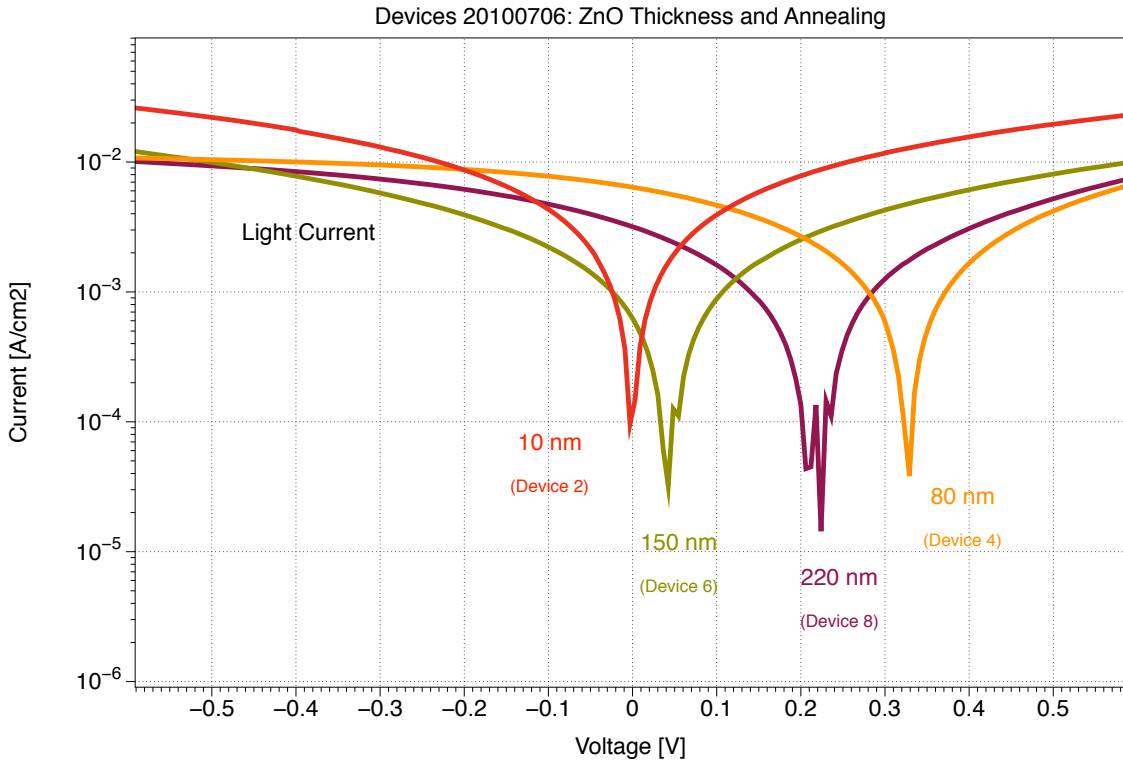


Figure 4-11: Collected current-voltage curves for solar cells 2, 4, 6, and 8 out of the set of devices 20100706. Each was fabricated with ZnO layers of different thicknesses ranging from 10 nm to 220 nm that were annealed in an oven before the PbS layer was spun on top.

Figure 4-12 is a compilation of the light current curves from Figure 4-10 and Figure 4-11 to compare the performances in the light of devices with layers of annealed zinc oxide to devices with layers of unannealed zinc oxide. The amount of current produced by devices with annealed layers of zinc oxide is overall much higher than the current produced by devices with unannealed layers of zinc oxide. However, the open circuit voltage for the devices with annealed layers of ZnO is significantly less than it is for the devices with unannealed layers of ZnO. Asymmetry in the dark current curves is most prominent in the devices with the thinnest, unannealed layers of ZnO, solar cells 1 and 3.

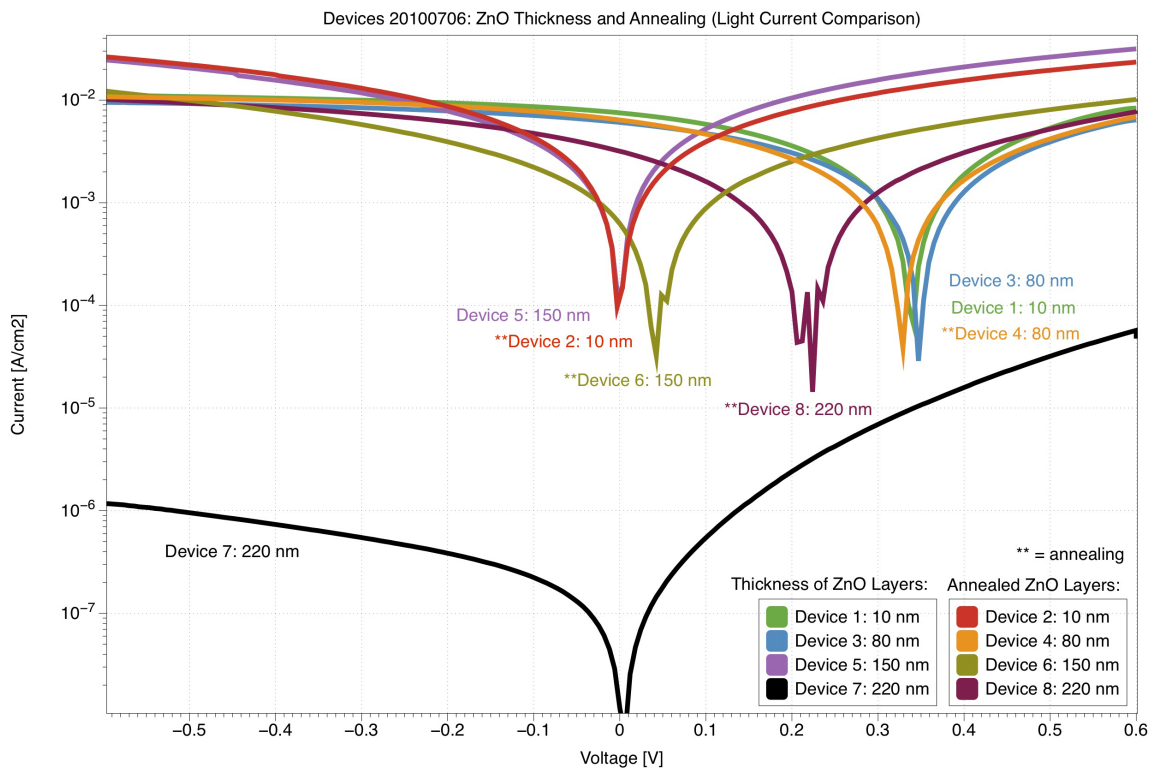


Figure 4-12: Collected current-voltage curves for all solar cells in the set of devices 20100706. Each was fabricated with ZnO layers of different thicknesses ranging from 10 nm to 220 nm and devices 2, 4, 6, and 8 were annealed in an oven before the PbS layer was spun on top.

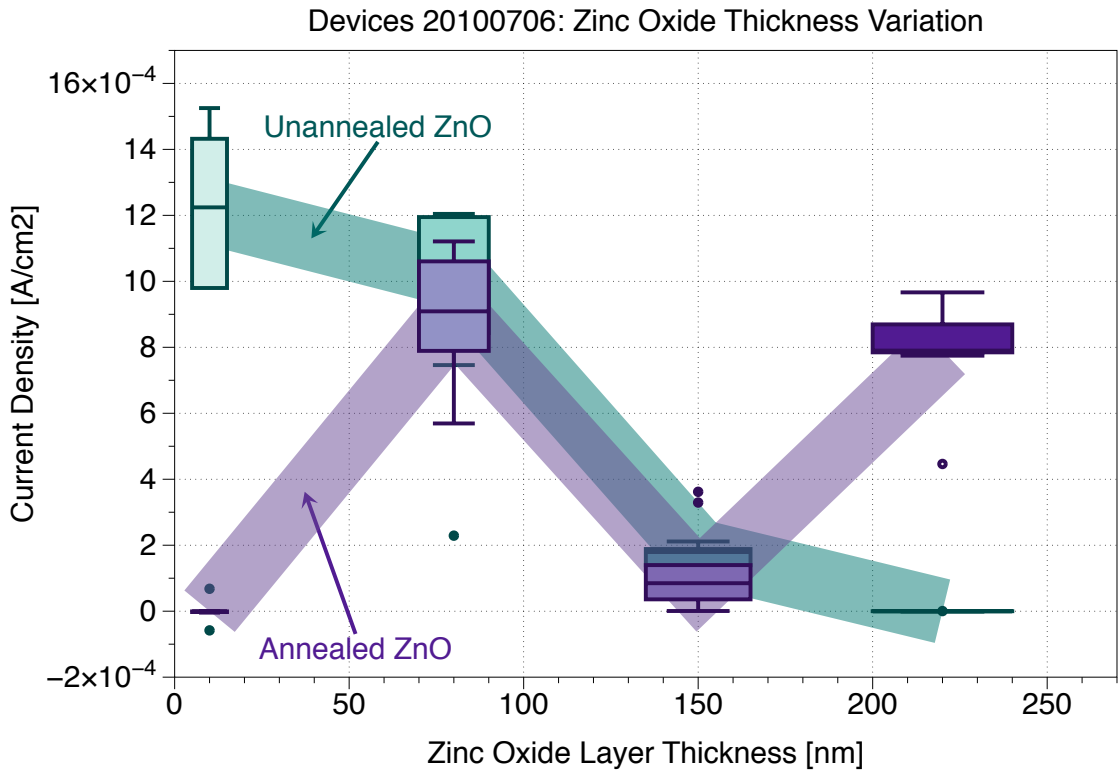
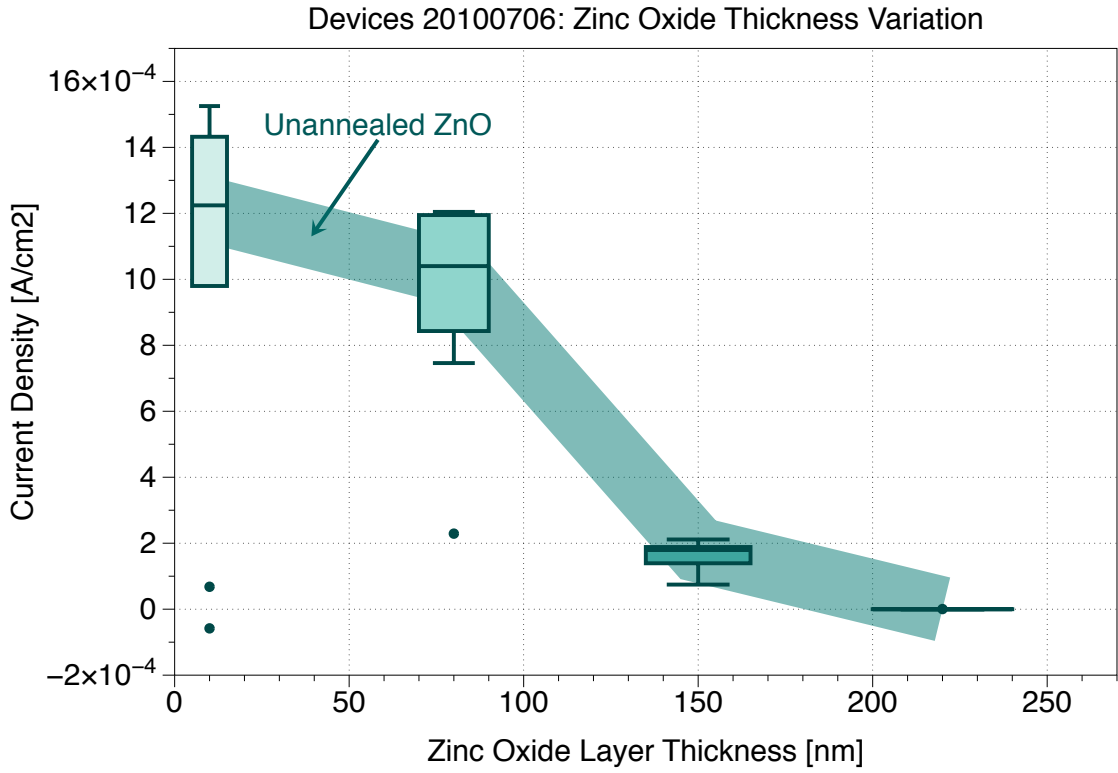


Figure 4-13: Collected short-circuit current density for devices 20100706 with unannealed ZnO layers (teal) and annealed ZnO layers (purple).

Short-Circuit Current Density Plot

The short circuit-current density plot in Figure 4-13 shows collected current density taken for solar cells 2, 4, 6, and 8 while biased at 0 V. Shown is a decrease in current density produced as thickness increases in devices with unannealed layers of zinc oxide. Devices with thinner, unannealed layers of zinc oxide produce higher current densities than devices with thinner, annealed layers. However, the device with the thickest layer of annealed zinc oxide shows significant improvement in current density over its unannealed counterpart, that produces virtually no current at 0 V. Devices with annealed and unannealed layers of both 150 nm and 80 nm thick zinc oxide display similar performances to each other. The devices with unannealed zinc oxide produce only slightly more current than devices with identically thick but annealed zinc oxide.

4.2.3 Analysis

The current-voltage curves in Figure 4-10 and the short-circuit current density plot in Figure 4-13 show that device performance decreases as thickness of the zinc oxide electron transport layer increases. Devices with thinner layers of unannealed zinc oxide produce more current than devices with thicker layers of unannealed zinc oxide. Furthermore, the symmetrical dark current curves seen in Figure 4-10 for devices with thicker layers of zinc oxide suggests is that shunting resistance is decreasing for the devices in the dark as ZnO thickness increases. An ideal device with no imperfections in its structure has infinite shunting resistance to prevent current from leaking out of a solar cell. A thicker layer of ZnO is sturdier than a thinner layer and less prone to cracks that would cause a short circuit between electrodes.

Another possibility is that charge carriers are unable to travel through thicker layers of ZnO and transfer charge to an electrode. The absence of negatively charged electrons would account for the asymmetry between forward and reverse bias in the dark current curves. This would also account for why open-circuit voltage is decreasing as the thickness of a device's ZnO layer increases and no photocurrent is seen in

the device with the thickest layer of ZnO.

A third concern lies in how the ZnO layer is deposited during the fabrication process, described in Section 3.3. The sputtering chamber is replenished with oxygen before deposition begins. The amount of oxygen present in the chamber decreases over time and a thicker layer of ZnO takes longer to deposit onto a substrate than a thinner layer. Depleted levels of oxygen at the end of the sputtering process would change the composition of the deposited material from zinc oxide to un-oxidized zinc, making the layer less like a semiconductor and more like a metal.

Asymmetrical dark current curves are observed in devices that have thinner, unannealed layers of zinc oxide, but this is not the case for any of the dark current curves produced by devices with annealed layers of zinc oxide as seen in Figure 4-11. The offset in energy levels between zinc oxide and lead sulfide should produce asymmetry when voltage is swept in reverse and forward bias in photovoltaic device functioning properly in the dark. Lack of asymmetry in the annealed devices' dark current suggests that the devices are not performing optimally.

Variability in dark current produced by devices with annealed layers of zinc oxide, combined with sporadic light current curves, shows some inconsistency in the annealing process. Annealing devices with 10 nm layers of ZnO destroys the device as seen in solar cell 2, that produces poor current-voltage curves and no open-circuit voltage.

The current-voltage curves in Figure 4-12 show devices with layers of annealed zinc oxide produce more current, but lower open-circuit voltages than the devices with unannealed zinc oxide layers. Oven annealing might cause the zinc oxide film to fracture, leaving devices able to channel charge as current but unable to contain charge and hold a voltage. The current-voltage curves in Figure 4-11 and the short-circuit current density plot in Figure 4-13 would suggest that annealing has a restorative effect on thick layers of zinc oxide that would otherwise destroy the performance of a good device.

Chapter 5

Overview and conclusions

Third generation photovoltaics offer a new direction in engineering powerful and efficient solar cells by utilizing thin film semiconductors, organic materials, and semiconducting nanocrystals to construct new device architectures which theoretically exceed the limits of silicon solar cells.

In this thesis, two sets of lead sulfide colloidal quantum dot solar cells with unique device architectures are fabricated to test the affects of oxygen exposure, zinc oxide thickness, and zinc oxide annealing on device performance. Current-voltage characteristics are taken for all solar cells. One additional set of quantum efficiency measurements are taken for devices 20100628.

It is shown that fabricating, storing, and testing devices inside gloveboxes under vacuum or nitrogen atmospheres preserves some aspects of device quality. Devices taken outside the glovebox after deposition of the lead sulfide quantum dot layer show significant decay in quantum efficiency and short-circuit current but some improvement in generating open-circuit voltage. Power efficiency is altered but not as much as initially predicted and devices exposed to lab atmosphere for up to two hours will still produce reasonable current-voltage curves. This experiment might be performed again using greater time scales to see how device power and quantum efficiency will be after twenty-four hours or several days of exposure to the atmosphere outside of the glovebox. Further experimentation might also be done to test how devices might or might not degrade after spending a certain length of time sitting inside the glovebox

after fabrication. It is suggested that construction of a full solar panel out of these devices would require additional casing to preserve device quality over time. A design for such casing is not proposed in this thesis.

It is also shown that device architectures show optimal performance when thin, unannealed layers of zinc oxide are used as an electron accepting layer. A decrease in device performance is seen starting in layers that are at least 80 nm thick. Devices with zinc oxide 220 nm thick are shown to not produce any photocurrent or open-circuit voltage. However, an annealing process restores short-circuit current density and open-circuit voltage in a device with a 220 nm thick zinc oxide layer. Future experimentation with oven annealing would help verify the results presented in this thesis. Thicker layers of zinc oxide might be required for a sturdy device design in commercial production and show better wear over time. In the case of having a need for thicker layers of zinc oxide in device design, an annealing technique may be considered to restore the power efficiency that is achieved in solar cells with thinner layers of zinc oxide. An experiment addressing full scale production and distribution of the device architectures presented in this thesis has yet to be performed.

An additional experiment was performed by the author, Kanchi Gashaw, and Nathan Monroe testing an alternative zinc oxide deposition method to address concerns over thicker zinc oxide layers losing its properties as a semiconductor as oxygen depletes in the sputtering chamber over time. Layers of zinc oxide were deposited onto devices 10 nm at a time to achieve thicknesses from 10 nm to 53.4 nm. However, the alternative deposition process takes too much time to be useful for future fabrication and the results, which do not show significant improvement in power efficiency for devices with thicker layers of zinc oxide, are not presented in this thesis.

One important aspect of device design lies in characterizing the quantum dot films to understand how charge moves through crystalline semiconductors. Quantum dot films may be spun on top of glass substrates printed with different materials such as gold, indium-tin-oxide, zinc oxide, nickel oxide, and silicon dioxide to see how the layers become saturated or desaturated with electric charge. Films of cadmium selenide can be examined using fluorescence microscopy, as seen in Figure 5-1, that

illustrate the dots' photoluminescence. Use of atomic force microscopy may also be employed to examine the topography of lead sulfide and cadmium selenide films. These options would prove useful for improving the quality of the nanocrystal films that go into colloidal quantum dot solar cells.

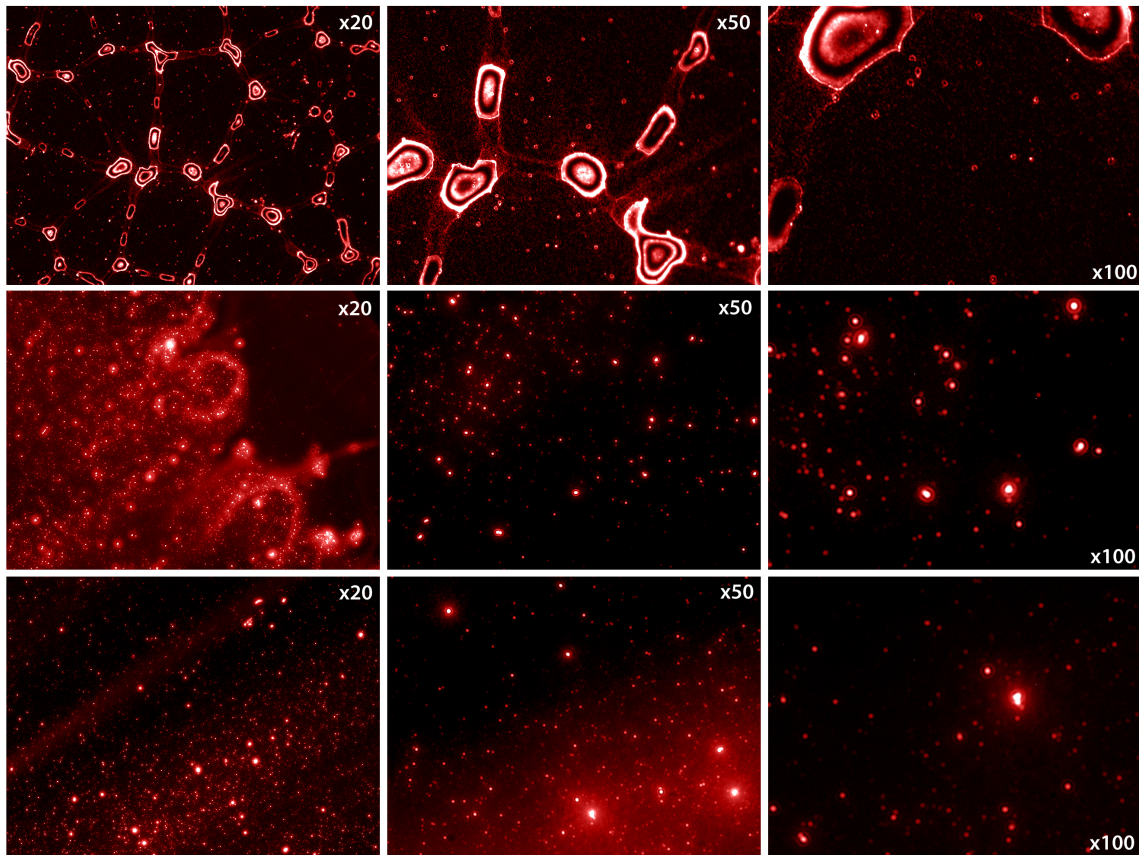


Figure 5-1: Films of cadmium selenide quantum dots diluted with chloroform and spun on top of plain glass substrates (top row) and substrates deposited with a layer of zinc oxide (middle and bottom rows), shown here under a fluorescence microscope at varying levels of magnification.

These experiments were performed in the Organic and Nanostructured Electronics Lab at the Massachusetts Institute of Technology. A new lab is under construction in Shattuck Hall at Mount Holyoke College so that more architectures for third-generation colloidal quantum dot photovoltaics may be developed, fabricated, and characterized by undergraduate students.

Appendix A

Procedure for synthesizing lead sulfide quantum dots

This document describes the procedure used for synthesizing lead sulfide quantum dots in the Bawendi Lab at MIT. Special thanks goes to Darcy Wanger of the Bawendi Group for her help and instruction in this document's preparation. Amount of degassed ODE material used in preparation will vary depending on the desired diameter of the dots. Similar materials for synthesis in the Mount Holyoke College Arango Lab may be found in lab drawers in the rear, against the wall opposing the chemical glove-box. A rough sketch of the complete setup in the fume hood is shown in Figure A-2. As always when working with chemicals, please abide by lab safety standards and above all ensure that you are wearing gloves, coats, and eye protection.

A.1 Equipment

- 3-neck flask
- Thermocouple with vacuum feedthrough
- Read-out for the temperature probe
- Condenser

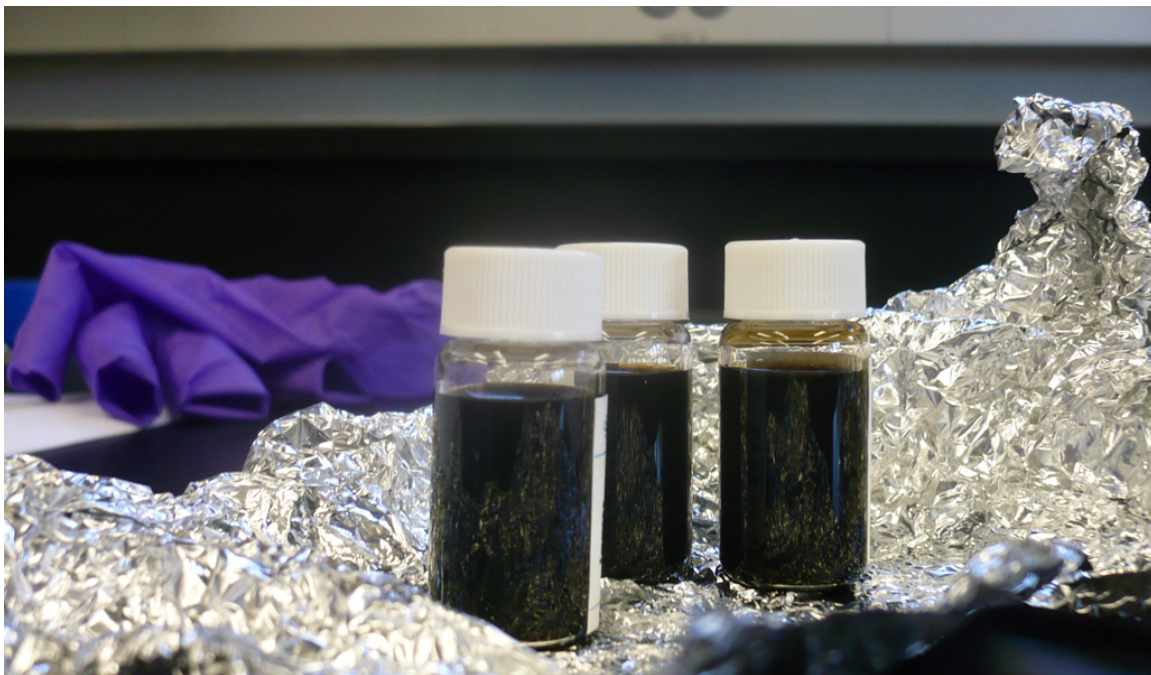


Figure A-1: Vials containing individual batches of lead sulfide nanocrystals. Each vial contains nanocrystals of different sizes: 2.3 nm (left), 3.3 nm (middle), and 5.4 nm (right) in diameter.

- Inlet adapter
- Stirrer (for 3-neck flask)
- Temperature regulator
- Lab jack
- Keck clip (for holding ground glass joints)
- Solvent trap/catcher
- O-rings
- Analytical balance (for weighing chemicals)
- Septum caps (size 14/20)
- Timer
- Dewar flask/vacuum flask
- Old cloth (to cover top of the Dewar)
- Pressure gauge (for vacuum line)
- Heating mantle
- Nitrogen flow meter
- Oil bubbler (for nitrogen line)
- Gas drying unit
- Output for heating mantle
- Hotplate Stirrer with temperature feedback (for oil bath)
- Cylindrical Pyrex container (for oil bath)

A.2 Supplies

- Vacuum grease
- Weighing paper
- Chemical scoop (for chemical powders/solids)
- One 40 ml septum vials (for degassing the ODE)
- One 40 ml septum vial (for the final quantum dot solution)
- One 7 ml vial (to make the TMS-S solution)
- Needles (purple, 16 G)
- Needles (green, 21 G)
- 10 ml syringe (for extracting ODE)
- 1 ml syringe (for adding TMS-S)
- 5 ml syringe (for extracting degassed ODE and degassed ODE/TMS-S solution)
- One 18 gauge, 6" long syringe needle (for oleic acid and final quantum dot solution)
- One 20 ml glass plunger (for the 18 gauge needle)
- Nitrile gloves
- Chem wipes
- Aluminum foil
- Two stir bars (one small, one large)

A.3 Chemicals

- 20 ml oleic acid (OA)
- 760 mg of lead acetate (PbAc)
- 5 ml of octadecane (ODE)
- 180 mg of TMS-sulfur (TMS-S)
- Silicone oil
- Bleach (sodium hypochlorite) for cleaning¹
- Hexane
- Acetone

A.4 Procedure

A.4.1 To set up the 3-neck flask where the synthesis will occur:

1. Connect the inlet adapter to the top of the condenser tube and the 3-neck flask to the bottom of the condenser. In order for the system to eventually be put under vacuum, a layer of vacuum grease must first be applied around areas where glass meets glass. Before inserting the male ends of the items into their proper female counterparts, lubricate them by applying a layer of vacuum grease in a ring around the middle of the glass tube's male end. The grease does not have to touch the edge of the tubes. Spread the grease by carefully twisting the smaller tube around inside the neck of the larger tube.
2. The 3-neck flask will need to be secured so that it is standing in an upright position. The best way to do this is to use clamps and a ring stand attached to

¹Bleach requires its own separate chemical waste container

the rear of the fume hood (the aluminum grid). The flask will later be sitting on top of the heating mantle and stirrer. Use a Keck clip to attach the inlet adaptor and the condenser.

3. Connect the vacuum line to the inlet adaptor. The vacuum tube does not have to fit snugly against the condenser. If you are having trouble sliding the tube over the adaptor, rinsing the inside of the vacuum tube with solvent is a good way to lube it up. Clamp a Keck clip down over the tube and the inlet adaptor.

A.4.2 To set up the solvent trap:

1. Ensure that the Schlenk line is temporarily isolated from the system that will eventually be pulling vacuum on the solvent trap. You do not want this system open to vacuum before the solvent trap is in place.
2. Take a rubber o-ring and apply a thin layer of vacuum grease on it. Place it in the brim of an empty, clean solvent trap. The o-ring should not fit perfectly within the circumference indented in the brim. The o-ring will expand and stretch to fill the circumference once the vacuum is pulled, ensuring a secure seal.
3. Hold the solvent trap with the inserted o-ring up to the bell jar (the top piece of the solvent trap) and secure the trap in place with a large clip. Have a lab jack ready to slide beneath it. The lab jack will support a Dewar that is going to keep the solvent trap submerged in liquid nitrogen.
4. Once the solvent trap is secured with the large clip, double-check that all vacuum lines are appropriately open or closed before turning on the vacuum pump. Make sure that the valve on the vacuum line between the solvent trap and the Schlenk line is closed. Double-check all connections and ensure that there is no place for air to leak into your line.
5. Open the vacuum line to the solvent trap and watch the pressure drop. The

vacuum should expand the o-ring and seal the solvent trap. Place the empty Dewar on top of the lab jack so that the solvent trap is hanging inside it.

6. Before fetching the liquid nitrogen to fill the Dewar, MAKE SURE THAT THE SYSTEM IS UNDER AT LEAST 300 mTorr PRESSURE.
7. Use a liquid nitrogen transfer jug/Dewar to carry liquid nitrogen from the nitrogen tanks to the right of the fume hood. Fill the Dewar sitting on the lab jack in the fume hood, taking care to make sure that the Dewar does not overflow. Take a scrap bundle of cloth (an old lab coat or blanket works well for this) and wrap it around the top of the solvent trap so that the open mouth of the Dewar is completely covered.

A.4.3 Adding the first two chemicals and completing the setup of the 3-neck flask:

1. Use a chemical scoop and analytical balance to measure out 760 mg of lead acetate (PbAc) and add the PbAc to the 3-neck flask.
2. Use the 20 ml syringe and the 6-inch long, 18 gauge needle to add 20 ml of oleic acid to the 3-neck flask.
3. Insert a stir bar into the flask and turn on the stirrer.
4. Use a 14/20 size septum to cover one of the flask's three necks. Later, this is where you will be injecting the TMS-S solution into the 3-neck flask.
5. Insert a temperature probe into the remaining neck of the 3-neck flask. Ensure that the end of the probe is in contact with the solution, but not the stir bar. Plug the temperature probe into the temperature regulator to read the temperature of the solution inside the 3-neck flask.
6. Before opening the closed, 3-neck system to vacuum, flush the 3-neck flask system through with nitrogen. Do this by sticking a 21 G syringe needle into

the septum to allow the air inside to escape as nitrogen is pushed in. Open the nitrogen Schlenk line to the 3-neck flask. This should take 1-2 minutes.

7. Once the system has been flushed with nitrogen, close the nitrogen Schlenk line to the 3-neck flask system and open vacuum Schlenk line. Pressure will briefly rise in the vacuum line. Allow the pressure to drop to 300 mTorr once again. The solution in the 3-neck flask will bubble as gas escapes and the stir bar may also stop stirring temporarily. It will take one hour to put the system under vacuum. The system is ready when there are no more bubbles escaping the solution.

A.4.4 Heating the chemicals:

1. Plug in the heating mantle and set the temperature to 100 °C. Adjust the Variac (Solid State relay, check updated Arango Lab PbS Synthesis SOP for full instructions) to control the voltage the heating mantle receives so that the mantle will not overshoot or undershoot when adjusting the temperature of the flask. Set this secondary device to output 30%-40% of power at a time.
2. It will take about one hour for the mantle to heat the solution in the flask and to keep it consistently heated for 20 minutes.
 - (a) As the solution heats up, it will turn yellow. Do not be alarmed.

A.4.5 Degassing the octadecane (ODE):

1. Prepare a hot plate underneath the cylindrical Pyrex container. Fill the container with silicone oil. Behind the hot plate, set up a ring stand and clamp to hold a temperature controller upright in the oil.
2. Use a 10 ml syringe to fill a 40 ml septum vial halfway with 20 ml of ODE. Place this vial in the clamp on the ring stand so that it is half submerged in the silicone oil bath.

3. Stick a thin syringe needle in the lid of the septum vial so that the needle is standing upright. Attach a vacuum tube to the open end of the needle (the end where you would normally connect the needle to a syringe).
4. Turn on the hot plate and heat the oil up to 110 °C.
5. Note: it is a good idea to have clean chem wipes handy to mop off the (be careful: HOT) oil that will drip off of the vial when you remove it from the bath.

A.4.6 Preparing the TMS-S solution:

1. You will be bringing into a wet chemical glovebox:
 - One 7 ml vial (to make the solution in)
 - 20 ml of degassed ODE in a 40 ml vial (see step 5: degassing the ODE)
 - One 16 G needle (purple)
 - One 5 ml syringe (for the ODE and Final Solution)
 - One 1 ml syringe (for the TMS-S solution)
 - One 21 G needle
2. TURN OFF THE CIRCULATION PURIFIER BEFORE YOU OPEN ANY CHEMICALS INSIDE THE GLOVEBOX.
3. Once inside the glovebox, use the 5 ml syringe and the 16 G needle to add 5 ml of degassed ODE into the empty 7 ml vial.²
4. Use the 1 ml syringe and 21 G needle to add 0.21 ml of TMS-S to the ODE solution in the 7 ml vial. The TMS-S is now diluted in the ODE. Use the 1 ml syringe to withdraw and extract this diluted solution in and out of the syringe, ensuring that the solution is thoroughly mixed.

²This amount may be adjusted as desired to affect the size of the resulting quantum dots.

5. Take your mixed TMS-S and ODE solution and extract 5 ml into the 5 ml syringe which was originally used to deposit the ODE. Prepare to take the materials that you brought into the wet chemical glovebox out of the glovebox.
 - (a) The vial and syringes will smell absolutely terrible at this point because of the sulfur, so be prepared to rush the materials immediately over to the fume hood where you are working in order to minimize the assault on your senses.
 - (b) Be sure that once you have withdrawn your solution into the 5 ml syringe, continue to pull back on the plunger so that empty air fills the needle ensuring that no solution will drip out of the needle while handling it outside of the glovebox.

A.4.7 Introducing the TMS-S solution to the 3-neck flask system:

1. Set the heater to turn the temperature of the 3-neck flask system down to 100 °C. If you want the final temperature of your fluid to be 100 °C after the TMS-S solution is injected, the actual solution in the flask should not be 100 °C when you inject the solution. The TMS-S is cold relative to the heated solution in the 3-neck flask, therefore once the TMS-S solution is injected, it will cause the temperature of the fluid in the flask to decrease even more.
 - (a) The final temperature of the liquid plays a crucial factor in controlling the size of the quantum dots. To increase the size of your dots, inject at a lower temperature.
2. When injecting the TMS-S and ODE solution into the 3-neck flask through the septum, be sure to do so in a quick and fluid motion. When the TMS-S is injected into the solution in the flask, the liquid should turn from a yellow tint to brown. NIFTY.

3. When you inject, start your timer going and check the temperature to see how it is dropping as the solution cools for about seven minutes. Turn off the heating mantle to let the solution cool. If you are going to remove the heating mantle at this point, raise the stage or lab jack so that it will support the 3-neck flask once the mantle is gone.

A.4.8 Preparing the PbS quantum dot solution for crash-out and storage:

1. Take a 40 ml septum vial and flush it out with nitrogen by sticking two small 21 G needles through the top, one to let in nitrogen from the nitrogen Schlenk line and the other to let the air that is inside the septum vial out. Flush the vial out with nitrogen for 5 to 10 minutes. Remove the needle that is letting the air out before removing the needle that is letting the nitrogen in.
2. The solution in the 3-neck flask should now be at a much lower temperature, about 50 °C, before transfer.
3. The 3-neck flask should still be under nitrogen atmosphere at this point.
4. Use the 20 ml glass syringe and the 6-inch long, 18 g needle to transfer the PbS out of the 3-neck flask and into the septum vial that will then be brought into the crash-out glovebox. Before slipping the needle from the septum attached to the three-neck flask, fill the needle with nitrogen inside the flask to prevent the needle from dripping while it is moving from the three-neck flask to the septum vial.

A.4.9 Clean up:

1. Dispose of excess chemicals into proper chemical waste containers. Dump used vials into chemical waste buckets.

2. Anything that has or has had quantum dots in it should be tossed out. This includes the septum on the three-neck vial.
3. Solvent vials may be rinsed out in acetone and left out to dry.
4. The TMS is going to absolutely reek, so dispose of anything that has touched this into hazardous waste.
5. The inlet adapter and condenser can be rinsed and do not usually need a base bath.
6. The thermocouple should be given a solid wipe down with a solution that is about 20% bleach, 80% water, until there is no color left on the prong from the quantum dots.
7. Anything that has touched the TMS-S, or sulfur, MUST be cleaned out with bleach. There must be a separate waste container for the bleach (sodium hypochlorite). The bleach may be used to rinse out anything that has traces of TMS-S, even before objects such as needles and used vials are disposed of. They are going to smell, so this is to prevent getting a whiff of sulfur every time afterwards you then open the solid waste container.
8. Hexane does a good job of rinsing away oily things. Use it to wipe any excess PbS off of the three-neck vial. It should also take away most of the vacuum grease.

A.5 Safety hazards

1. Do not try to force glass to do anything. Glass can (and will) break. When forcing things, control over fine muscles skills is lost. Tapping gently is better than yanking to separate stubborn tubes.
2. Do not force anything through the filters you may place over plastic needles.

3. Lead, although poisonous, does not penetrate nitrile gloves and will not rapidly penetrate skin. If any is spilled onto skin, immediately run exposed area under water for fifteen minutes.
4. Needles should be handled with caution. Always know where the tip of an uncapped needle is and do not keep more than one needle uncapped at once. To take the cap of a needle off, hold securely in one hand and use the fingers of that hand (or a second clasped directly over that hand) to gently ease the needle cap off by holding the base of the needle cap. Do not use two hands to pull apart as if uncapping a marker. To replace the cap, hold the open end of the cap at a ninety-degree angle to the tip of the needle and ease the needle tip in.
5. If stabbed with a needle, immediately rush to the sink and run the penetrated area under water, simultaneously squeezing blood out of the wound.
6. No synthesis is worth your health. If an accident occurs and you find yourself bleeding or dripping a substance onto your bare skin, drop everything and rush to the sink to tend to yourself first, alerting someone else if need be to tend to a dangerously neglected setup.

A.6 Liquid nitrogen perils

- Liquid nitrogen is extremely cold and freeze-burns will occur if you are not careful. Wear thermal gloves if your hands are going to be near the liquid.
- Liquid nitrogen will not burn if it splashes off the back of your hand, curiously enough, as it will evaporate before it has the chance to burn. However, if your hand is cupped or the liquid is given the chance to stay in contact with the skin, it will burn.

A.7 Liquid oxygen perils

- Liquid oxygen (a bright blue substance) can react with organics and cause rapid pressure changes to the surrounding environment. As such, any liquid nitrogen that occurs near the synthesis setup should be treated with extreme caution and avoided at all cost.
- Liquid oxygen condenses at a higher temperature than liquid nitrogen, thus nitrogen may be used to condense oxygen.

Appendix B

Procedure for spinning lead sulfide quantum dot films

This document describes the procedure used for spinning films of lead sulfide quantum dots in the ONE-Lab at MIT as the third layer in solar cell device fabrication. Similar materials for synthesis in the Arango Lab at Mount Holyoke College may be found in lab drawers in the rear, against the wall opposing the chemical glovebox. As always when working with chemicals, please abide by lab safety standards and above all ensure that you are wearing gloves, coats, and eye protection.

B.1 Supplies

- 2 200 ml vials (I-CHEM, Vial Clear Boro w/Septa, blue caps, item: S226-0030)
- 2 6 ml syringes (NORM-JECT, Henke Sass Wolf)
- 2 dunking vials (VWR SC6602-300 pk, barcode: 193972)
- 1 small vial (VWR 66011-020 pk, barcode: 193500)
- 1 glass reusable syringe
- teflon-coated tweezers

- 1 micro-syringe
- 2 or 3 pipette tips for micro syringe
- latex chem gloves
- aluminum foil
- sharpie marker

B.2 Chemicals

- Hexane
- Acetonitrile (ACN)
- EDT solution (ethanedithiol, in freezer)

B.3 Safety notes for spinning quantum dot films

- The circulation purifier to the glovebox should be turned off whenever you are exposing chemicals to the glovebox atmosphere.
- Always wear an extra pair of latex gloves over your glovebox gloves when working with chemicals inside the glovebox.
- Do NOT uncap the syringe needles by using both hands. Hold the syringe in one hand and use your thumb to ease off the cap. You will stab yourself otherwise. This will hurt. It will also destroy the glovebox glove and expose your bloodstream to all of the nasty and toxic chemicals that others have been working with inside the glovebox.
- Make sure that all vials and bottles in the glovebox that contain chemicals are capped when they leave your hands. By capping them before setting them down, you reduce your chances of spilling things on the glovebox floor. You may think that you will remember, but you won't.

- When extracting chemicals from jars, make sure that the tip of the needle is completely submerged. Hold jar securely in one hand and operate the syringe with the other.

B.4 Procedure for chemical preparation

1. Turn OFF the circulation purifier in the glovebox.
2. Put on latex or nitrile chemical gloves over the glovebox gloves on your hands before working with chemicals inside the glovebox.
3. Take 5 to 6 ml of hexane and put into an empty vial. This will be used for cleaning out the glass reusable syringe, which in turn will be used to deposit the quantum dot solution onto the spinning devices.
4. Take 6 ml of acetonitrile and put into an empty vial labeled “ACN.”
5. Take 6 ml of acetonitrile and put into an empty vial labeled “EDT.”
6. Take 2 ml of acetonitrile and put into a small, empty vial. This will be used for diluting the EDT.
7. Take exactly 20 microliters of EDT and add it to the small vial that already has 2 ml of ACN in it. After depositing, shake the container a little to make sure that the solution is properly stirred and mixed.
8. Take exactly 120 microliters of this mixed EDT and ACN solution in the small vial and deposit into the vial of ACN labeled “EDT.” Again, shake gently to make sure that the solution is properly mixed.

B.5 Procedure for spinning films of lead sulfide onto device

1. Turn OFF the circulation purifier in the glovebox.

2. Using the green teflon-coated tweezers, place your device, face up, on the chuck of the spin coater.
3. Take 20 microliters of the PbS quantum dot solution into the glass, reusable syringe.
4. Deposit/squirt the 20 microliters of quantum dots onto the device and immediately run the spinner at 1500 rpm for 1 minute.
5. While the spinner is running, rinse the syringe using the hexane solution by transferring clean hexane from the hexane vial and depositing the now “dirty” hexane and PbS solution into the empty vial.
6. When the spinner stops, use the teflon-coated tweezers to dunk the device into the solution of 0.02% EDT that you have prepared for 30 seconds. After, transfer the device into the pure ACN solution for about 5 seconds, taking care to make sure that you hold the device with the tweezers to keep it submerged instead of letting the device drop and sink.
7. Wipe the back of the device on your glove to help dry the evaporating ACN and place the device back onto the chuck of the spin coater. Run the spin coater once again to dry the device completely.
8. Repeat steps 3-7 as needed.
9. Place your device back into its container. Before depositing the final pair of ITO electrodes onto device, use tweezers to scrape off a border of excess quantum dots coating the ten electrode pads on the device.

Appendix C

Full scale current-voltage and quantum efficiency curves

Full scale versions of the current-voltage and quantum efficiency curves for devices 20100628 and devices 2010706 in Chapter 4 are included to display in greater detail.

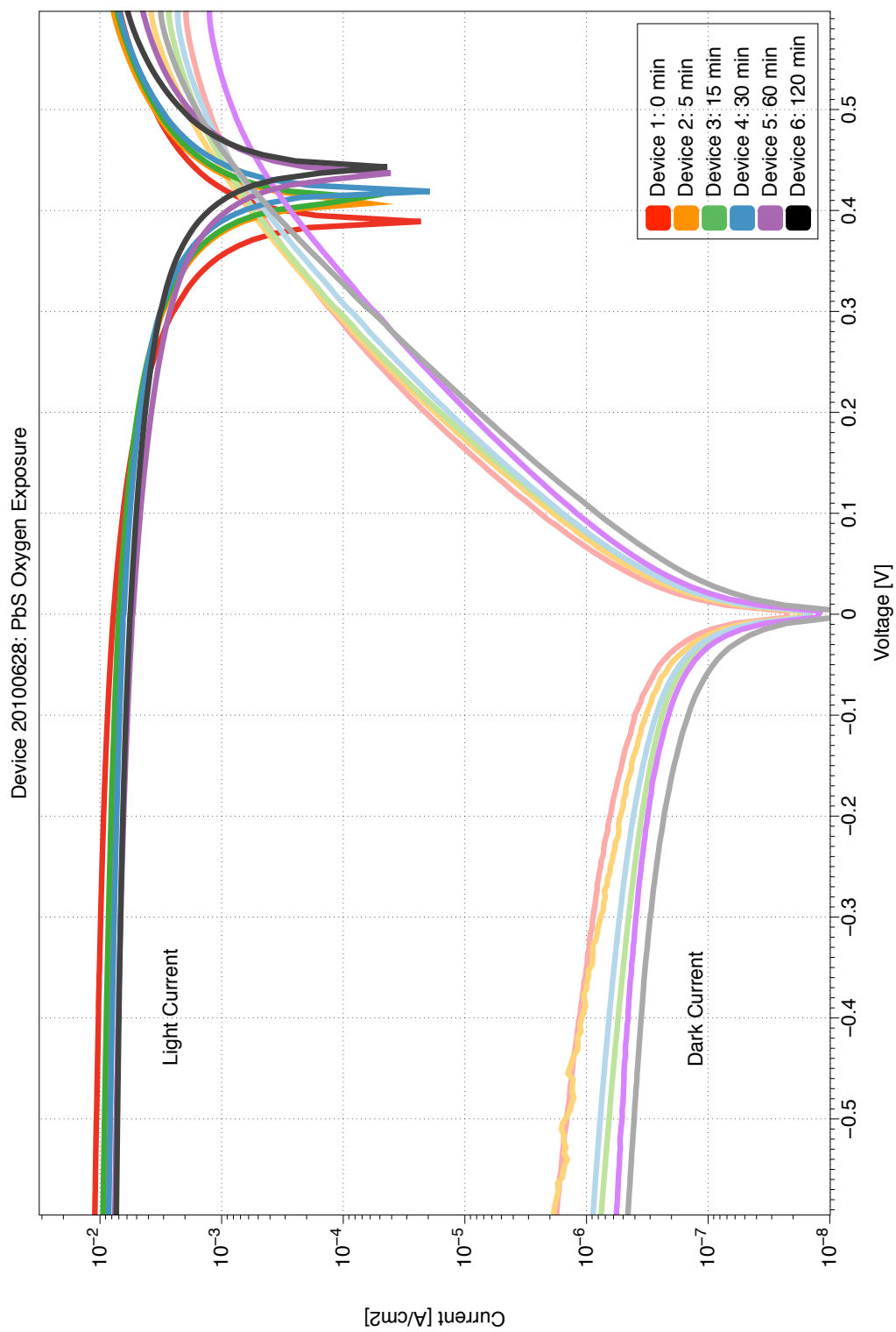


Figure C-1: Full scale current-voltage curves for devices 20100628 showing how current and voltage varies between devices which have spent varying amounts of time outside of an inert glovebox atmosphere.

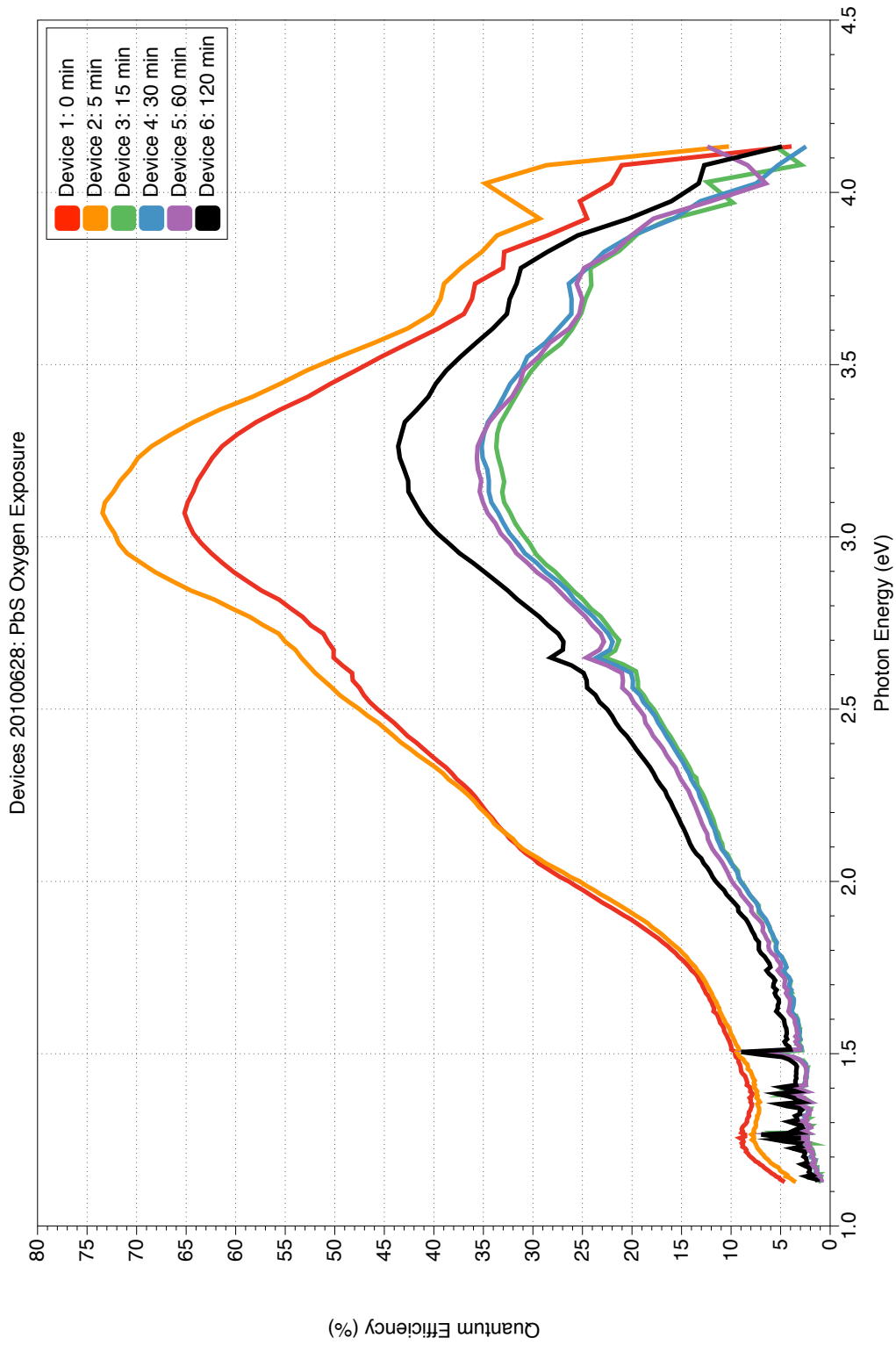


Figure C-2: Full scale quantum efficiency curves for devices 20100628 showing how photon energy absorption varies between devices which have spent varying amounts of time outside of an inert glovebox atmosphere.

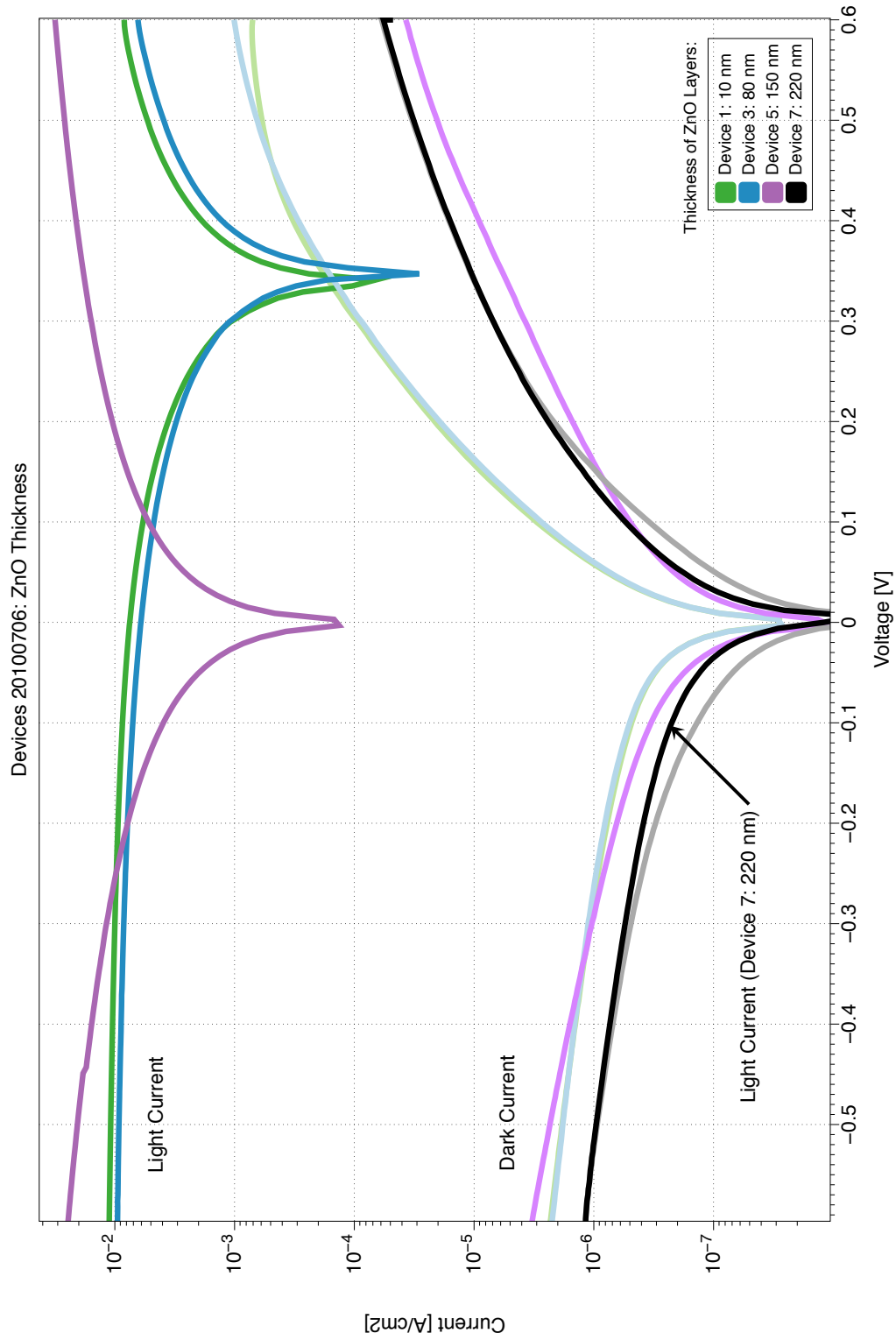


Figure C-3: Full scale current-voltage curves for solar cells 1, 3, 5, and 7 out of the set of devices 20100706. Each was fabricated with ZnO layers of different thicknesses ranging from 10 nm to 220 nm.

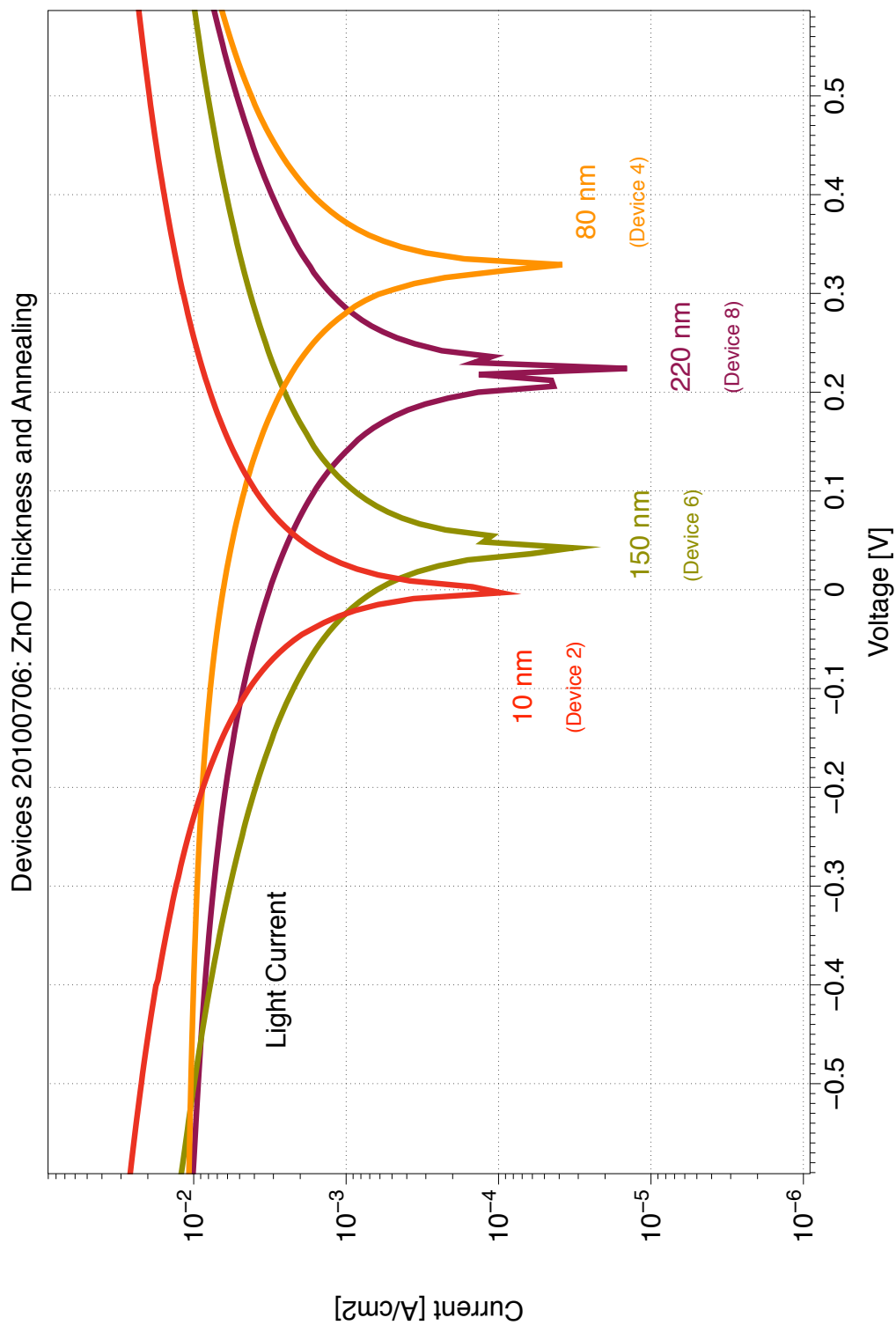


Figure C-4: Full scale light current-voltage curves for solar cells 2, 4, 6, and 8 out of the set of devices 20100706. Each was fabricated with ZnO layers of different thicknesses ranging from 10 nm to 220 nm that were annealed in an oven before the PbS layer was spun on top.

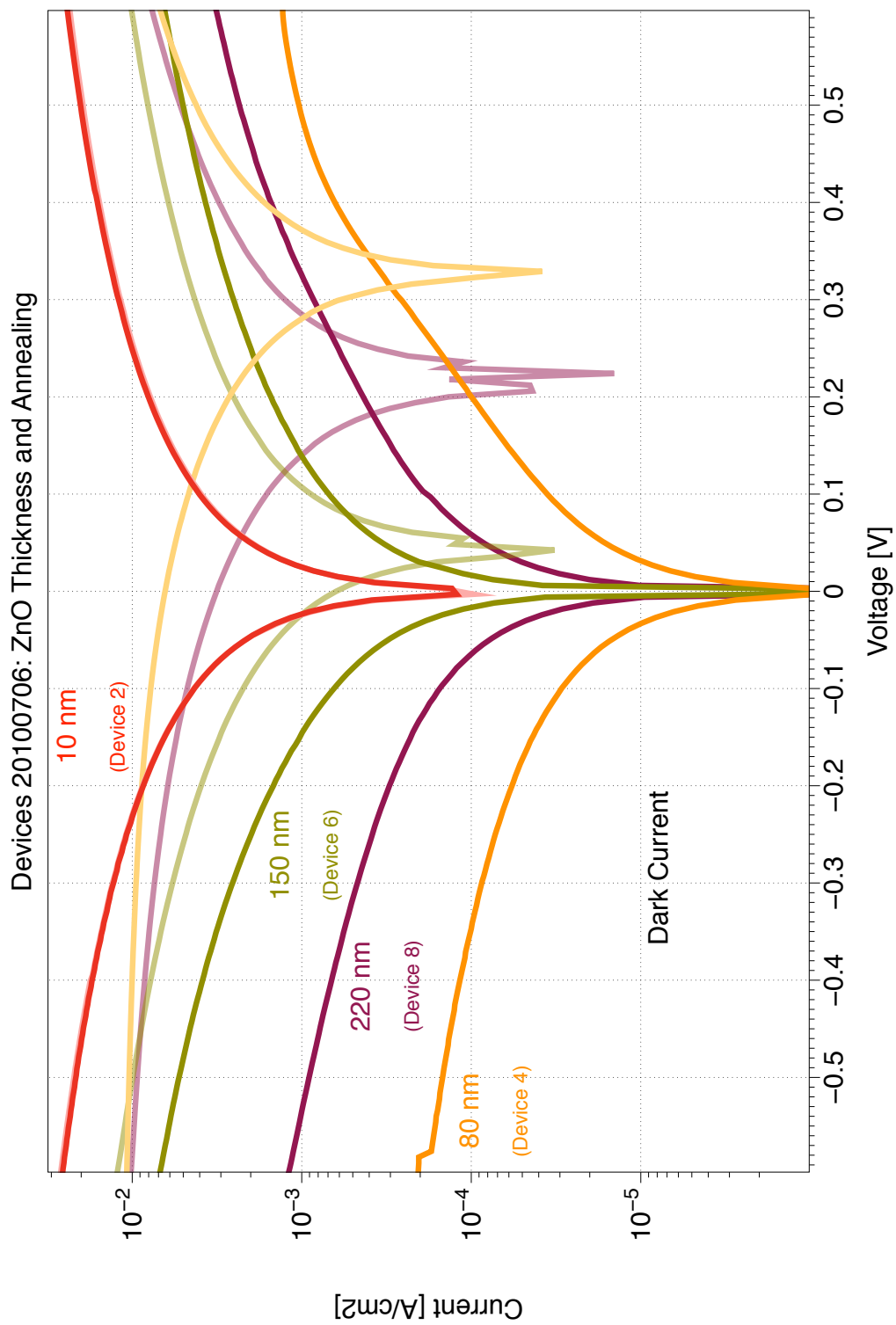


Figure C-5: full scale dark current-voltage curves overlaying the light curves from Figure C-4 for all devices 20100809. Each was fabricated with ZnO layers of different thicknesses ranging from 10 nm to 220 nm that were annealed in an oven before the PbS layer was spun on top.

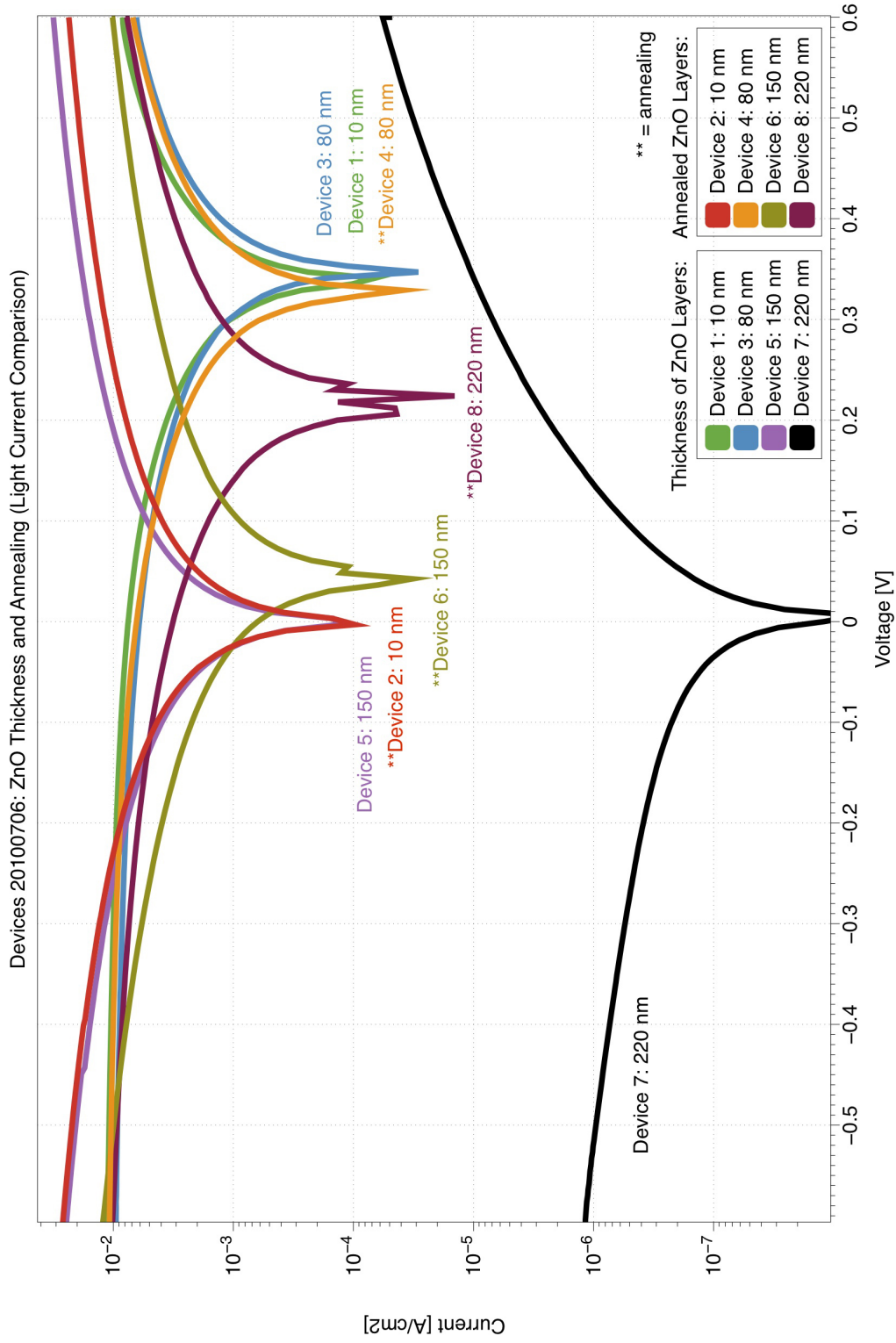


Figure C-6: full scale light current-voltage curves from all solar cells out of the set of devices 20100706 showing how devices with different thicknesses of ZnO performed with and without annealing the ZnO layer.

Bibliography

- [1] National Aeronautics and Space Administration (NASA). International Space Station Gallery. <http://spaceflight.nasa.gov/gallery/images/station/index.html>, January 2011.
- [2] National Aeronautics and Space Administration (NASA). International Space Station: Facts and Figures. http://www.nasa.gov/mission_pages/station/main/onthestation/facts_and_figures.html, January 2011.
- [3] National Aeronautics and Space Administration (NASA). The Very Latest SOHO Images. <http://sohowww.nascom.nasa.gov/data/realtime-images.html>, March 2011.
- [4] National Aeronautics and Space Administration (NASA). About the Very Latest SOHO Images. <http://sohowww.nascom.nasa.gov/data/realtime/image-description.html>, April 2011.
- [5] Theodore Brown, Eugene LeMay, and Bruce Bursten. *Chemistry: The Central Science*. Pearson, New Jersey, 10th edition, 2007.
- [6] Alexi C. Arango. *High open-circuit voltage in heterojunction photovoltaics containing a printed colloidal quantum-dot photosensitive layer*. PhD thesis, Massachusetts Institute of Technology, 2010.
- [7] Jenny Nelson. *The Physics of Solar Cells*, chapter 1: Introduction, pages 1–16. Imperial College Press, London, 2003.

- [8] Thomas C. Hayes and Paul Horowitz. *The Student Manual for the Art of Electronics*. Cambridge University Press, New York, 1989.
- [9] Dina Fine Maron. One Percent of U.S. Coal Plants Closed to Avoid Pollution. <http://www.scientificamerican.com/article.cmf?id=one-percent-us-coal-plants-closed-avoid-pollution>, April 2011.
- [10] Michael D. Lemonick. “I Stick to the Science”. *Scientific American*, 304(6):84–87, June 2011.
- [11] Martin Rees and et al., editors. *Universe*, chapter The Sun, pages 120–123. DK Publishing, New York, 2008.
- [12] National Aeronautics and Space Administration (NASA). About the SOHO Mission. <http://sohowww.nascom.nasa.gov/about/about.html>, April 2011.
- [13] National Aeronautics and Space Administration (NASA). SOHO Extreme ultraviolet Imaging Telescope (EIT). <http://umbra.nascom.nasa.gov/eit/>, April 2011.
- [14] Mary D. Archer. *Clean Electricity from Photovoltaics*, volume 1 of *Series on Photoconversion of Solar Energy*, chapter 1: The past and present, pages 1–32. Imperial College Press, London, 2001.
- [15] American Society for Testing and Materials (ASTM). Reference Solar Spectral Irradiance: Air Mass 1.5. <http://rredc.nrel.gov/solar/spectra/am1.5/>, January 2011.
- [16] W.G. Adams and R.E. Day. The Action of Light on Selenium. *Philosophical Transactions of the Royal Society of London*, 167:313–349, 1877. JSTOR permanent link: <http://www.jstor.org/stable/109173>.
- [17] Hugh W. Hillhouse and Matthew C. Beard. Solar cells from colloidal nanocrystals: Fundamentals, materials, devices, and economics. *Current Opinion in Colloid & Interface Science*, 14:245–259, 2009.

- [18] Robert F. Service. Can the Upstarts Top Silicon? *Science*, 319:718–720, February 2008.
- [19] M Riede, T Mueller, W Tress, R Schueppel, and K Leo. Small-molecule solar cells—status and perspectives. *Nanotechnology*, 19:1–12, September 2008.
- [20] Cyrus Wadia, A. Paul Alivisatos, and Daniel M. Kammen. Materials Availability Expands the Opportunity for Large-Scale Photovoltaics Deployment. *Environmental Science & Technology*, 2009.
- [21] Jonathan J. M. Halls and Richard H. Friend. *Clean Electricity from Photovoltaics*, volume 1 of *Series on Photoconversion of Solar Energy*, chapter 9: Organic photovoltaic devices, pages 377–445. Imperial College Press, London, 2001.
- [22] Mark Z. Jacobson and Mark A. Delucchi. A Path to Sustainable Energy by 2030. *Scientific American*, pages 58–65, November 2009.
- [23] 7 Radical Energy Solutions. *Scientific American*, 304(5):38–45, May 2011.
- [24] Joseph M. Luther, Matt Law, and et al. Schottky Solar Cells Based on Colloidal Nanocrystal Films. *Nano Letters*, pages A–E, August 2008.
- [25] Ahmed Maria, Paul W. Cyr, and et al. Solution-processed infrared photovoltaic devices with $\geq 10\%$ monochromatic internal quantum efficiency. *Applied Physics Letters*, 87(21):213112 1–3, November 2005.
- [26] Keith W. Johnston, Andras G. Pattantyus-Abraham, and et al. Schottky-quantum dot photovoltaics for efficient infrared power conversion. *Applied Physics Letters*, 92(15):15115 1–3, April 2008.
- [27] Keith W. Johnston, Andras G. Pattantyus-Abraham, and et al. Efficient Schottky-quantum-dot photovoltaics: The roles of depletion, drift, and diffusion. *Applied Physics Letters*, 92(12):122111 1–3, March 2008.

- [28] Byung-Ryool Hyun and et al. Electron Injection from Colloidal PbS Quantum Dots into Titanium Dioxide Nanoparticles, month = October, volume = 2, number = 11, year = 2008. *ACS Nano*, pages 2206–2212.
- [29] Joshua J. Choi and et al. PbSe Excitonic Solar Cells. *Nano Letters*, 9(11):3749–3755, August 2009.
- [30] Kurtis S. Leschkies, Timothy J. Beatty, and et al. Solar Cells Based on Junctions between Colloidal PbSe Nanocrystals and Thin ZnO Films. *ACS Nano*, 3(11):3638–3648, October 2009.
- [31] Alexi C. Arango, David C. Oertel, Youfeng Xu, Mounqi G. Bawendi, and Vladimir. Bulovic. Heterojunction Photovoltaics Using Printed Colloidal Quantum Dots as a Photosensitive Layer. *Nano Letters*, 9(2):860–863, 2009.
- [32] Andras G. Pattantyus-Abraham, Illan J. Kramer, and et al. Depleted-Heterojunction Colloidal Quantum Dot Solar Cells. *ACS Nano*, 4(6):3374–3380, May 2010.
- [33] Ni Zhao, Tim P. Osedach, and et al. Colloidal PbS Quantum Dot Solar Cells with High Fill Factor. *ACS Nano*, 4(7):3743–3752, June 2010.
- [34] Tong Ju, Rebekah L. Grahm, and et al. High efficiency mesoporous titanium oxide PbS quantum dot solar cells at low temperature. *Applied Physics Letters*, 97(4):043106 1–3, July 2010.
- [35] Paul Horowitz and Hill. *The Art of Electronics*. Cambridge University Press, New York, 2nd edition, 1989.
- [36] Steven E. Schwarz and William G. Oldham. *Electrical Engineering: An Introduction*, chapter 13: Semiconductor devices, pages 481–498. Oxford University Press, 2nd edition, 1995.
- [37] V. Petrova-Koch. Milestones of solar conversion and photovoltaics. In Vesselinka Petrova-Koch, Rudolf Hezel, and Adolf Goetzberger, editors, *High-Efficient Low-*

Cost Photovoltaics, volume 140 of *Springer Series in Optical Sciences*, pages 1–5.
Springer Berlin / Heidelberg, 2009.